Sensor and Simulation Notes
Note 153
25 June 1972

Electromagnetic Design Calculations for ATLAS I, Design 1

Carl E. Baum, chairman
Lt Daniel Higgins
Air Force Weapons Laboratory

David B. Cummings
James E. Faulkner
Milton Heinberg
Peter Moore
Edwin B. Nelson
Marvin L. Price
Nuclear Defense Research Corp.
of New Mexico

Walter F. Crewson
J. T. Naff
Pulsar Associates

Abstract

Besides the calculations of specific boundary value problems for transmission-line EMP simulators the various effects observed in such calculations need to be integrated together to actually design such a simulator. This note gives an example of such design considerations for a specific set of simulator dimensions from the electromagnetic point of view. This is for one design option termed design 1 of ATLAS I, a horizontally polarized transmission-line EMP simulator intended primarily for testing aircraft supported off the ground on a test stand called a trestle. The direction of wave propagation is also horizontal with respect to the terrain.

Foreword

This note is a somewhat different type of note when contrasted to most other Sensor and Simulation Notes. Most other such notes are concerned with design principles for classes of simulators (or sensors) or electromagnetic boundary value problems which quantify specific aspects of simulator (or sensor) design and performance. This note goes in a different direction. In case you, the reader, have wondered what you are supposed to do with all the information provided in these notes you may find part of the answer in this note.

In designing a simulator such as ATLAS I there are many design questions to be quantified. For the general class of TEM transmission line EMP simulators there is a considerable body of practical experience in their use and many of the Sensor and Simulation Notes are devoted to individual design questions for this class of simulators. More notes are also being written on relevant questions for such simulators. As time goes on we know more and more questions to ask. This note then serves as a summary of where we stand at present and where we are headed.

One purpose of the electromagnetic design effort for ATLAS I and II is to spread out some of the knowledge of the electromagnetic characteristics of transmission line EMP simulators among a larger group of people. Thus at the request of the chairman a committee was formed to perform the design calculations for ATLAS I and II. This note is a report of this committee with contributions to the calculations, curves, writeup, and/or review coming from all members of this committee. This committee is coextensive with the list of authors of this note. The chairman also provided overall guidance to the committee and acknowledges numerous useful conversations on this simulator design with John Darrah and Maj. Al Aube.

We have come a long way in the development of the technology of transmission line EMP simulators. Since Ralph Partridge first proposed in Sensor and Simulation Note 1 the three plate transmission line which was built and later named ALECS there has been some progress. ALECS was modified to a two plate design for missile testing. A much bigger facility called ARES was then designed primarily for missile testing. Even around the time ARES was being designed, thought was given to the application of transmission line EMP simulators to aircraft testing. Some of this was later documented in Sensor and Simulation Note 82 for transmission lines giving a horizontally polarized electric field in the working volume. Here the concept of a trestle-like test stand (not an EMP simulator itself) was also introduced. Around early 1969 the first such advancement of transmission line EMP simulators oriented toward

aircraft testing was proposed at AFWL to be constructed in the Kirtland AFB vicinity with the first of these named ATLAS to follow in the tradition of ALECS and ARES.

So here we are with the present report on the electromagnetic design calculations (at least in their present iteration) for ATLAS I, design 1. Already the dimensions for ATLAS I, design 2 have been chosen and hopefully a similar report will cover this. The transmission line EMP simulator for vertically polarized electric fields is tentatively called ATLAS II (unless an equally good distinct name in the same sequence is developed). Already dimensions for both designs 1 and 2 for ATLAS II have been chosen and reports will also hopefully be issued on the state-of-the-art electromagnetic calculations for these cases.

While transmission line EMP simulators are only one type of EMP simulator they are more useful than some other types for certain EMP simulation problems. More government agencies and contractors are starting to make their own. Hopefully this note can provide some guidance on how to go about it.

TABLE OF CONTENTS

I. Introduction

The ATLAS I simulator with which this report is concerned is a horizontally polarized transmission line EMP simulator.[14] It is primarily intended for testing aircraft (including the largest aircraft in operation at present) in their in-flight configurations. For the most part, the aircraft will be in their normal orientation with wings and fuselage approximately horizontal. To do this the aircraft are positioned on a trestle test stand. Such a simulator produces a horizontally polarized electric field (approximately) in a working volume where aircraft are to be positioned above the trestle. This allows the electric field polarization to be made parallel to the aircraft wings or fuselage as desired. This is important because large resonances are associated with currents on the wings for antisymmetric electric field excitation and on the fuselage plus wings in a symmetric electric field excitation.[41,42,43]

The name of this particular EMP simulator (which is not the name of a class or type of EMP simulator) is an acronym just as in the cases of ALECS and ARES. However, it has several interpretations already, just as in some other cases. Even several years ago when ATLAS was established it had several meanings presently remembered. The best one would appear to be AFWL Transmission Line Aircraft Simulator but there are others both serious and humorous such as AFWL Trestle Aircraft Simulator and AFWL Terribly Large Aircraft Simulator. There may be other interpretations proposed later on just like some people have later changed the simulator name on various occasions. Of course one important point of the name ATLAS (or a similar name) is that it is a direct extension of ALECS and ARES. In this sequence of transmission line EMP simulators the simulators have merely gotten larger and more sophisticated design considerations have been used.

In designing this simulator we have taken a somewhat iterative approach. More than one set of design dimensions (at least two sets so far) have been established. The first of these is called design 1. Between designs 1 and 2 the general shape is the same but design 2 is a little smaller. Figures 1.1 through 1.3 show perspective views of three possible orientations for ATLAS I including the direction of entry of the aircraft onto the trestle. Note that other orientations are possible. These drawings have been made with a view toward siting the simulator on terrain which falls off away from the runway and tow road level making some of the earth excavation problems easier. This roughly corresponds to the presently discussed site on Kirtland AFB on the north side of Tijeras arroyo. Figure 1.4 shows top and side views for design 1 (and design 2) roughly to scale. Note that this report does not discuss the design of the trestle or associated above ground

walkways. These are basically mechanical design questions and are not very significant electromagnetically as long as certain general guidelines are followed. This question is discussed in another report.[34] Some electromagnetic calculations to better quantify this question may be done at some future time.

The general design philosophy is discussed in references 34 through 38, all containing as parts of their titles: "General Principles for the Design of ATLAS I and II." For an understanding of the various techniques which can be used to design such a simulator the reader should read these reports. Combined with this report which considers a specific case (ATLAS I, design 1) the reader can better understand how to proceed and what some of the options are. A few future reports can be added to this list for completeness and they will have similar titles for ready identification.

The electromagnetic performance of an EMP simulator, if considered in detail, is a complex issue. Over the years many calculations pertinent to transmission line EMP simulators have been documented. The list of references at the end of this report would be a good place for the reader to begin his search. All of these except those listed as possible future reports are quite readily available at many places.

As time has progressed new questions have been recognized and some answers developed having various degrees of quantitative accuracy. One problem that the reader may encounter then is that there are so many relevant questions that can (and therefore should) be asked. No one parameter (such as peak electric field somewhere in the working volume) should be the sole design criterion, thereby giving a design for which several other important parameters have poor performance associated with them. This leads to the concept of a balanced design. If because of money limitations, time limitations, etc. the simulator cannot be perfect then one should consider all the parameters relevant to the simulator performance and accept compromises in some equivalent sense on all of them. This means that if certain useful design features are trivial to achieve in terms of money, time, and/or other relevant considerations then very little compromise should be accepted. On the other hand if other design parameters involve comparatively more money, technical risk in actually constructing it, etc. then one should be willing to compromise a little more on these parameters provided the money, risk, etc. can be significantly reduced thereby.

When formulating specifications then one should think of them in terms of something like this balanced design concept. No numbers are hard and fast; they can shift up and down somewhat as required. From the beginning it was recognized that while we knew roughly what type of simulator and roughly what

size was required in a gross sense, still there were many tradeoffs to be made. Furthermore as such transmission line simulators get larger and larger and thus generally more expensive it becomes desirable to accept somewhat more distortion as long as this is rationally controlled.

This report is based on one set of simulator dimensions for ATLAS I. A choice was made with this balanced design concept in mind. These dimensions are illustrated in figure 1.5. Note that these are the macroscopic dimensions for electromagnetic purposes. These dimensions are chosen with a few constraints in mind. The 90 meter maximum vertical extent was chosen to avoid what appeared to be excessive earth excavation if the top of the simulator was not to be more than about 45 meters above the local roughly flat ground near the Tijeras arroyo site since this simulator site is near an airport (for obvious reasons). Furthermore the working volume should have horizontal dimensions of about 75.7 meters to accommodate the 747 and C-5 aircraft which are the largest aircraft considered and have roughly the same dimensions. These automatically implied compromises on field uniformity in the working volume, interaction of the aircraft with the side plates and earth, and interaction of the transmission line plates with earth. As one will see later some of the distortion figures such as for field uniformity at low frequencies can exceed 20% at some positions. Comparing these numbers with those for other designs (evaluated in about the same way) and comparing these designs while including cost and schedule estimates one can make a better choice for the actual simulator.

Note in the choice of ATLAS I, design 1, only the major macroscopic features are fixed. For example the dimensions of the outer plates for the input transitions are fixed with respect to the two apexes, but the beginning of the transitions is at the pulsers. The pulser dimensions depend on the details of the pulser design which are not specified here. The distance of the pulsers from the apexes and the corresponding plate spacing at the pulsers are only nominal and are included in figure 1.5 merely for illustration. Similarly the termination positions and dimensions are nominal. The apex of the output transition is what is fixed.

Another set of dimensions not specified in figure 1.5 is the details of the earth contouring underneath and to the side of the simulator. The basic earth dimensions that are fixed are first the lowest earth level as 90 meters below the highest position at the junction of the central ground planes in the input transitions. Second the roughly extrapolated earth level is about 30 meters below the apexes of the input transitions. While the level of the ground is lowest beneath the working volume it should be contoured upward as one advances up the input transitions and toward the central ground planes. This

helps to make the ground reflections propagate less toward the working volume. Note that the junction of the central ground planes may not reach the lowest ground level so as to allow the ground level near the ground planes to be raised somewhat under the 20 meter spacing from the working volume to the ground planes and under the ground planes as one moves back up the transitions. Back near the pulsers the earth is lower than 30 meters below the apex height as one moves away from the ground planes but does not go below 45 meters below the apexes which is the lowest ground level. Reference 34 has more discussion and sketches for the earth contouring design.

In section XII various of the simulator performance parameters are summarized. Whether or not this represents a "balanced design" at the present state of the art depends somewhat on more detailed results for the mechanical design. However this does establish a very useful design for comparison to other designs such as design 2 or others which are as yet unspecified. None of these designs are "perfect" if only because of our limited knowledge. Next year we will know a little more and this might shift a few numbers. However, one expects that this will continue to be the case. As we find more answers these tend to suggest more questions.

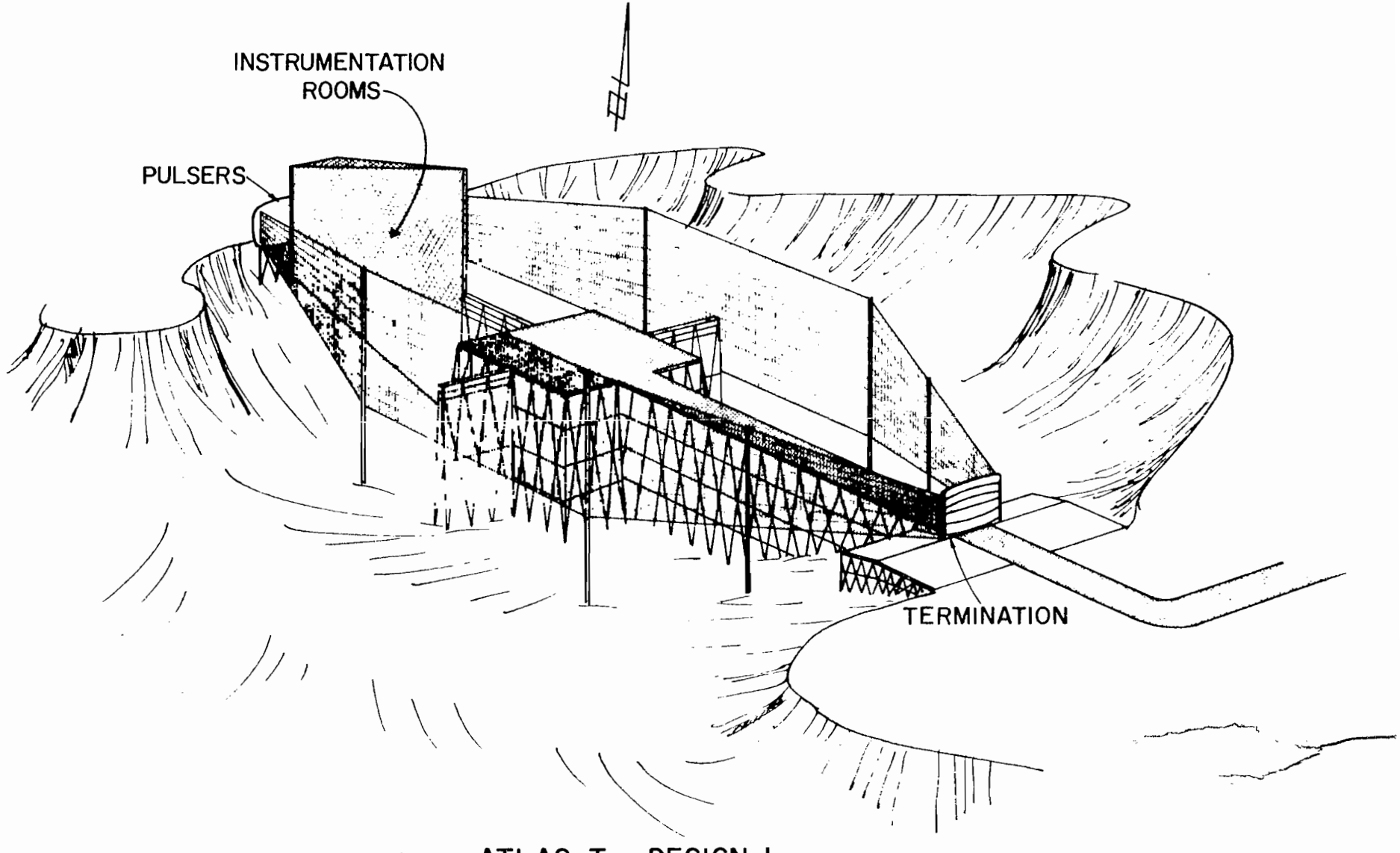

ATLAS I DESIGN I

PROPAGATION IN SOUTHEAST DIRECTION

Figure 1.1

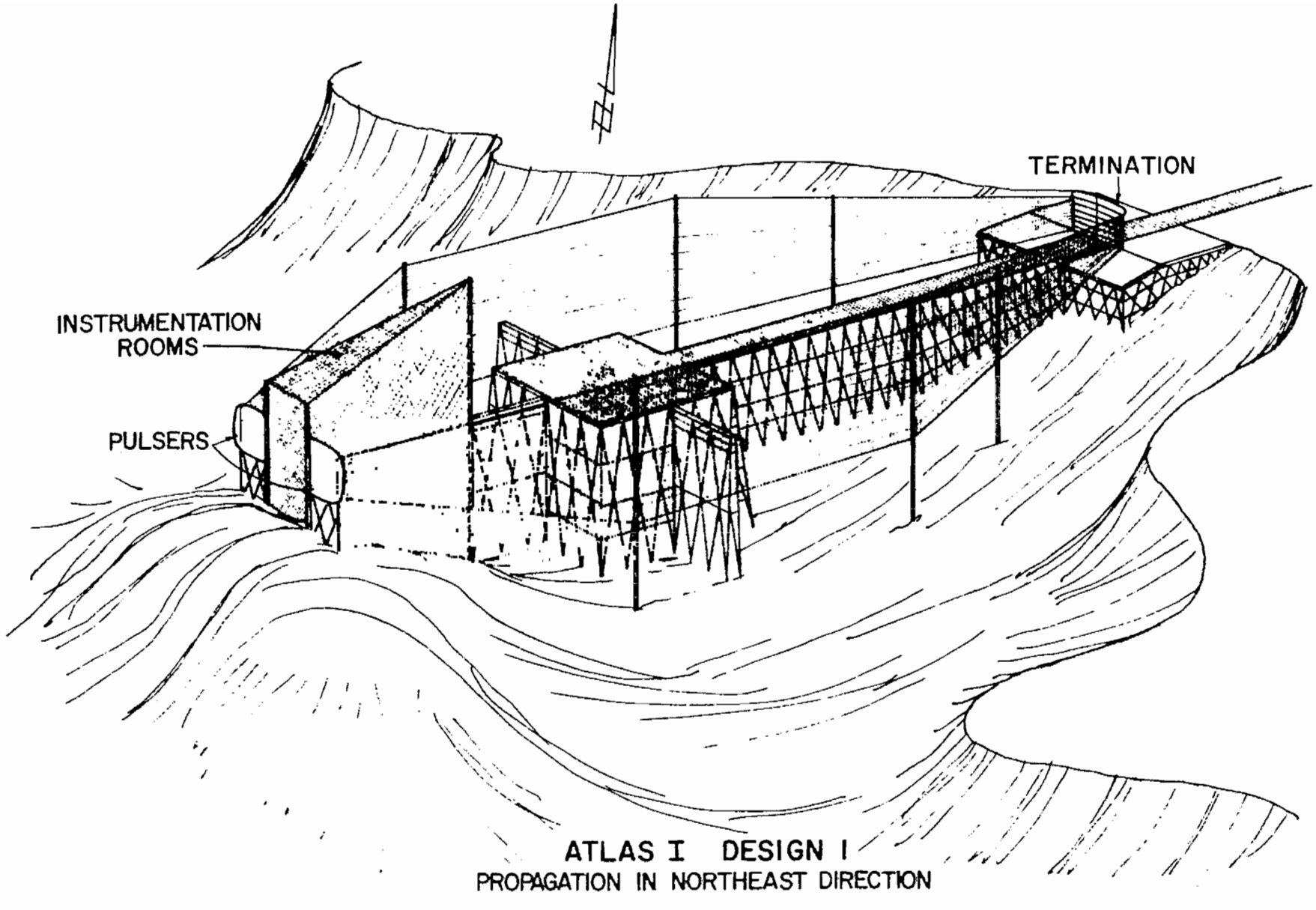
TERMINATION
INSTRUMENTATION ROOMS
PULSERS
ATLAS I DESIGN I
PROPAGATION IN NORTHEAST DIRECTION

Figure 1.2

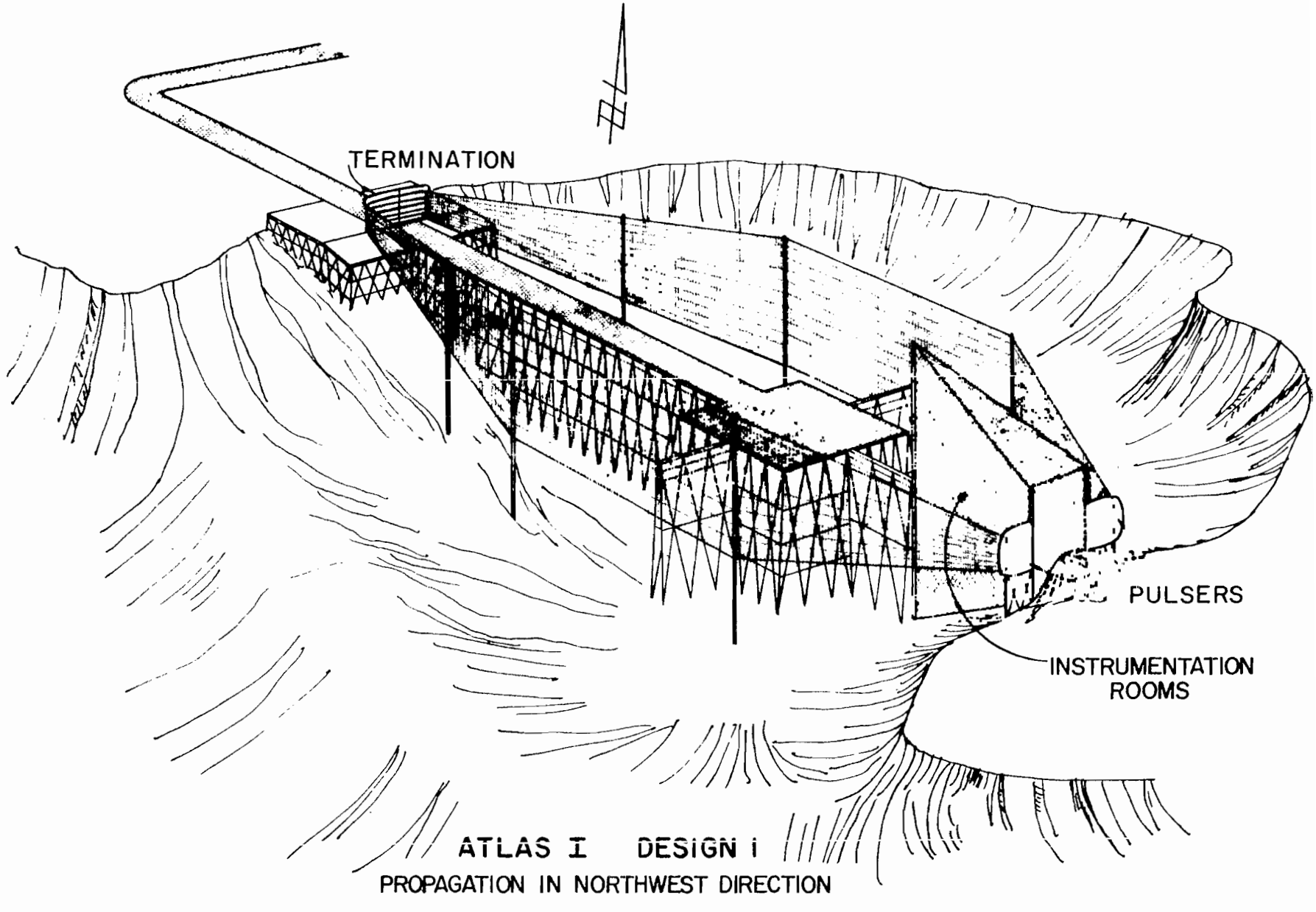
TERMINATION
PULSERS
INSTRUMENTATION
ROOMS
ATLAS I DESIGN i
PROPAGATION IN NORTHWEST DIRECTION

Figure 1.3

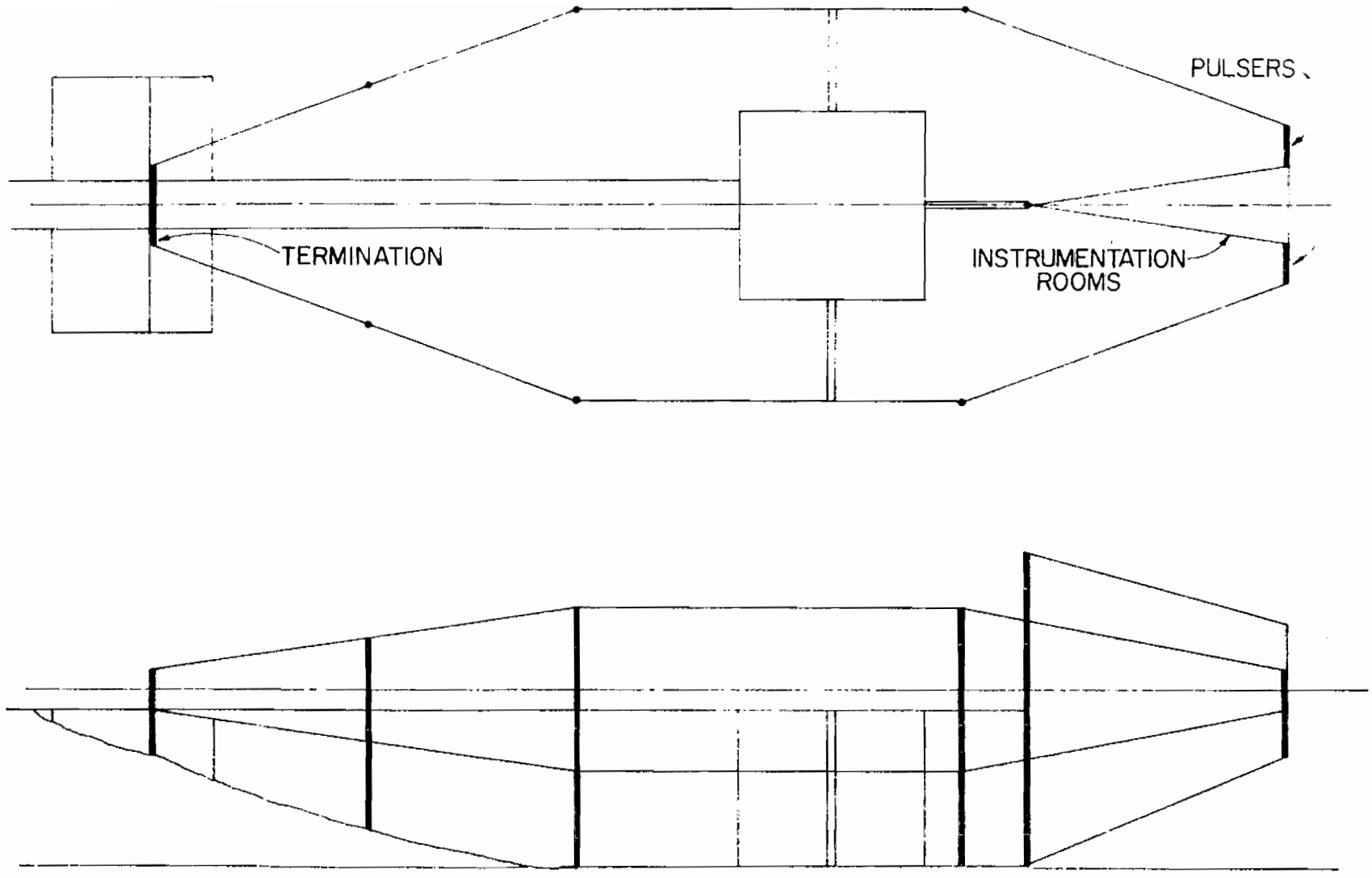

ATLAS I DESIGN I

Figure 1.4

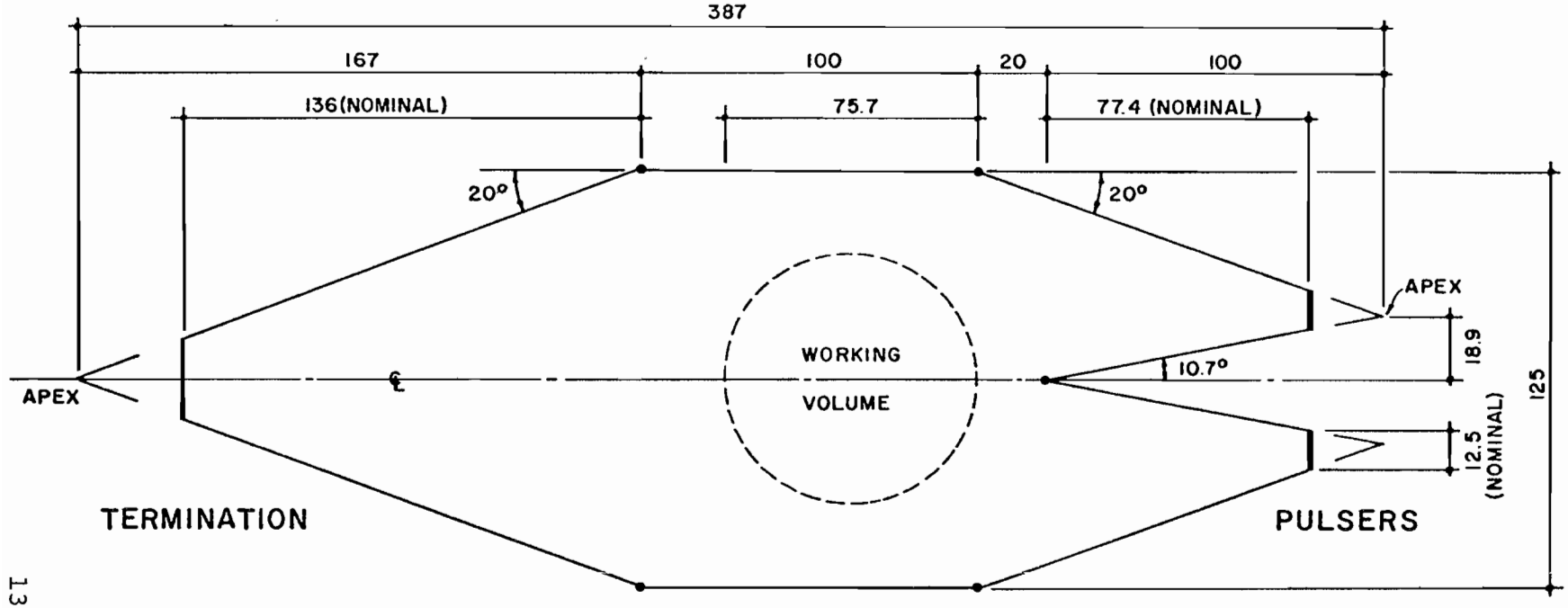

ALL DIMENSIONS IN METERS

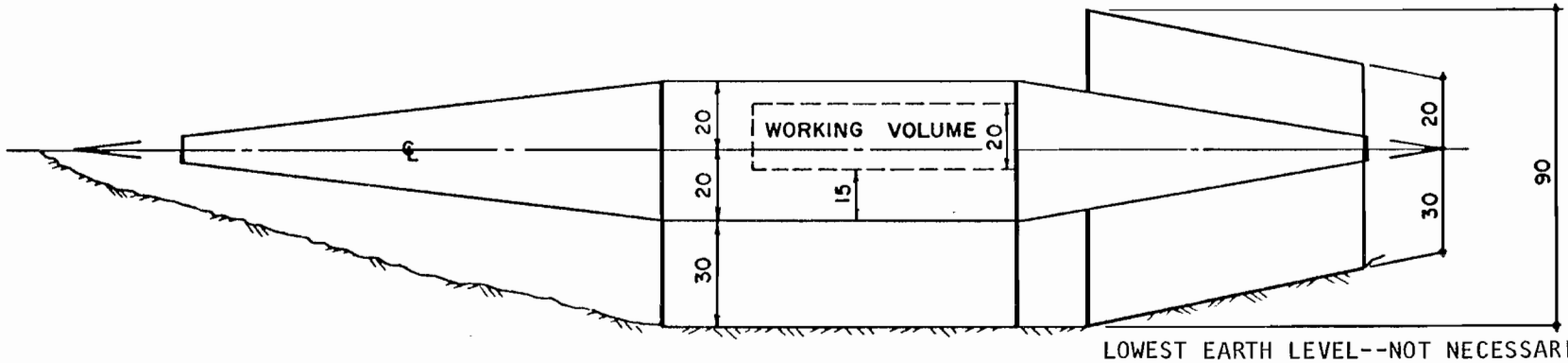

ATLAS I DESIGN 1

Figure 1.5

II. Interaction of the Aircraft with the Side Plates near Resonant Frequencies

One of the initial problems in the design of the ATLAS simulators is the determination of the plate spacing. If the plates can be kept close together, then the required pulser voltage can be minimized. However, if the plates approach the working volume too closely, then the aircraft being tested will interact strongly with the plates. This results in changes in the charge and current distributions on the surface of the aircraft, shifts the resonant frequency and alters the decay time constant. These "interaction effects" are inconsistent with a simulated environment of free space and should be minimized.

SSN 111 (Reference 22) was used as the basis for estimating and evaluating these interaction effects. This reference treats the case of an infinite parallel-plate transmission line in free space with a right circular cylinder midway between the plates and oriented with its axis perpendicular to the plane of the plates. The notation and the geometry used in the calculations are shown in figure 2.1.

SSN 111 assumes a step-function plane wave traveling between the parallel plates and then calculates (1) the currents and charge densities induced on the surface of the cylinder as a function of time and frequency, and (2) the decay time ratio. These data are computed for two values of the parameter a/h (0.1 and 0.01), and for several values of h/s.

In applying the data of SSN 111 to an ATLAS design, the first problem that arises is the choice of cylinder dimensions (a and h) which can reasonably be expected to represent a specific aircraft. The most obvious course of action is merely to choose a cylinder that approximates the dimensions of the aircraft fuselage, which implicitly assumes that the aircraft is oriented with its fuselage perpendicular to the simulator axis.

Allowance must still be made for the fact that the fuselage is not of constant diameter nor even truly cylindrical and the radome of the aircraft is non-conducting. Even more serious is the fact that the effects of the wing have been completely disregarded. Failing to allow for these dissimilarities contributes to the uncertainty of the results.

An alternate method of choosing cylinder dimensions assumes that the aircraft is oriented with its fuselage parallel to the simulator axis. The wingspan is then taken as the cylinder length. The radius of the cylinder is selected such that this radius is equal to the equivalent radius of the wing. In this model the fuselage is disregarded; this is at least partially compensated for by the fact that the fuselage will lie

along the symmetry plane of the simulator where its effects will be minimized.

Figures 2.2 to 2.5 are drawings showing the dimensions of the 747 aircraft and the C-5A aircraft. As an example of how to use the data contained in SSN 111 consider the 747 oriented with the fuselage parallel to the simulator axis.

The wingspan of the 747 is 59.6 m. The wing surface is approximately 1068 m^2. Each nacelle, considered as a cone 7.6 m long and 2.6 m in base diameter, has a surface area of 30.9 m^2. The total surface area of the wings and nacelles is then approximately 1192 m^2. Using a crude area rule and equating this area to $2\pi a\ell$ (a = radius of equivalent cylinder, ℓ = length of equivalent cylinder) yields a = 3.2 m. The parameter h = $\ell/2$ = 29.8 m. Thus a/h $\simeq$ 0.107.

With the dimensions of the equivalent cylinder determined, the graphs of SSN 111 can be used to evaluate the performance of a simulator. Examples of methods of applying the SSN 111 data will be demonstrated using a $\simeq$ 3.2 m and h = 29.8 (i.e., the 747 oriented with the fuselage parallel to the simulator axis). Figure 2.6 is a reproduction of figure 4 of SSN 111 which is a graph of $I_s(0)/I_\infty(0)$ versus s/h. $I_s(0)$ is the surface current at the cylinder midpoint at the resonant frequency when the plate spacing is 2s. $I_\infty(0)$ is the same measurement except that the plate spacing is infinite. The ratio, $I_s(0)/I_\infty(0)$, is an indication of how closely free space will be simulated with a plate spacing of 2s. For design 1 for a 747 with fuselage parallel to the plates s/h = 2.1 and the ratio $I_s(0)/I_\infty(0)$ is about 1.05; hence, design 1 satisfies a specification that current densities as measured in the frequency domain shall be within 5% of the value that would occur in free space as compared to the results including interaction with the side plates. However this is only the change in the resonant frequency response.

Figures 5a and b and 6a and b of SSN 111, reproduced here as figures 2.7 through 2.10, show the time history of the cylinder surface current with a/h and h/s as parameters. After the first peak, the currents have differences in phase and magnitude for different values of h/s. In any case the peak current induced on the cylinder for any plate spacing will be the same as would occur in free space. At the second current peak (ct/h $\simeq$ 3.5) it appears that the current density will still be within 30% of the free space value. At even later times the variation may be greater. This will occur at times >500 ns and the currents will have decayed to <25% of their maximum values.

The decay time specification for design 1 can be checked directly by use of figure 7 of SSN 111 reproduced here as figure 2.11. The ordinate of this graph is τ_s/τ_∞ which is the

ratio of the cylinder decay time when the plate spacing is 2s to the decay time with infinite plate spacing.

SSN 111 does not directly supply data with which the surface charge densities on the cylinder between the plates can be compared with the charge densities that would occur in free space. However, table II of SSN 111 does list the "field enhancement factors" at different h/s values, and from these the charge densities can be computed. C_r is the charge density on the end of the cylinder at the first resonant frequency and C_m is the charge density on the end of the cylinder at the time of first current reversal. By dividing each of the computed values of C_r by the value of C_r when h/s = 0 (the free space case) we can see the effect of the simulator plates on the response of the test object. Similarly for C_m we can calculate the charge density ratio in the time domain. The following table lists the data from these computations:

for a/h = 0.1	h/s	C_r	C_r/C_r (at ∞)	C_m	C_m/C_m (at ∞)
	.9	11.598	.746	15.465	1.610
	.8	11.283	.726	11.005	1.146
	.7	11.831	.761	10.061	1.047
	.6	12.897	.830	9.728	1.013
	.5	15.336	.987	9.580	.997
	.4	17.263	1.111	9.575	.997
	.3	15.011	.966	9.574	.997
	.0	15.537	1.000	9.607	1.000
for a/h = 0.01	.9	91.275	.664	62.513	1.126
	.8	102.839	.748	57.278	1.032
	.7	120.106	.874	56.246	1.013
	.6	142.882	1.040	55.735	1.004
	.5	156.107	1.126	55.657	1.002
	.4	140.084	1.019	55.662	1.003
	.3	133.226	.969	55.690	1.003
	.0	137.421	1.000	55.522	1.000

Table 2.1

Plots of the data are shown in figures 2.12 and 2.13.

Up to now we have just considered the 747 oriented with the fuselage parallel to the axis of the simulator as an example of how to use the attached graphs. One can also consider other aircraft and aircraft orientations. The appropriate dimensions for two orientations of a 747 and a C-5A are summarized in table 2.2.

Aircraft	747		C-5A	
Orientation of fuselage with respect to simulator axis	⊥	∥	⊥	∥
Fuselage length	69.86 m (229 ft)	-	75.7 m (248 ft)	-
Fuselage radius	3.2 m (10.6 ft)	-	5.8 m (19 ft)	-
Wingspan	-	60 m (195.7 ft)	-	68 m (222.7 ft)
Wing area	-	1,070 m^2 (11,500 ft^2)	-	1,090 m^2 (11,650 ft^2)
Nacelle area	-	124 m^2 (1,330 ft^2)	-	107 m^2 (1,150 ft^2)
Total area	-	1,200 m^2 (12,830 ft^2)	-	1,190 m^2 (12,800 ft^2)
Equivalent cylinder 1/2 length (h)	35 m	29.8 m	37.75 m	33.5 m
Equivalent cylinder radius (a)	3 m	3.2 m	5.9 m	2.85 m
a/h ratio	.086	0.107	0.156	0.084
s/h ratio	1.79	2.09	1.67	1.85

Table 2.2
Equivalent Cylinder Dimensions

Because only two values of a/h were considered in SSN 111, an a/h ratio of .1 is used to consider all four cases tabulated in table 2.2. [This should be a pretty good approximation with the possible exception of the C-5A oriented with its fuselage perpendicular to the axis of the simulator.] Then using the appropriate h/s ratio the various interaction specification ratios can be read from the graphs of figures 2.6 to 2.13. These results are summarized in table 2.3. It is readily seen that the parameter affected most by the plate interaction is the decay time.

One should note that all of these calculations are based on an idealized geometry which includes the assumption of infinitely wide, perfectly conducting plates. In fact, the plate width of design 1 is a good bit smaller than the plate separation and the plates will probably be sparse structures rather than solid sheets. These considerations would tend to indicate that the interaction effects are in actuality less than those calculated in reference 22 and the numbers generated in this report are actually worst case estimates.

Aircraft	747		C-5A	
Orientation of fuselage with respect to simulator axis	⊥	∥	⊥	∥
Current Density Ratio From fig. 2.6	.89	1.05	.83	.90
Current Density Ratio From fig. 2.7 at $ct/h \simeq 3.5$	.76	.82	.73	.78
Decay Time Ratio From fig. 2.11 - τ_s/τ_∞	.60	1.01	.61	.68
Charge Density Ratio From fig. 2.12 - C_{m_s}/C_{m_∞}	1.01	.99	1.01	~1.00
Charge Density Ratio From fig. 2.13 - C_{r_s}/C_{r_∞}	.935	1.05	.85	.93

Table 2.3

Aircraft Interaction Data

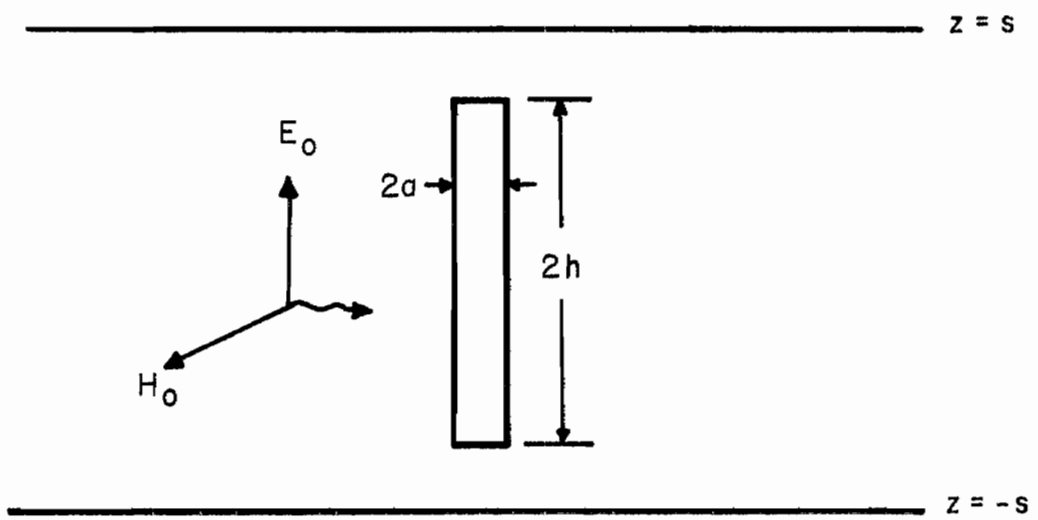

Figure 2.1. Notation and geometry used in SSN 111.

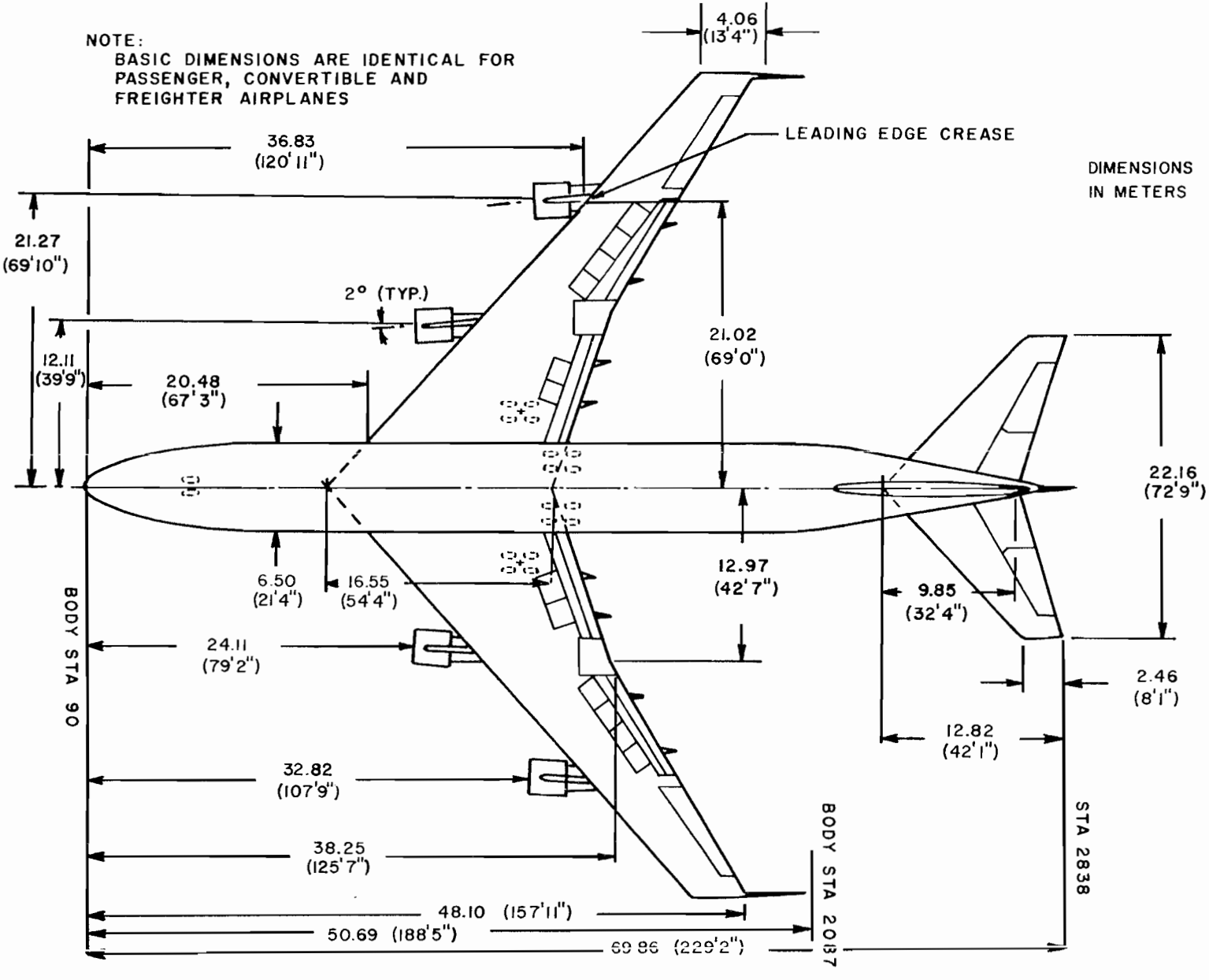

Figure 2.2. Boeing 747 dimensions

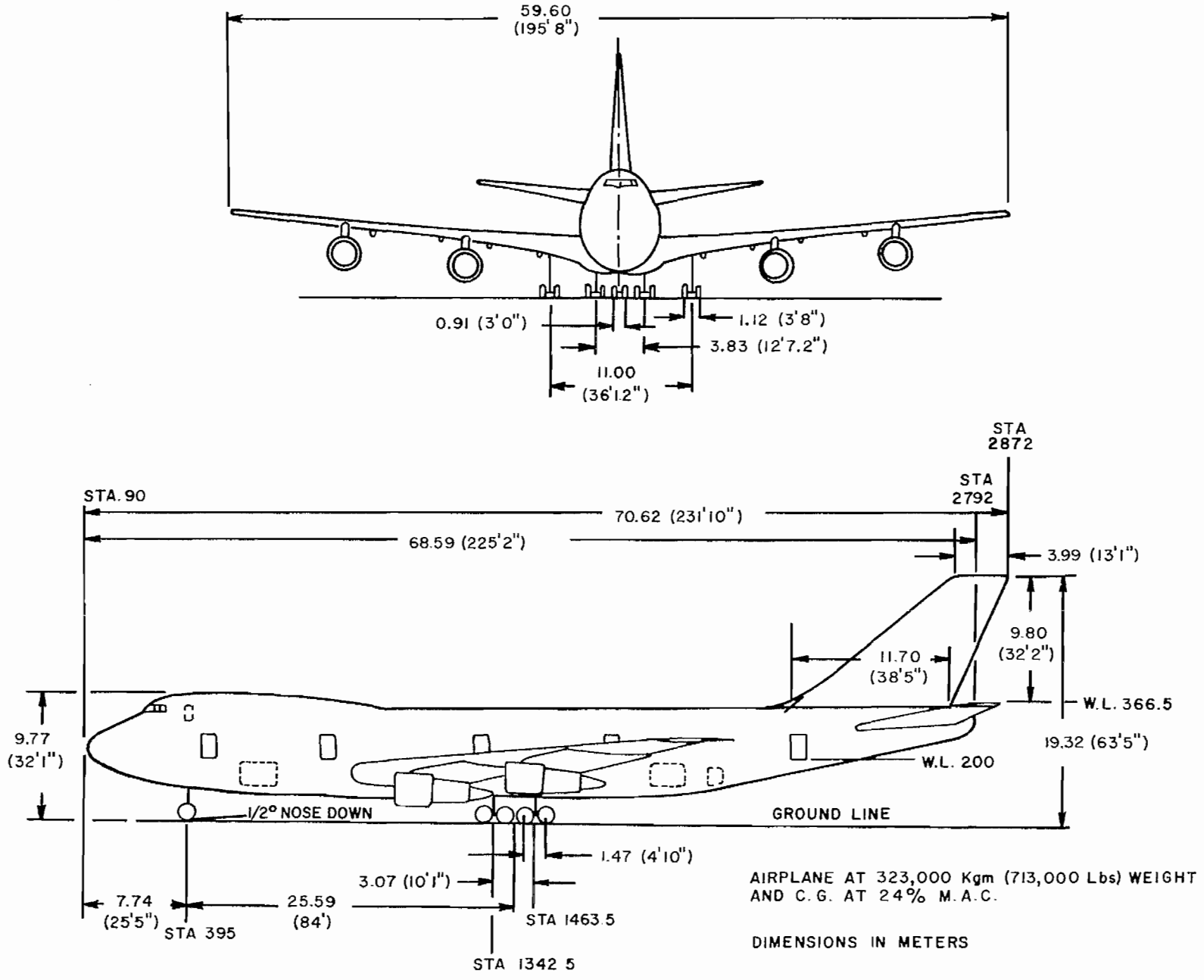

Figure 2.3. Boeing 747 dimensions

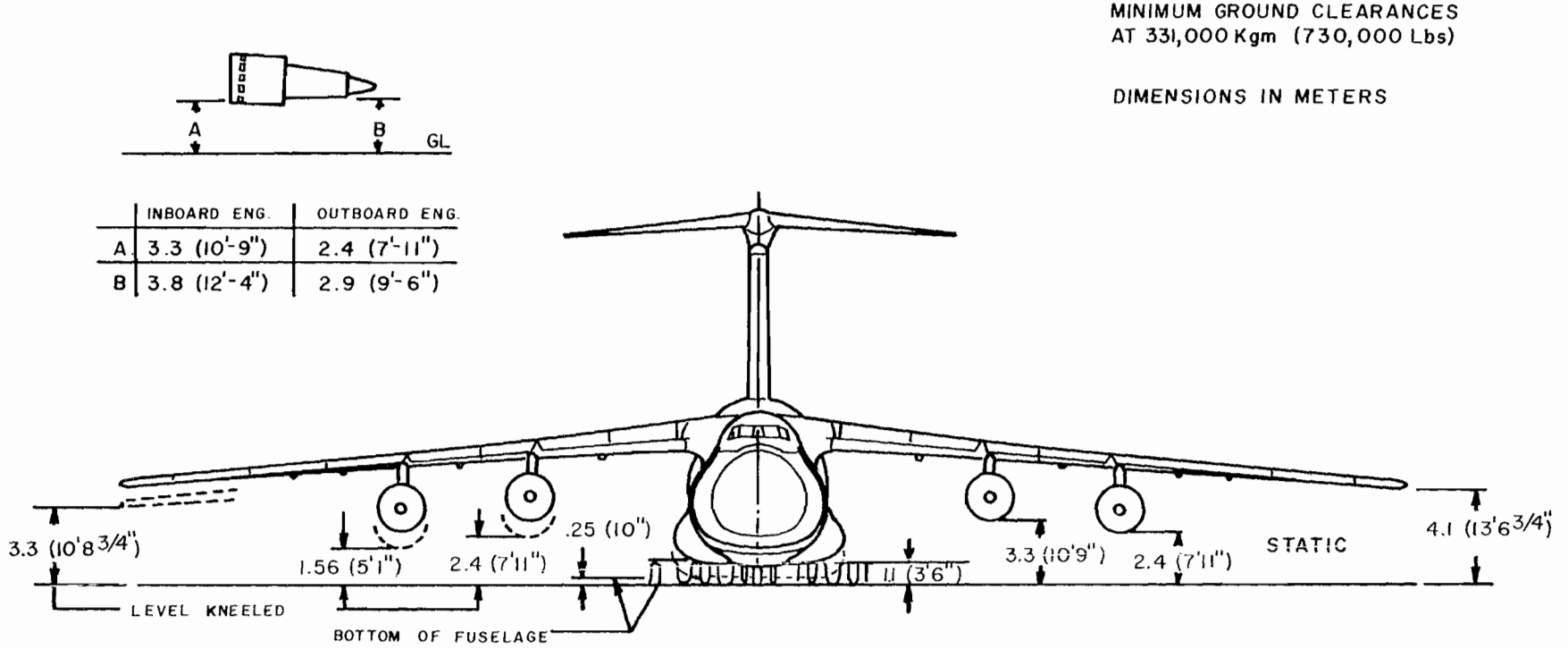

NOTE:
DIMENSIONS REFLECT GROUND CLEARANCES ON A SMOOTH SURFACE AT A GROSS WEIGHT OF 331,000 Kgm (730,000 Lbs) WITH 111,000 Kgm (245,000 Lbs) WING FUEL LOAD

Figure 2.4. C-5A dimensions

	A	B	C
STATIC	14.4 (47'-3.5")	19.9 (65'-1.17")	9.3 (30'-7.5")
LEVEL KNEELED	13.6 (44'-5.5")	19.0 (62'-3.17")	8.5 (27'-9.5")

GENERAL AIRCRAFT DIMENSIONS
AT 348,000 Kgm (769,000 Lbs)

DIMENSIONS IN METERS

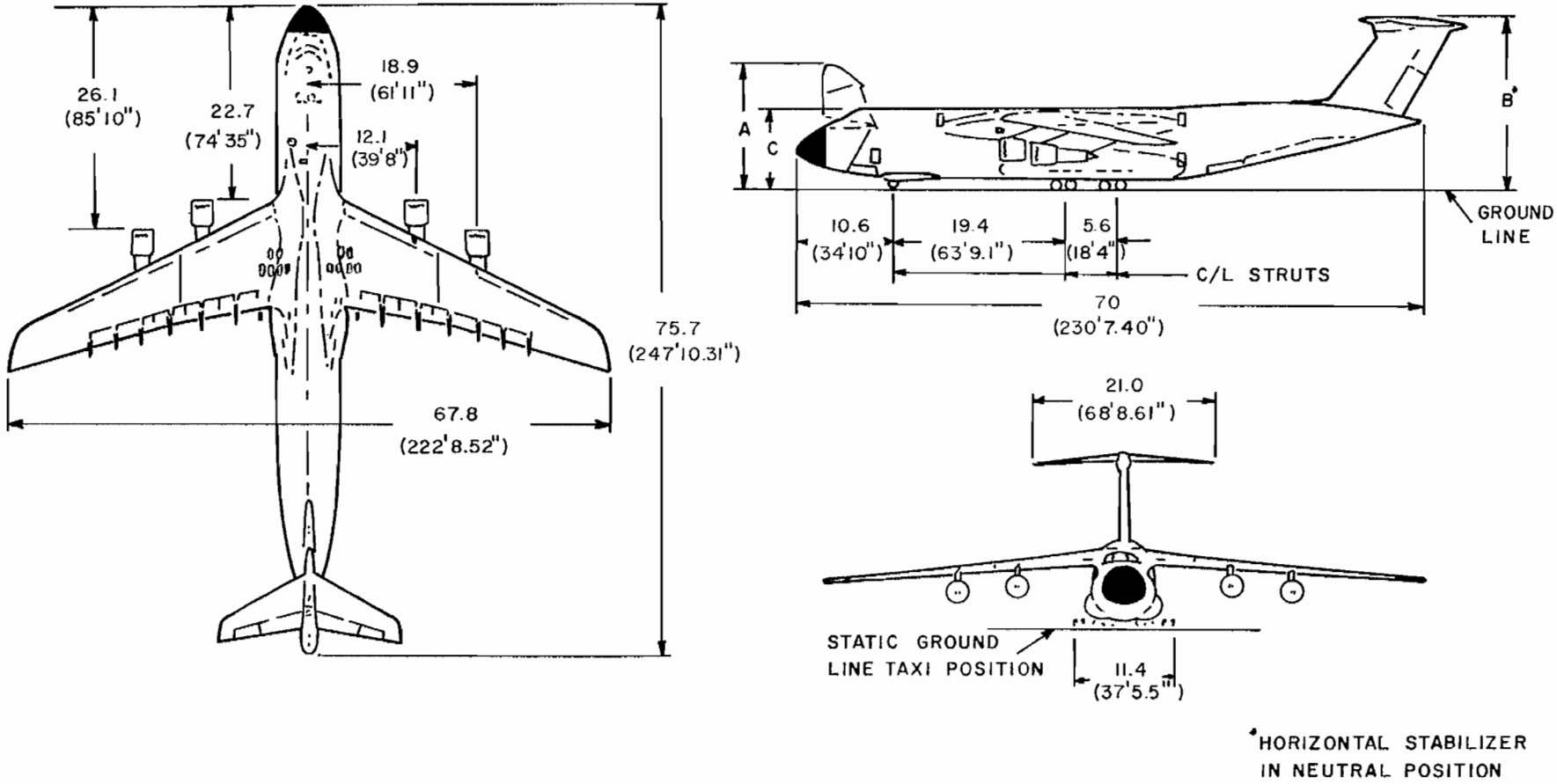

Figure 2.5. C-5A dimensions

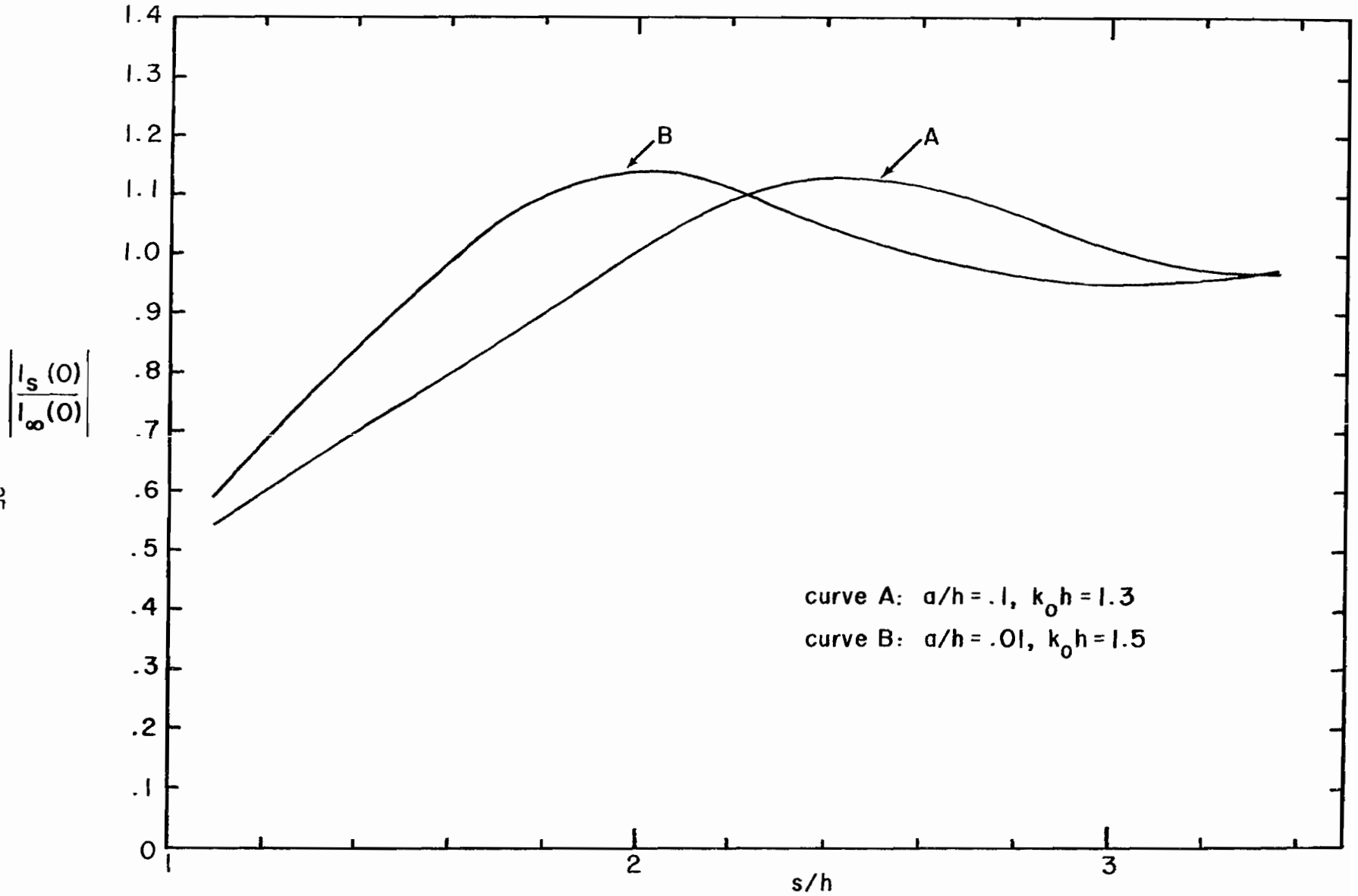

Figure 2.6. Post current at z = 0 versus plate separation around the resonant frequency.

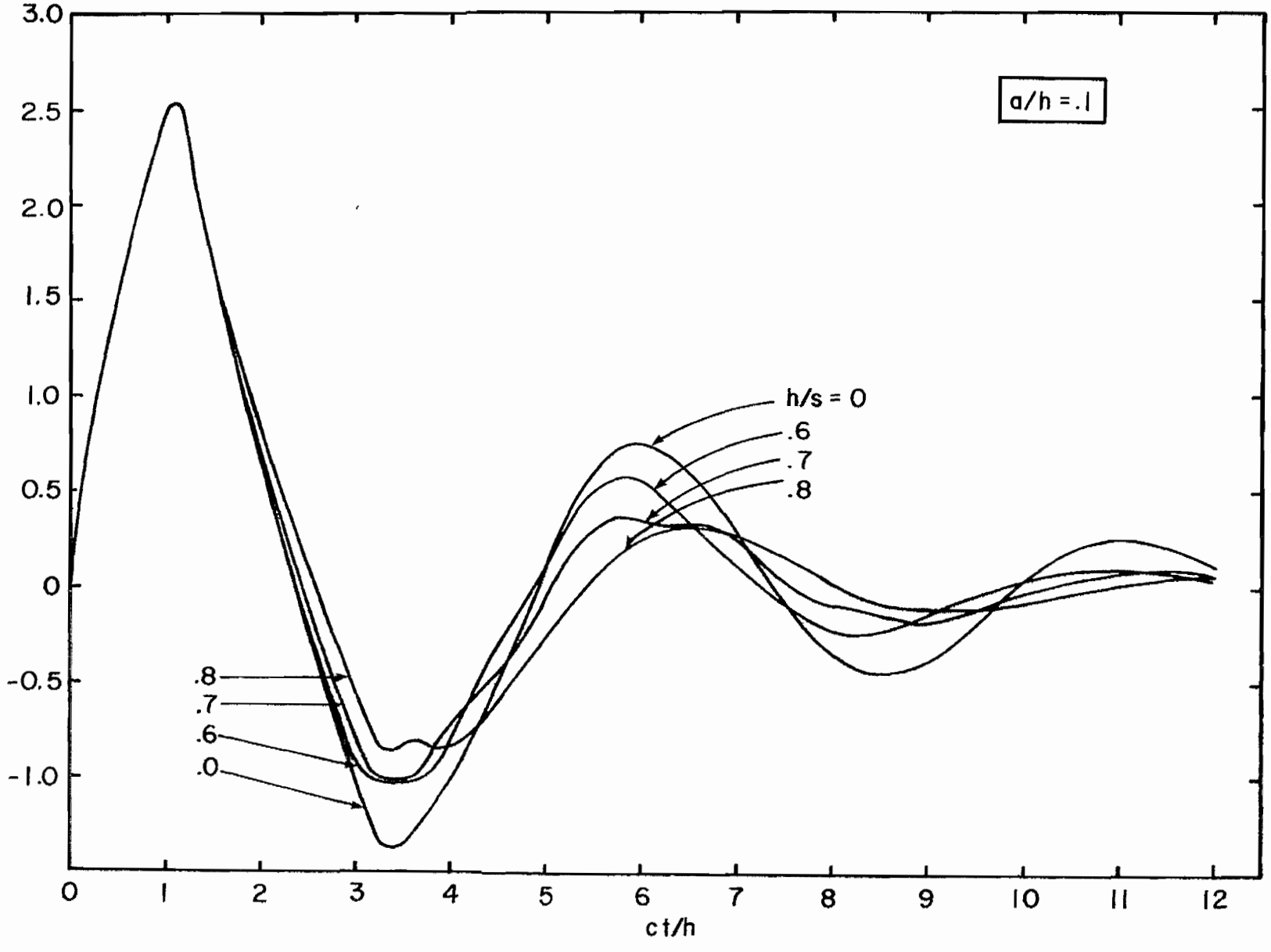

Figure 2.7. Time history of post current at z = 0 with plate separation as parameter.

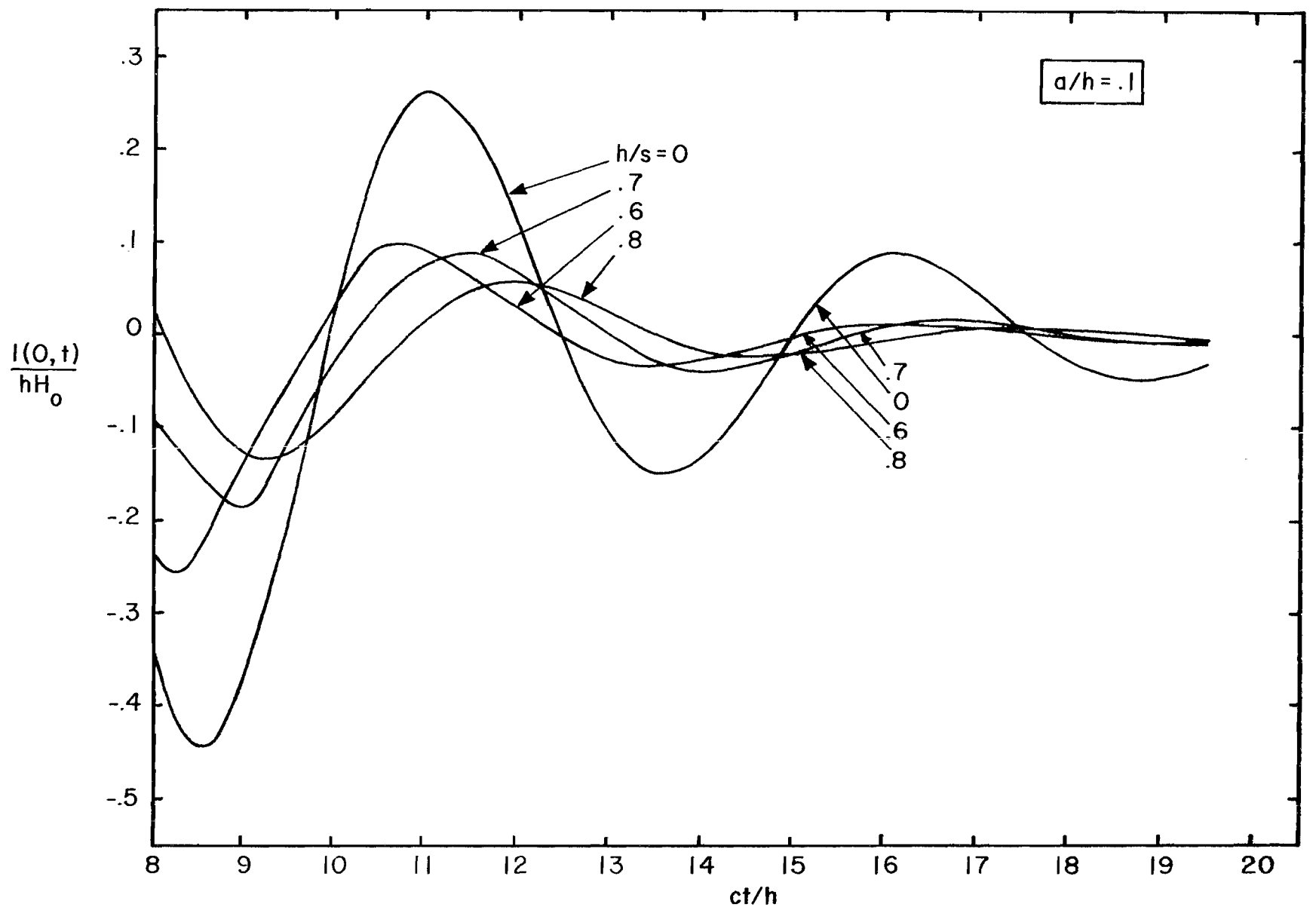

Figure 2.8. Time history of post current at z = 0 with plate separation as parameter.

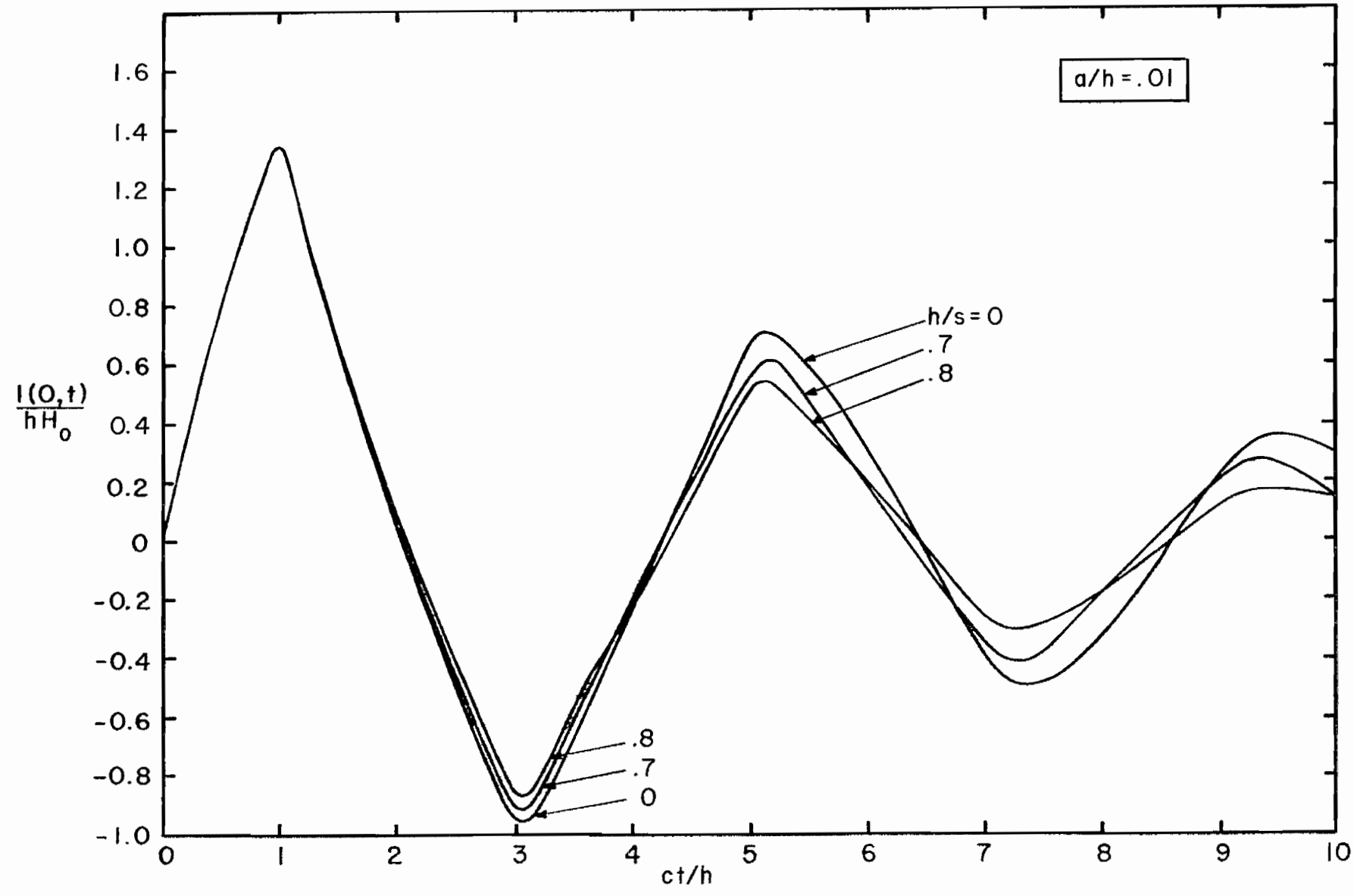

Figure 2.9. Time history of post current at z = 0 with plate separation as parameter.

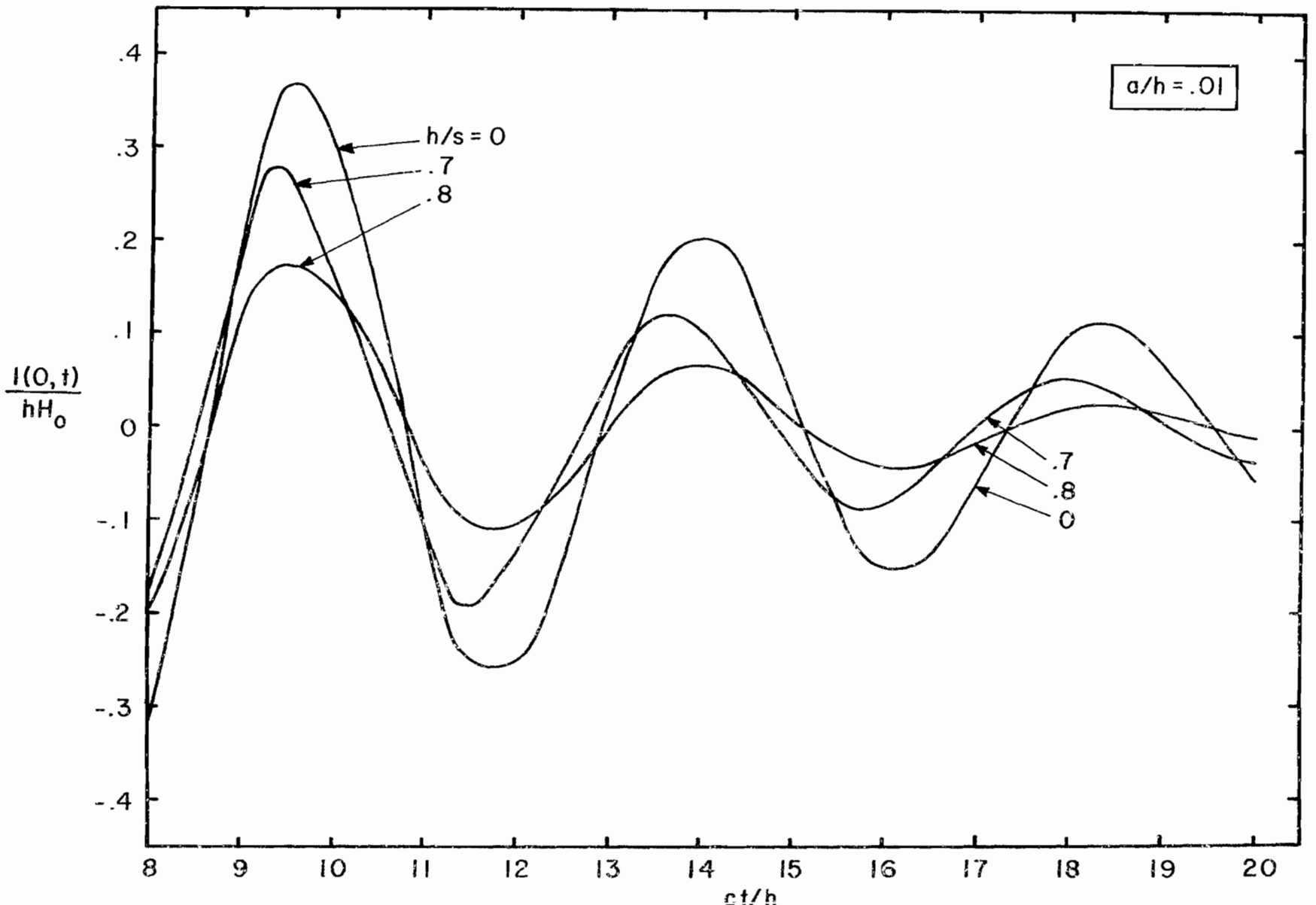

Figure 2.10. Time history of post current at z = 0 with plate separation as parameter.

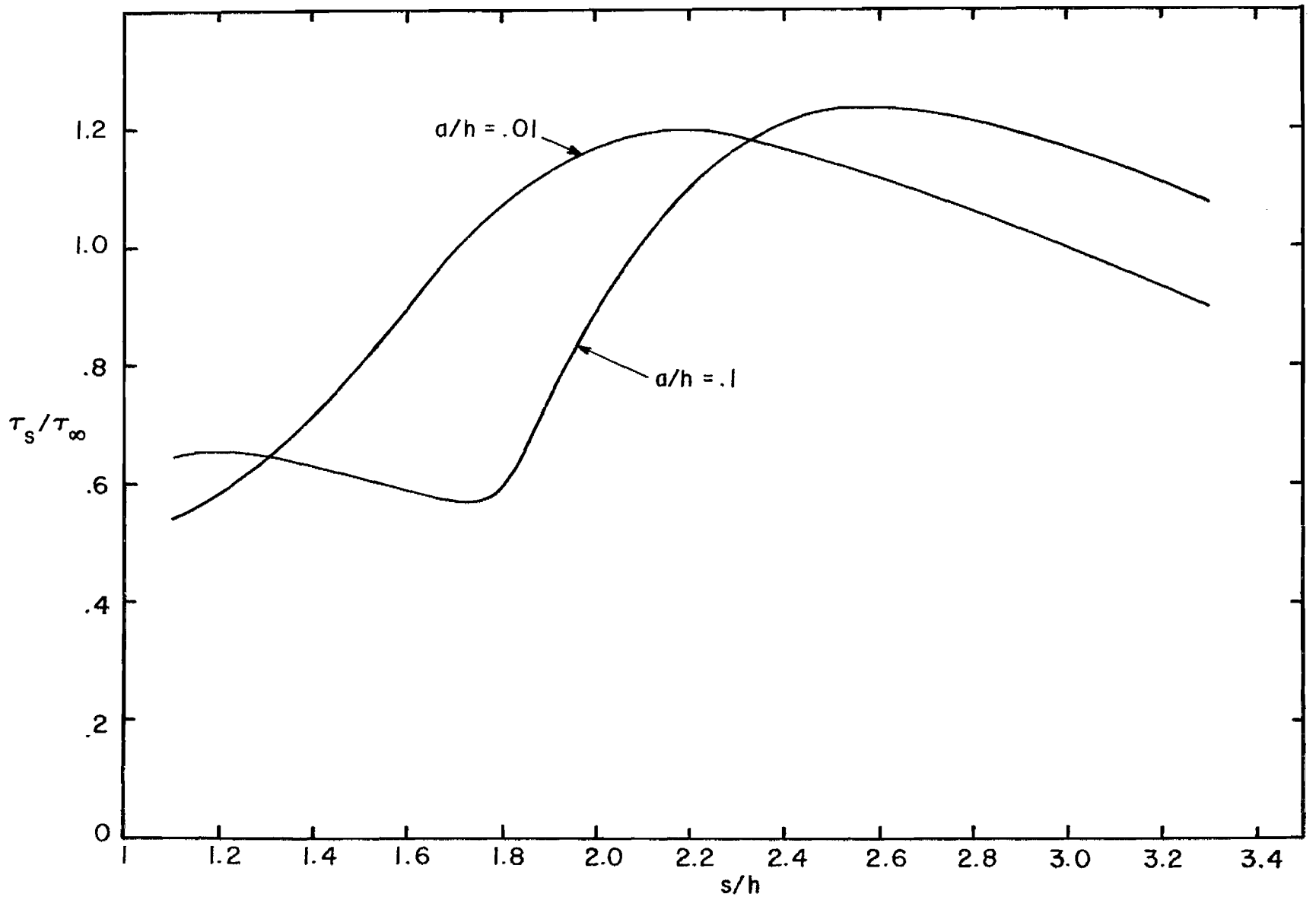

Figure 2.11. Decay time versus plate separation (as s/h increases, the curves oscillate about unity with decreasing amplitudes).

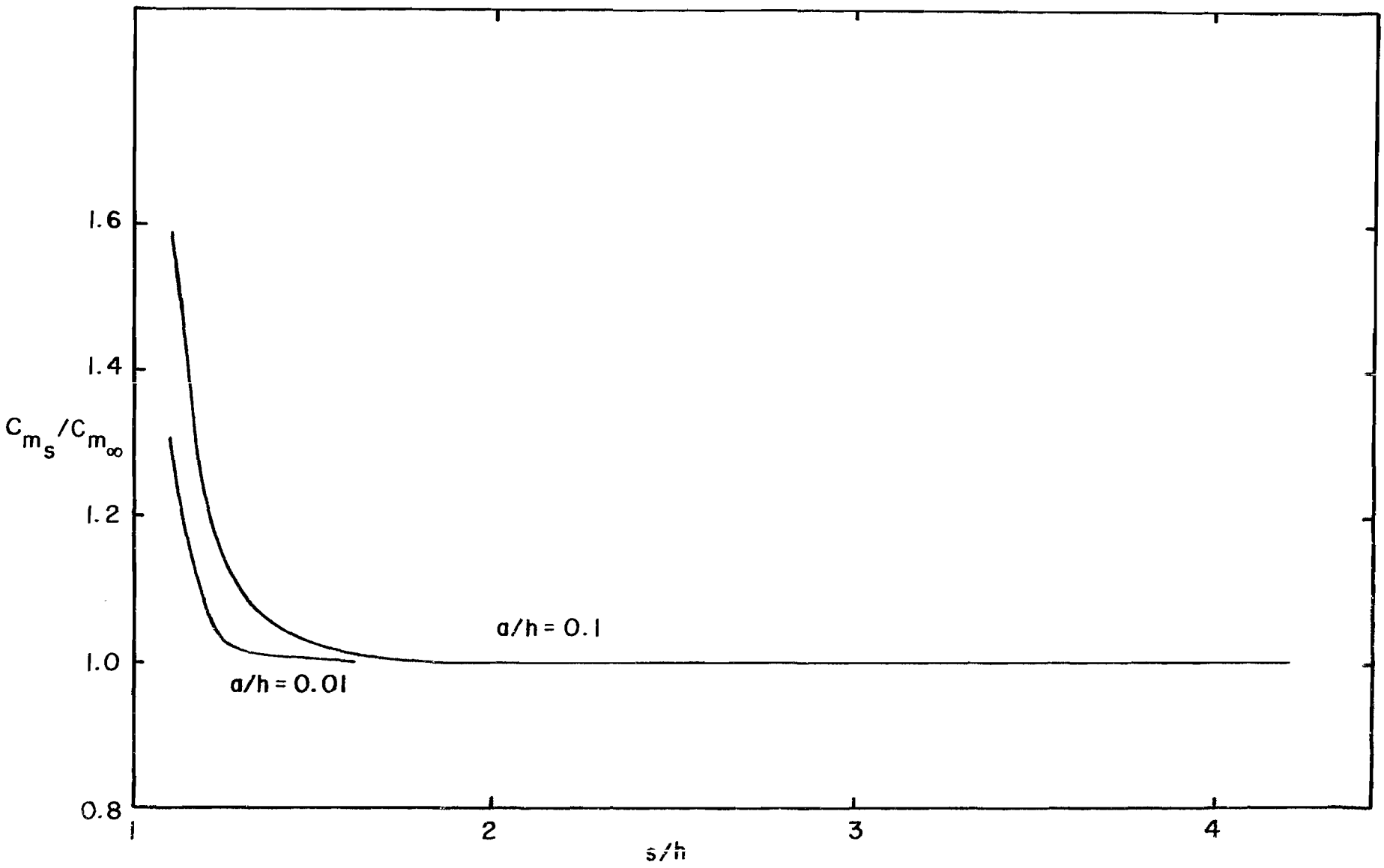

Figure 2.12. Charge density ratio at time of first current reversal.

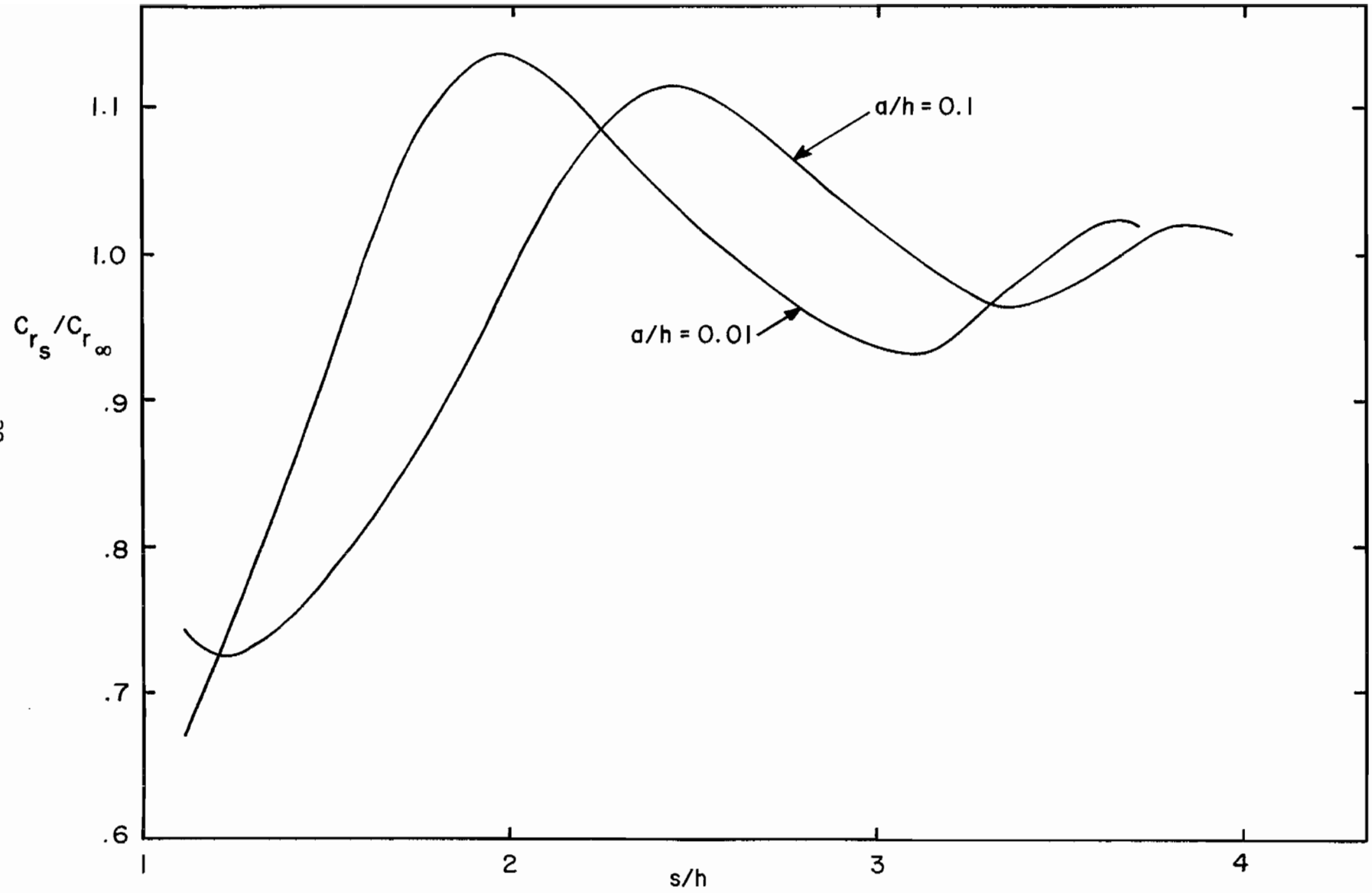

Figure 2.13. Charge density ratio at resonant frequency.

III. Interaction of Test Aircraft with the Earth near Resonant Frequencies

Reference 45 deals with the problem of approximating the EM interactions between an aircraft and the ground, thus comparing the aircraft's response near the ground to its response in free space (i.e., in-flight). Two intersecting cylinders forming an L-shaped body (L-wire) were used as a model of an actual aircraft.

Although a complete parameter study and final report on the response of the L-wire above a ground has not been completed, some data has been compiled, both in frequency and time domain, for various heights above the ground. The results of this data, as it applies to the ATLAS simulator, will be summarized here.

First of all a few words should be said as to the applicability of the L-wire model. The incident field is assumed to be vertically polarized, so there is some question as to how well this data applies. However, if one examines the problem a little more closely, it can be seen that the interaction between the L-wire and the ground is primarily a function of the geometry of the configurations rather than the method of excitation. It will be admitted, however, that applying the results of a calculation for a vertically polarized incident field to a horizontally polarized simulator is a rather crude approximation. At the present time, though, very little information exists that would give us any better data. In any event, the resonant frequencies (including damping constants to give the complex natural frequencies) are not changed by the form of the incident field; the amplitudes of these resonances are affected.

Also, the L-wire calculation does not include the effects of the wings and horizontal stabilizers that are present on an actual aircraft. It is merely chosen as a simple structure to indicate the change in the object response due to the presence of the ground.

For the calculations described here, sizes appropriate to a C-5A aircraft were chosen for the L-wire dimensions and both time and frequency domain responses were calculated for a variety of heights above the ground ranging from 10 meters to 40 meters. In addition, the free space response (far above the ground) was calculated as a baseline for comparison purposes. For time domain calculations both step function and double exponential input waveforms were considered. Graphs showing these results at several representative points on the L-wire are attached. The vertical scales give the current in amperes for an incident field with a peak strength of 1 volt/meter and the double-exponential input was assumed to have a risetime of 10 nanoseconds and a fall-time of 500 nanoseconds.

A few generalizations regarding the information in these plots can easily be made. First of all, note that the plots of the magnitude of the current in frequency domain are all similar in that peaks corresponding to the first three resonances of the L-wire structure appear. The exact shape and height of these resonant peaks, however, is highly dependent on the height of the L-wire above the ground. These variations with height are particularly noticeable at the two lower frequency resonances. This result is reasonable in that one intuitively expects the low frequencies to "see the ground" better than high frequencies would. Variations in the peak value of the first resonance may be up to 50% above the free space value.

Now consider what these frequency domain variations do to the time domain response. Both step-function and double-exponential input waveforms were considered by the use of convolution techniques. By comparing the time-domain current plots one can see that, at trestle heights of 35 and 45 meters, the ground has little effect on the early time portion of the L-wire response. The response is roughly approximated by a damped sinusoid and it is only at about the second or third peak that ground effects tend to cause variations in the L-wire response (as compared to free space). Since the current has decayed considerably from the first peak by the time these later peaks appear, the ground causes only minor differences in the L-wire time response for trestle heights of 35 and 45 meters. More quantitatively, these variations due to the ground are about 10 percent of the peak current at the first resonance. These conclusions are based primarily on the double-exponential input pulse. The step-function time responses vary somewhat from the double exponential but again, the response for a height of 35 meters above the ground is almost the same as free space. Generally the damping constant is more significantly affected but the present data are not adequate to quantify this well.

Thus one can summarize these results by saying that little deviation from free space is expected in the time domain skin current responses of aircraft for ATLAS I design 1 (45 meter platform) or ATLAS I design 2 (36 meter platform). In the frequency domain the presence of the ground increases the magnitude of some of the resonance peaks and decreases others. Thus, one would expect that further study might be needed to evaluate the effects on systems vulnerability tests of enhanced or decreased energy at certain frequencies.

Note that these results are for the current. Charge per unit length is also important. However, results for the charge per unit length on an L-wire in the presence of a ground plane are not yet available. Generally one expects the deviation of the charge per unit length to be about the same deviation of the current associated with the ground presence.

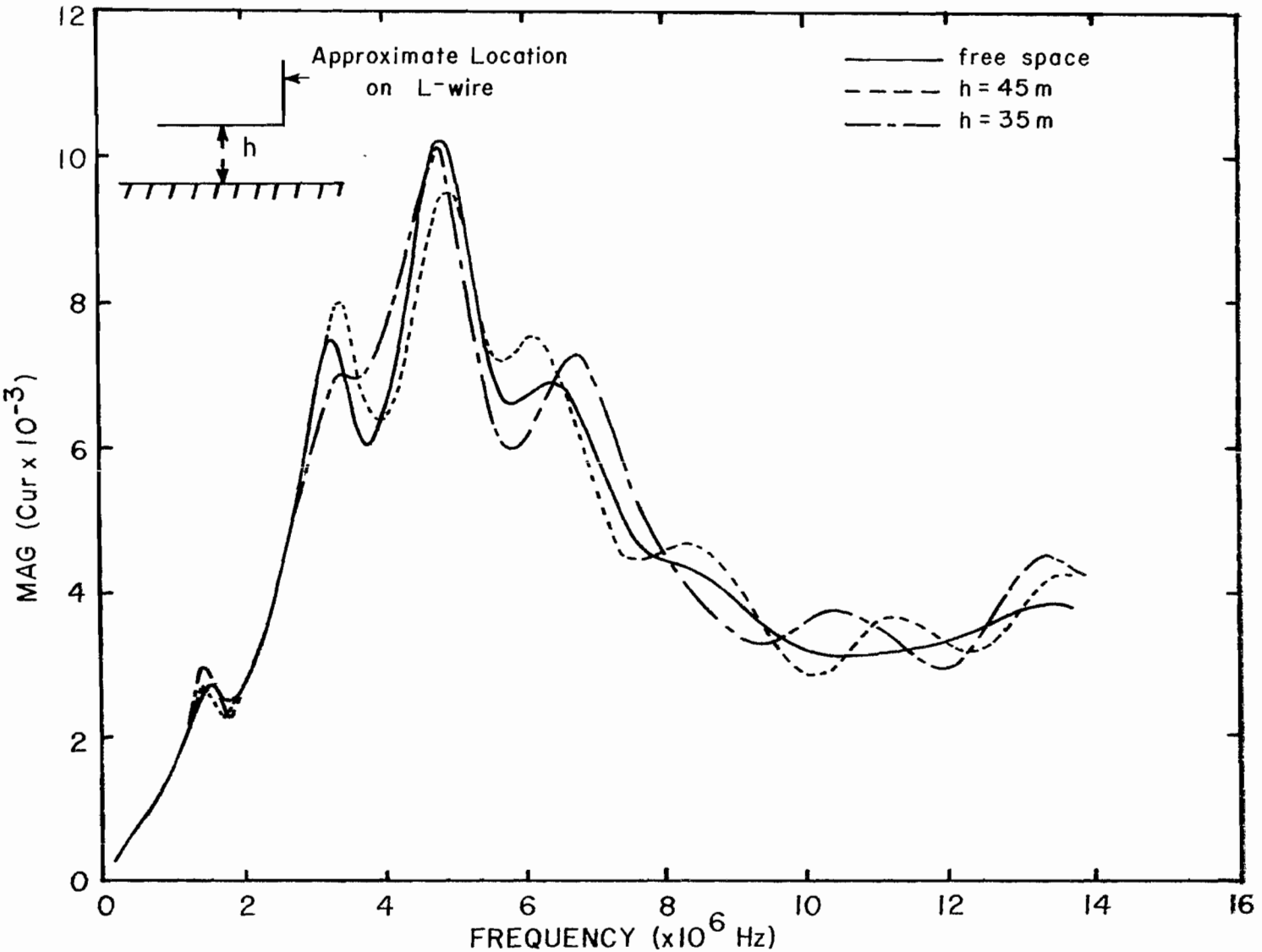

Figure 3.1. Magnitude of L-wire frequency domain response.

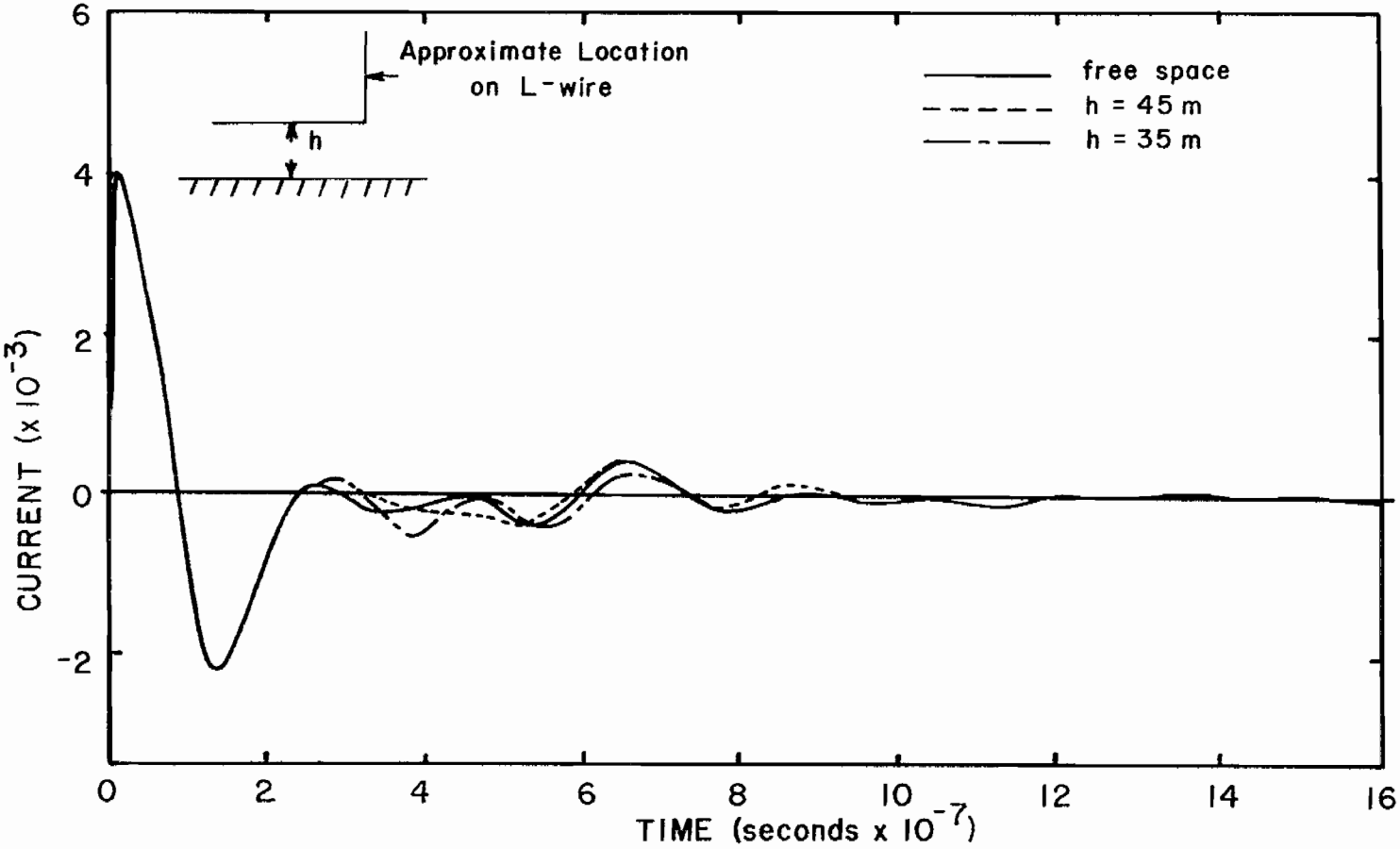

Figure 3.2. L-wire time domain response (double exponential input).

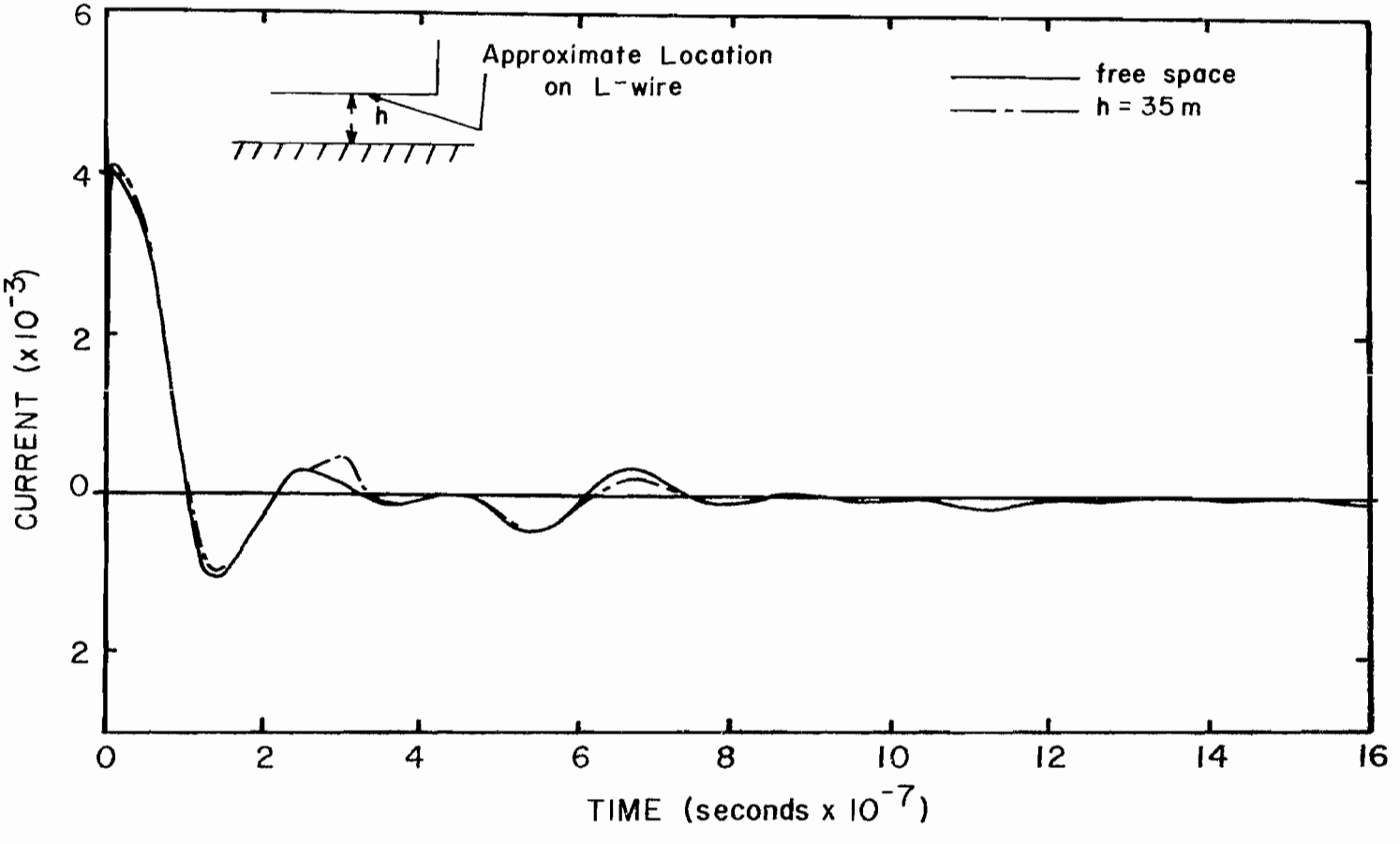

Figure 3.3. L-wire time domain response (step function input).

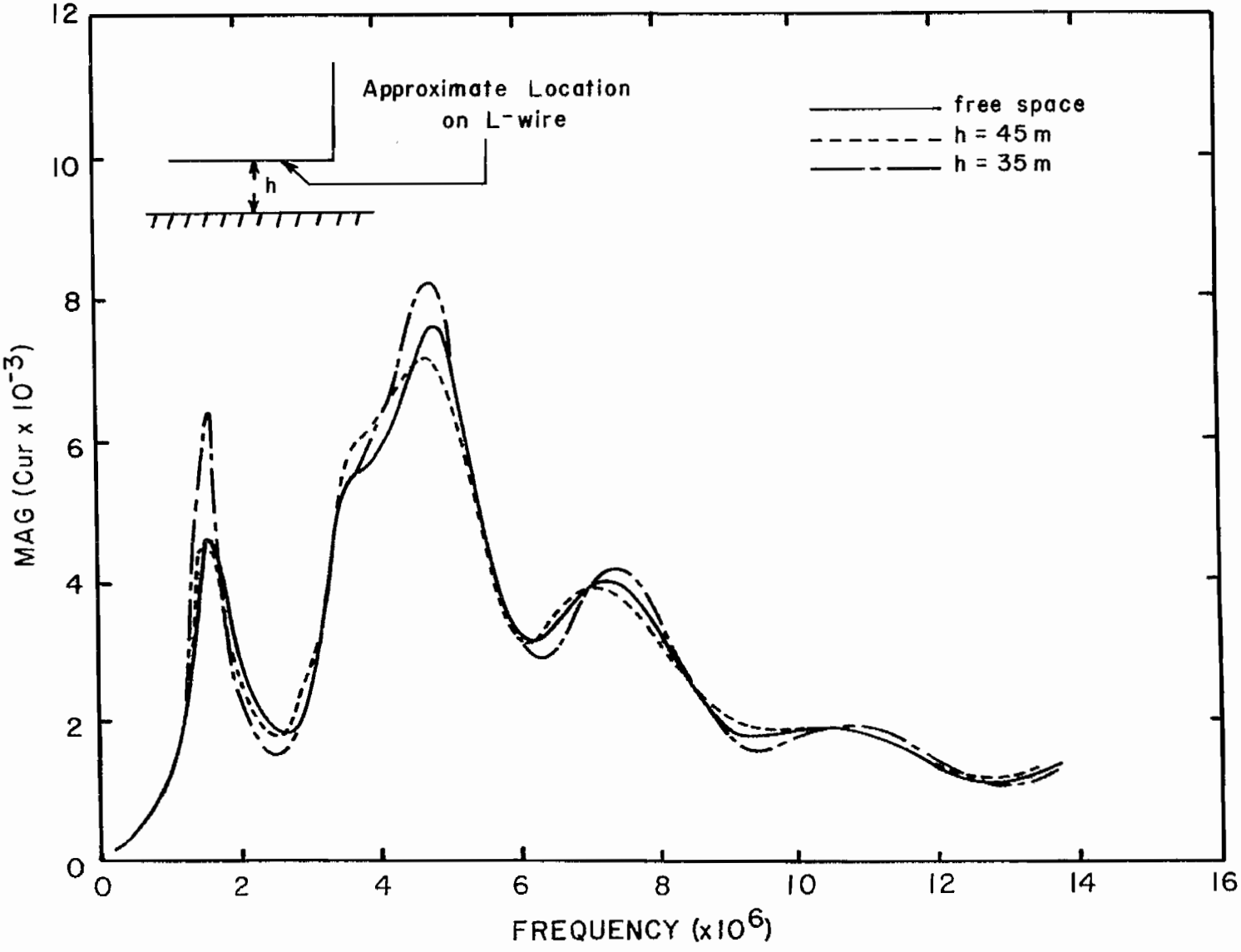

Figure 3.4. Magnitude of L-wire frequency domain response.

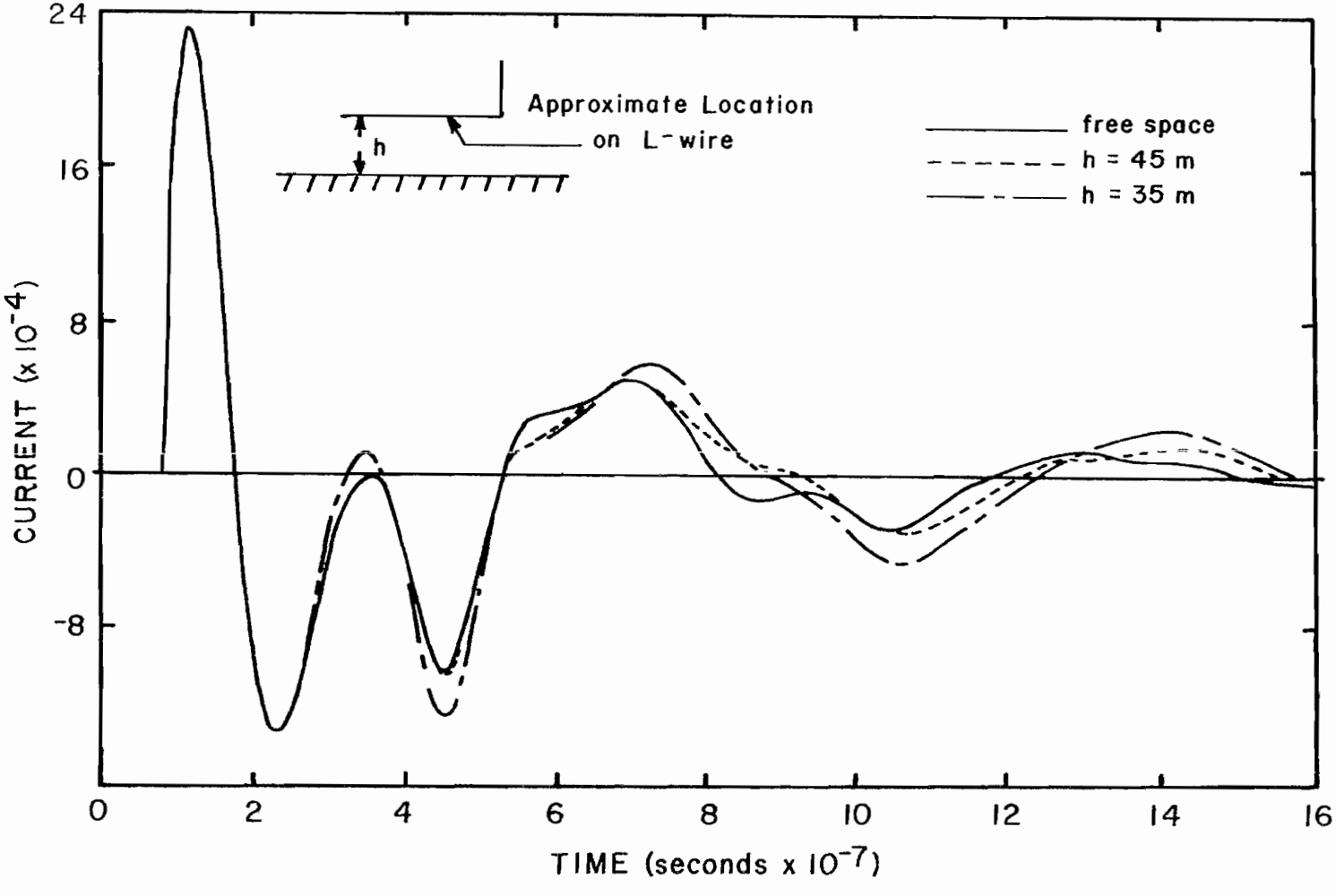

Figure 3.5. L-wire time domain response (double exponential input).

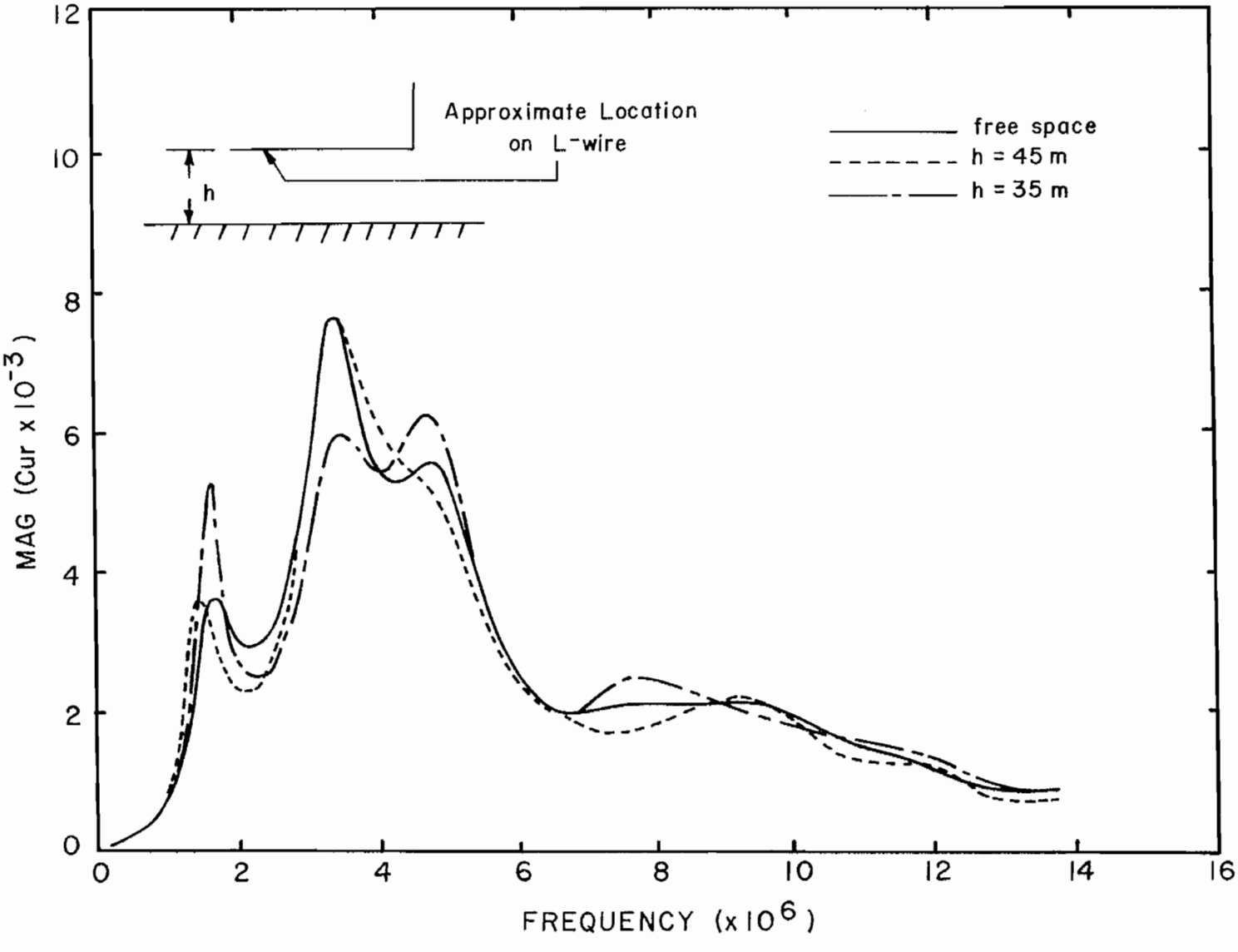

Figure 3.6. Magnitude of L-wire frequency domain response.

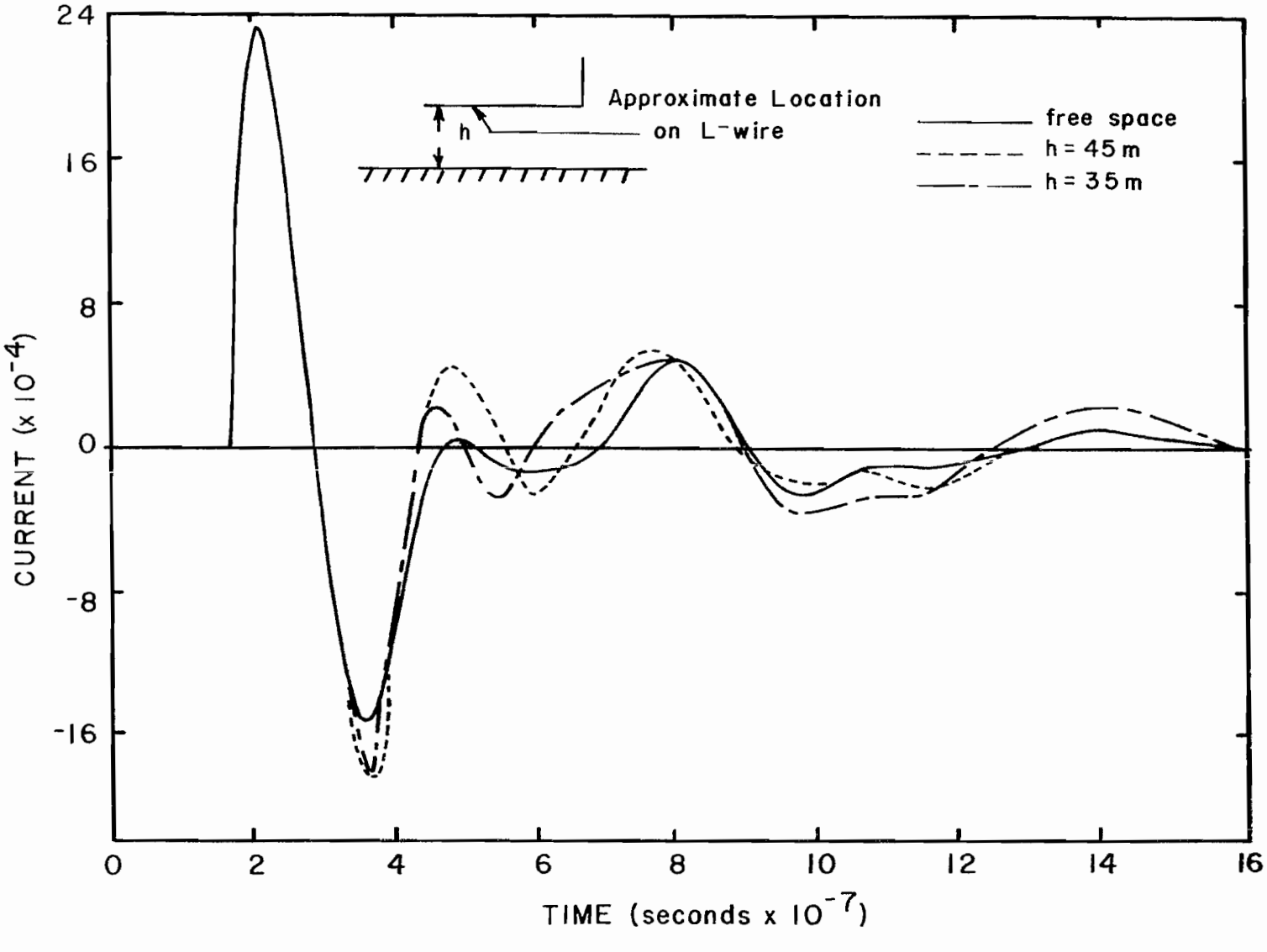

Figure 3.7. L-wire time domain response (double exponential input).

IV. Low Frequency Field Uniformity and Pulser Voltage Calculations

One of the primary electromagnetic questions concerning the use of a horizontally polarized transmission line for the simulator is the effect of the nearby ground. The actual earth under the simulator is a very complex structure electromagnetically with a highly frequency dependent conductivity and dielectric constant. However, a first-order cut at the problem can be made by considering the ground to be a flat, perfectly conducting plane.

Since we are primarily interested in the perturbation of the fields and impedance associated with the ground, such an approximation will still show the order of the change at a given cross section. If frequencies are low enough and the ground conductivity sufficiently small such that the skin depth in the ground becomes comparable to or larger than the typical cross section dimensions, then the magnetic field significantly penetrates into the ground and is thereby less distorted by the ground on the cross section considered. This approximation is most accurate for low frequency electric fields. With this assumption, the usual method of considering TEM fields of a transmission line by solving Laplace's equation for a potential can be used. (See references 2, 3.) Note that the low frequency propagation is not included in these calculations on a cross section.

As mentioned in reference 39 a method has been developed for numerically solving for the TEM mode potential and field distributions of a parallel plate transmission line above a perfectly conducting ground. Each plate is assumed to consist of 51 1/4" diameter parallel wires, all at the same potential. (The number and size of wires was chosen somewhat arbitrarily but these parameters do give field values and impedances within a few percent of those given in SSN 21 for a parallel plate line in free space.) The method of solution basically consists of superpositioning the static field of a number of parallel thin wires with a given charge per unit length. The potential on the n^{th} wire is given by

$$U_n = \sum_m p_{nm} q_m \tag{4.1}$$

where q_m is the charge on the m^{th} wire and we are summing over all the wires. Each p_{nm} is a function of wire location only and is called Maxwell's capacitance coefficient. (See reference 39.) The matrix formed by p_{nm} can be inverted to give an expression for the charge on each wire, given the potential; i.e.,

$$q_m = \sum_n K_{nm} U_n \qquad (4.2)$$

where K_{nm} is an element of the inverted p_{nm} matrix. Once we know the charge on each wire so that all the wires in a given plate are at the same potential, superposition can be used to give the potential (and thus the electric field) at any point in space.

This technique was used to calculate the low frequency (i.e., quasi-static) TEM mode field distribution for the specific dimensions of ATLAS I design 1. The results are shown in figures 4.1-4.4.

Note that these calculations apply strictly only at late times in the pulse. Diffraction effects add correction terms to the "static" fields in the earlier-time portion of the pulse shape.

An approximate "characteristic time" which divides the time interval when the static field approximation is fairly good from the interval when significant diffraction effects can be expected is the transit time between the simulator plates. In design 1, the plate spacing spanning the working volume is 125 meters, so this "characteristic time" can be taken as 415 nanoseconds. Since the pulse's e-folding time will be about 500 ns, the static field approximation only applies rather late in the pulse, and cannot be relied upon in the vicinity of the pulse's rise front. The early-time pulse behavior is discussed in other sections of this report. In this section, the "static" field data will be used to evaluate the system's behavior in a very approximate way.

The working volume is centered between the plates and has a radius of 75.7/2, or 37.8 meters. This is a normalized (x/a) value of 37.8/62.5, or 0.606. The top of the working volume is 20 meters above the floor, and corresponds to y/a = 35/62.5 = 0.56. The bottom of the working volume corresponds to y/a = 15/62.5 = .24. The shape of the working volume, as defined by these normalized coordinates, is mapped onto the normalized potential plot U(x,y) of figure 4.2.

The potential plot of figure 4.2 is used to calculate E_{AV}, the average E field across the working volume in the x (horizontal) direction. By symmetry of the simulator and working volume the electric field in the y (vertical) direction does not contribute to the vector average. To do this, the method of construction of figures 4.2, 4.3, and 4.4 must be understood. There are two normalizing calculations. The first of these is the length normalization, dividing all lengths by a = 62.5. The second is a field normalization, in which the x-component of electric field at the geometrical center of the plate system

(x = 0, y = 20 in figure 4.1), is set to 1.0. This geometrical center corresponds to x/a = 0, y/a = 0.32 in the normalized coordinates. Reference to figure 4.3 shows that E(x) is indeed 1.0 at the indicated coordinates.

If the field in the simulator were perfectly uniform, then the actual value of E(x) at the center (or anywhere else between the plates) would be:

$$E_{actual} = V/2a = V_o/a \tag{4.3}$$

Here V is the potential difference between the two plates, and V_o is the potential drop between one plate and ground (V = 0). But the simulator field is nonuniform, since the plates have finite width and are constructed of a number of parallel wires. Both of these departures from the ideal case of a smooth, infinitely wide plate system cause the electric field amplitude near the plates to exceed that on the central symmetry plane of the structure. Consequently, the actual electric field at the center point is less than the "uniform" field value. It is given by a modified form of (4.3):

$$E_{actual} = V_o/a \cdot f_e \text{ (x-component)} \tag{4.4}$$

Here, f_e is a factor less than unity, dependent only on the geometrical ratios of the simulator cross-sectional dimensions. In this case, the two defining ratios are (plate spacing/width) and (height above ground/plate spacing (or width)).

In the data plots, figure 4.3 shows the x-component of E in the normalized coordinate system with E (center) = 1.0. Now by the assumed symmetry of the plate system, the potential is zero both at the ground level, and everywhere on the vertical plane (x = 0) that divides the two simulator plates. Then the normalized potential on the horizontal center line (y = 20 meters) of the plate system, at some distance x = k meters from the vertical centerline (x = 0), would be:

$$U(k)_{\text{normalized}} = \int_o^k E(x)\,dx \equiv a\int_o^{k/a} E(x/a)\,d(x/a) \tag{4.5}$$

Equation 4.5 follows from the direct substitution of variable x/a for x. In (4.5), the potential is a "normalized" value, since by construction of the data, the value of E(x/a) at x = 0, y = 20 is 1.0. For the actual case, this central E field is given by equation 4.4, so the actual potential at x = k is just

the normalized potential of (4.5) multiplied by the actual central field value; this gives

$$U(k)_{\text{actual}} = V_o/a \cdot f_e \cdot a\int_o^{k/a} E(x/a)\,d(x/a) \tag{4.6}$$

or

$$U(k)_{\text{actual}} = V_o\left[f_e\int_o^{k/a} E(x/a)\,d(x/a)\right] \tag{4.7}$$

In (4.7), the term in brackets is the normalized potential function U(x,y) which is plotted in figure 4.2. For the plate geometry of the present system the "efficiency" factor f_e is 0.619. Now if we want to know the potential at the edge of the working volume (x/a = 0.6 or x = 37.8 meters) we see from figure 4.2 that the normalized potential assumes values from 0.42 to 0.44 for this value of (x/a) as one passes up the side of the working volume, from y/a of 0.24 to y/a of 0.56. Taking the average of these potentials, we have an approximation to (4.7) as

$$U(x = 37.8\text{ m})_{\text{actual}} = 0.43V_o \tag{4.8}$$

Then the average E field, in the x direction, over the extent of the working volume, is simply:

$$E_{AV} = \frac{U(x = 37.8)}{37.8} = \frac{0.43V_o}{37.8} \tag{4.9}$$

Letting the average field equal 200 kV/m the voltage of one pulser array, V_o, is, from (4.9)

$$V_o = \frac{E_{AV} \times 37.8}{0.43} = \frac{2 \times 3.78}{0.43}\text{ MV} = 17.6\text{ MV} \tag{4.10}$$

The normalized potential plots for other cross-sectional geometries can be similarly prepared, and these can be used in the above indicated way to yield directly the pulser array voltage required for a given working volume size and E_{AV} value.

Note that 200 kV/m is not precisely the average peak electric field given 17.6 MV peak voltage from each pulser. It is

the peak electric field under a transmission line approximation which is most accurate at low frequencies. The precise value of the peak is not that important anyway. This value of 200 kV/m with the transmission line approximation and a characteristic time for the pulse width (τ_d in reference 38) specify a lot more about the waveform than just the peak. In a frequency-domain sense this specifies the low frequency content (or complete time integral) of the pulse and roughly the break away from the low frequency asymptote as one moves up in frequency. The measured peak field may then be more or less than 200 kV/m depending on where one measures it or even if one averages it over a cross section of the working volume. Note that the initial rise characteristics of the pulser are rather complex (reference 38) so that even the TEM waveform launched on each input transition will not necessarily quite reach 17.6 MV.

A second method for calculating the pulser array voltages involves graphing the potential function U(x,y) as a function of x/a with y/a as a parameter. This data is plotted in figure 4.5 for y = 20 meters.

The level, y = 20, was chosen because it is 5 meters above the bottom of the working volume and is the region that would be occupied by the fuselage of an aircraft being tested and is of relatively greater interest. As a check, U(x,y) was also determined along the level y = 30 and it was found that there is practically no difference between the two plots within the limits of the working volume.

From figure 4.5 it can be seen that 43% of the potential drop between the plates of the transmission line occurs within the working volume. If we assume the electric field averages 200 kV/m across the 75.7 meter width of the working volume, the potential difference between the plates of the transmission line would be:

$$\Delta V = \frac{200 \text{ kV/m} \times 75.7 \text{ m}}{0.43} = 35.2 \text{ MV} \qquad (4.11)$$

Figures 4.3 and 4.4 are used to examine the uniformity of electric field over the working volume. These E(x/a) and E(y/a) plots are obtained by simply dividing the U values of figure 4.2 by the efficiency factor f_e and then differentiating the results directionally, as can be seen from equation 4.7. To discuss field uniformity, however, we can neglect scale factors and normalizations and work directly with the plotted field values of figures 4.3 and 4.4.

A reasonable measure of field uniformity is defined by

$$\alpha = \frac{|\vec{E} - \vec{E}_{AV}|}{|\vec{E}_{AV}|} \tag{4.12}$$

where $\vec{E}_{AV}$ is a vector with x-component only. Obviously, all normalizing scale factors divide out of equation 4.12.

An examination of figures 4.3 and 4.4 shows that the electric field deviates most strongly from the purely x-directed case at the upper and lower corners of the working volume. Quite near the center height of the working volume (y/a = 25/62.5 = 0.40) the E_y field component vanishes, as seen in figure 4.4. At the upper corner of the working volume (x/a ≃ 0.6, y/a = 0.56) we have the normalized field components:

$$E_x = 1.4 \; ; \quad E_y = -0.35 \tag{4.13}$$

Then

$$\vec{E} = 1.4\vec{i}_x - 0.35\vec{i}_y \tag{4.14}$$

Now we need E_{AV} in this normalized form. The definition of $|\vec{E}_{AV}|$ in the normalized system of units is:

$$|\vec{E}_{AV}| = \frac{1}{M}\int_o^M E(x/a)d(x/a) \; , \quad (0 < M < 1) \tag{4.15}$$

From equation 4.7, we see that the plot of normalized potential of figure 4.2 is simply:

$$U(k/a)_{\text{normalized}} = f_e\int_o^{k/a} E(x/a)d(x/a) \; , \quad (0 < k < a) \tag{4.16}$$

Making the substitution M = k/a, we have

$$U(M) = f_e\int_o^M E(x/a)d(x/a) \tag{4.17}$$

This identifies with (4.15), leading to

$$E_{AV}(y) \text{ (over range 0 to M)} = \frac{U(M)}{f_e \cdot M} \quad (M = x/a) \tag{4.18}$$

We have, as an approximate average over the side of the working volume, a value of 0.43 for U(0.6), and $f_e = 0.619$, so

$$E_{AV} = \frac{U(0.6)}{0.619 \times 0.6} = \frac{0.43}{0.372} = 1.15 \tag{4.19}$$

Then, for use in the uniformity calculation of (4.12), $\vec{E}_{AV}$ is

$$\vec{E}_{AV} \equiv 1.15\vec{i}_x \tag{4.20}$$

Using (4.14)and (4.20) in (4.12), one finds

$$\alpha = \frac{|0.24\vec{i}_x - .35\vec{i}_y|}{1.15} = 0.37 \tag{4.21}$$

So the field deviates 37 percent from the uniform value, under the uniformity definition of equation 4.12. At the lower corner of the working volume, we have almost the same result; using figures 4.2, 4.3, and 4.4 in the indicated way, we find a 47 percent departure from uniformity. Similarly, across the (horizontal) centerline of the working volume, the deviation is found to be 32.5 percent; this is a better field uniformity, as we would expect, since the y-component of E is small along the centerline of the working volume.

The measure of field uniformity, as defined above, has been calculated at several points in the working volume and the results are summarized in the table below.

	x/a=0.0	x/a=0.2	x/a=0.4	x/a=0.6
Bottom of Working Volume y/a = 0.24	17.4%	16.1%	19.8%	44.4%
Middle of Working Volume y/a = 0.40	15.7%	11.7%	2.9%	30.6%
Top of Working Volume y/a = 0.56	12.9%	10.4%	12.4%	38.0%

Table 4.1

Uniformity deviations - ATLAS I design 1

(These numbers vary slightly from those given above. The numbers used in constructing the table were taken directly from computer output rather than read off graphs and therefore should be more accurate.)

Note that the low frequency fields are most uniform at some point about two-thirds of the way from the center of the working volume out to the outer edge (along a horizontal line). This is because we have defined our uniformity with respect to an "average" electric field rather than the field at the center, and the minimum uniformity deviation occurs where the field is closest to "average."

As will be seen later the effects of diffraction tend to compensate for the non-uniformity of the fields during the first part of the simulator pulse.

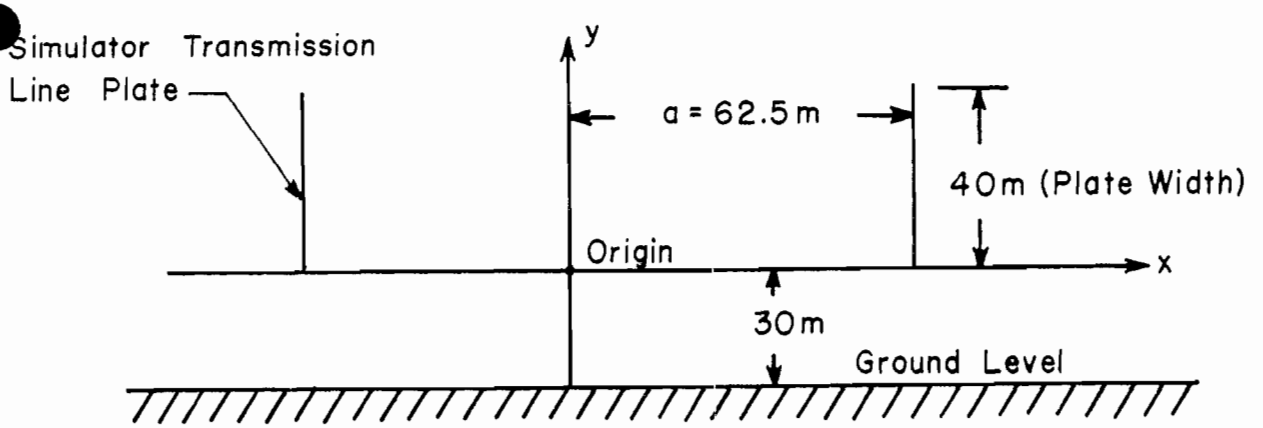

Figure 4.1. Cross section of transmission line.

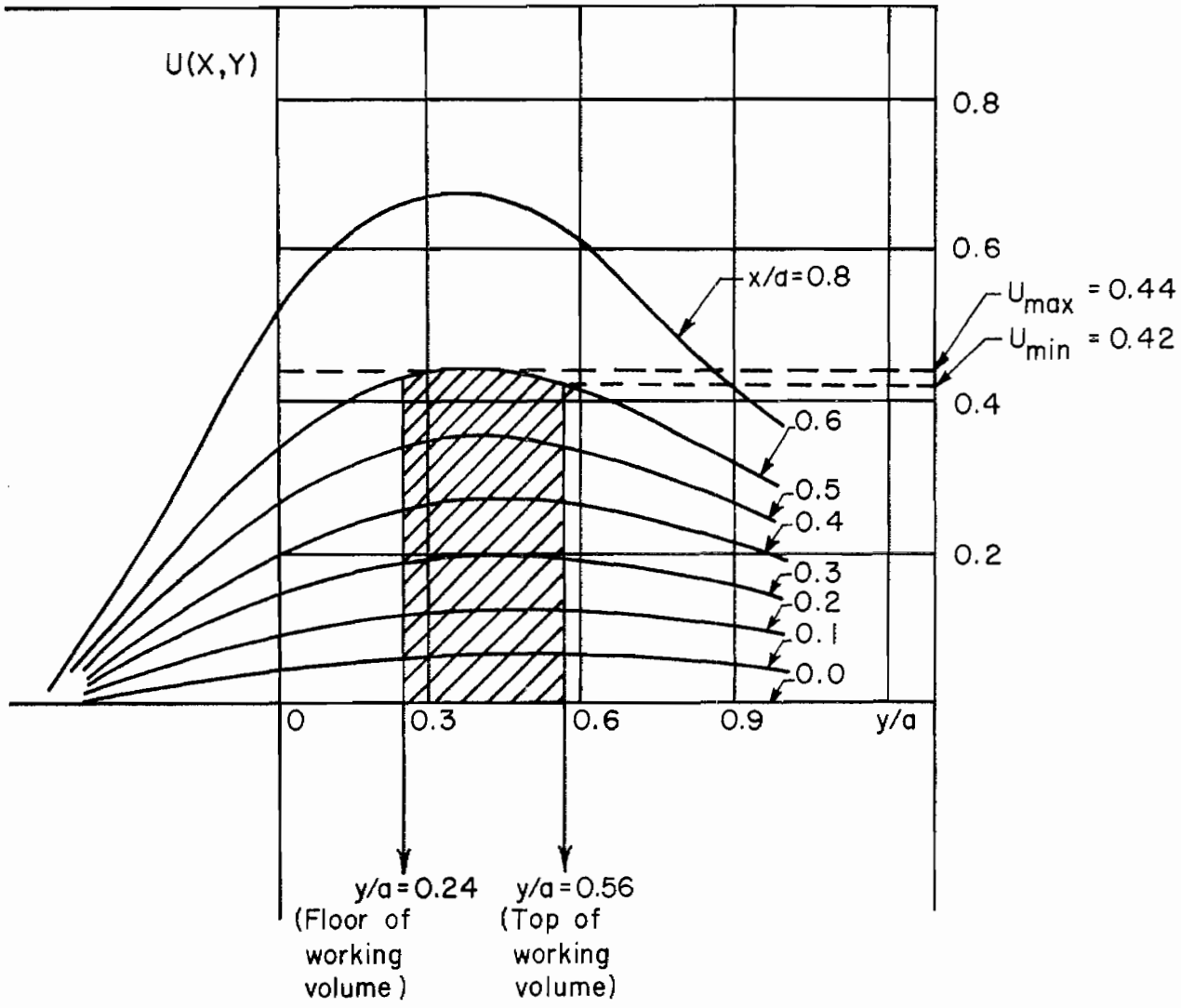

Figure 4.2. Normalized potential vs height (y/a).

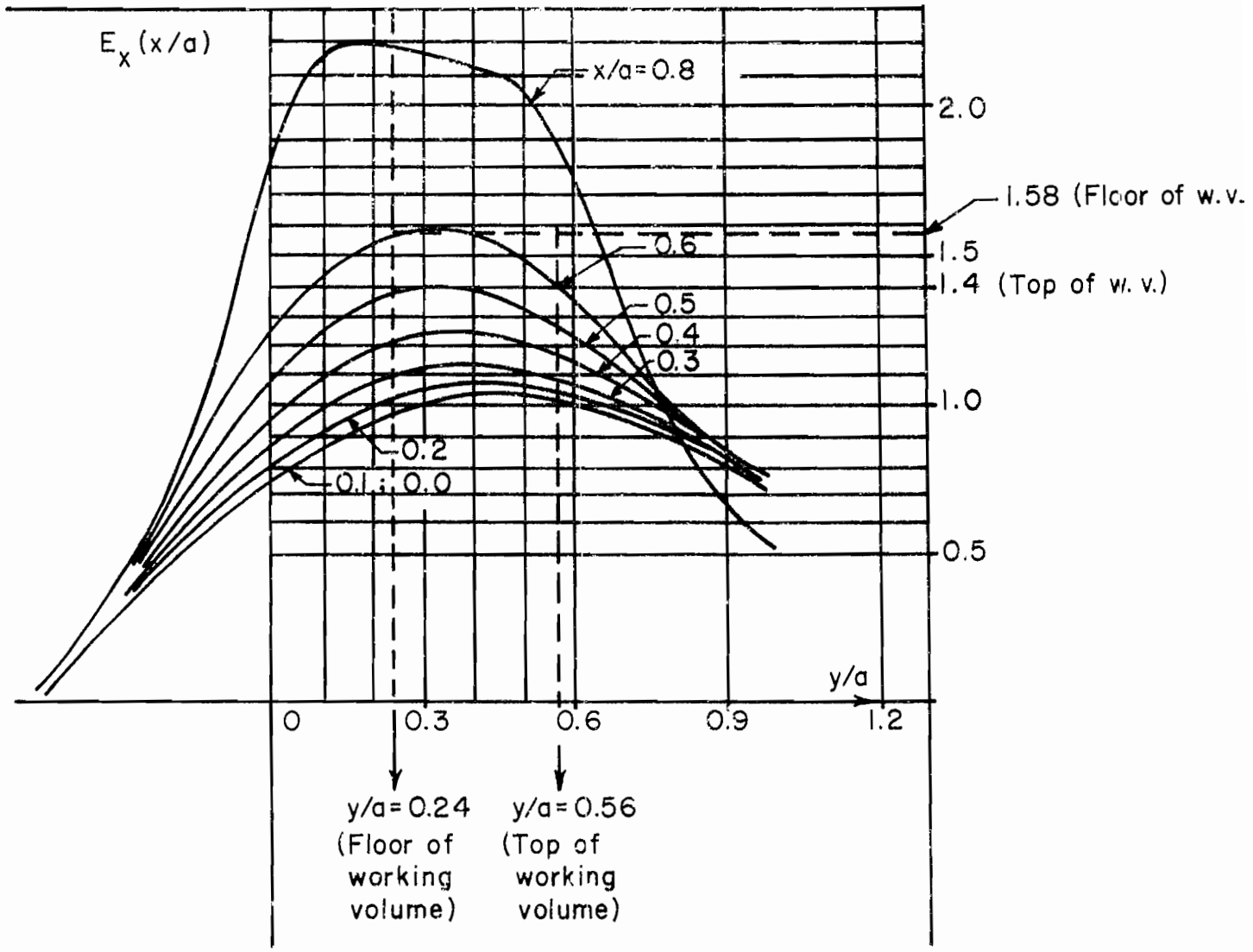

Figure 4.3. Normalized E_x vs height (y/a).

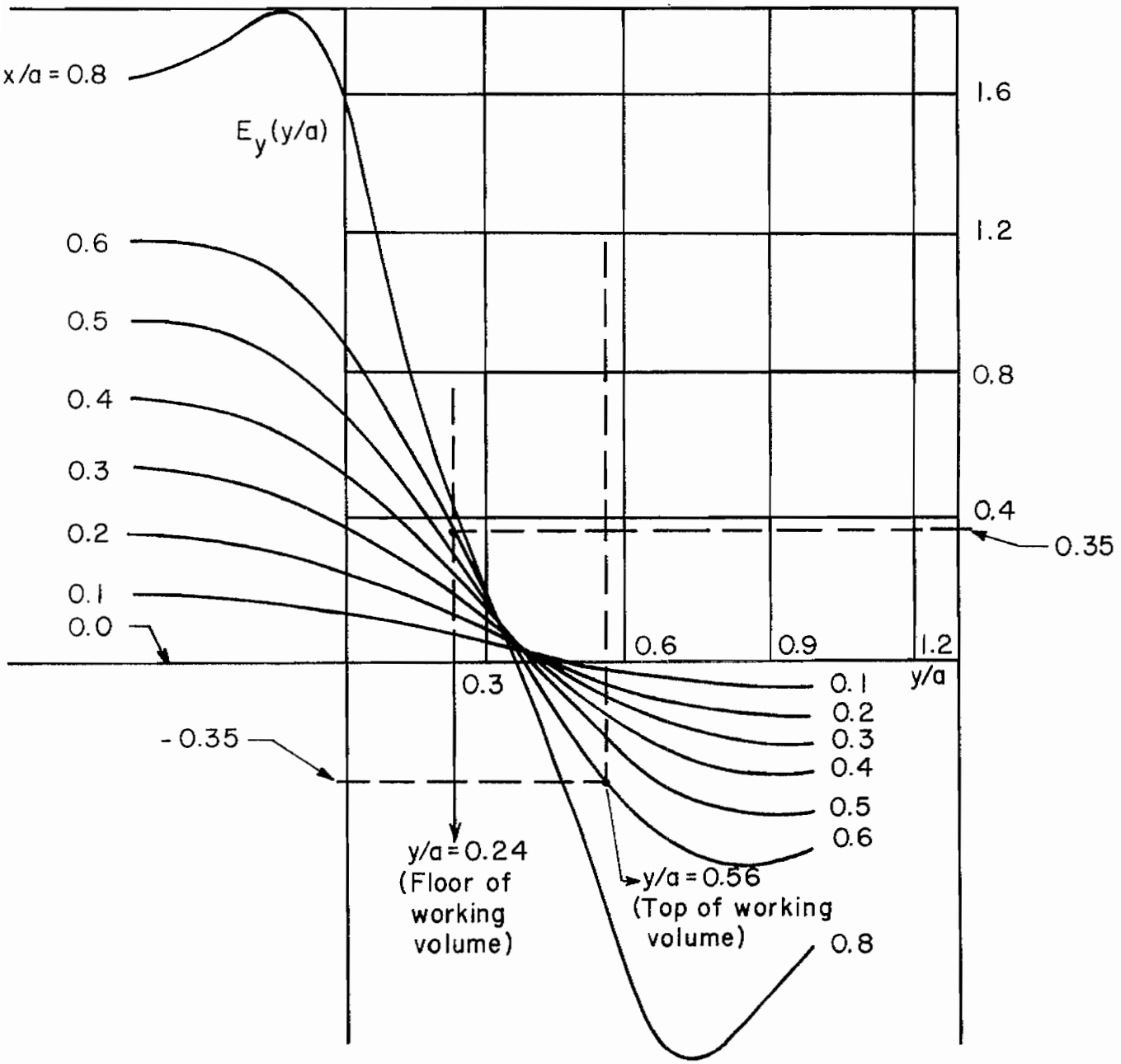

Figure 4.4. Normalized E_y vs height (y/a).

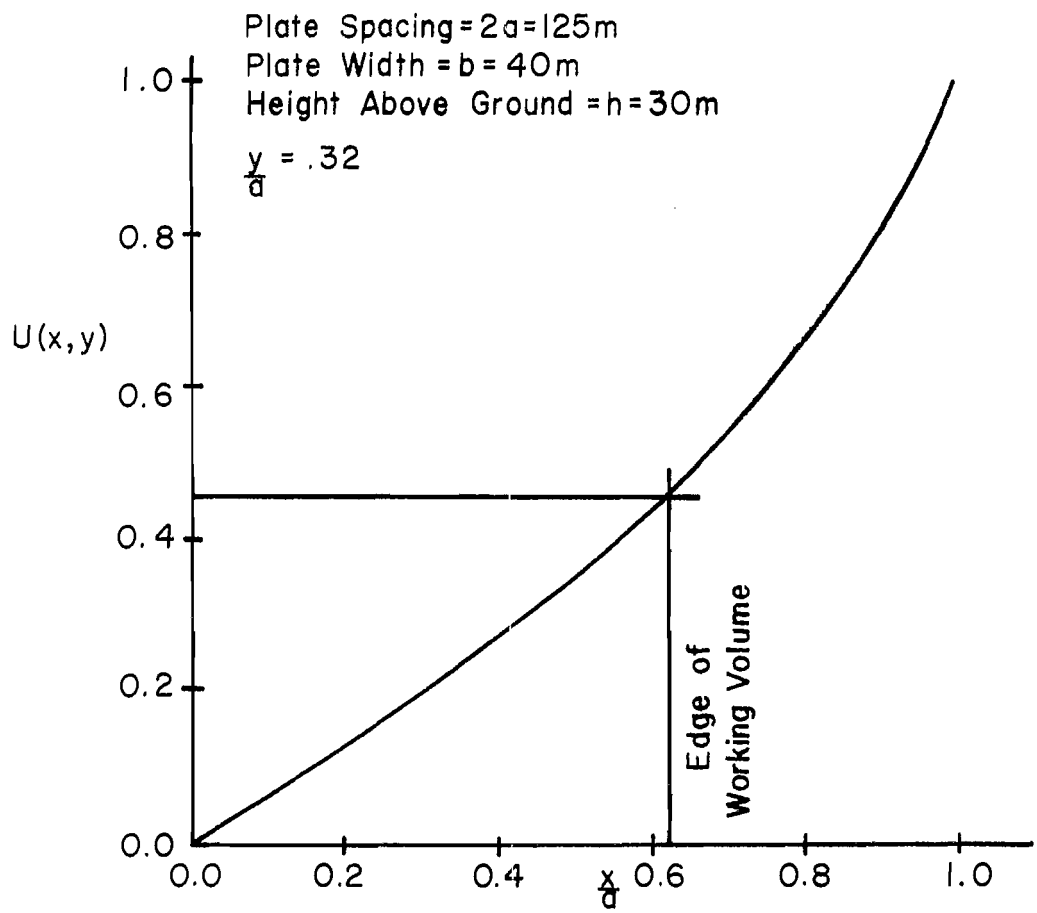

Figure 4.5. Potential distribution

V. Transmission Line Impedance

Differential Mode Impedance

The impedance of a transmission line is related to the characteristic impedance of free-space by equation 5.1, in cases when only the TEM mode is present and the concept of impedance is well defined.

$$Z = f_g \sqrt{\frac{\mu}{\varepsilon}} \simeq 120\pi f_g \quad \text{(for vacuum)} \tag{5.1}$$

The geometrical factor, f_g, is a function of the location of the conductors of the transmission line only. For the design 1 cross-sectional geometry, the geometrical factor is calculated to be 0.686 using the technique discussed in reference 39. [A recent set of calculations giving f_g for various parameters is shown in figure 5.1.] Then the characteristic impedance of the transmission line is 258 ohms in the differential mode. If this transmission line were located in free-space, very far removed from the ground plane, its impedance would be significantly higher. References 2 and 8 provide data covering this case. The most directly applicable data is given in reference 8 in tabular form. For a plate spacing/width ratio of 125/40, or 3.125, the value of f_g given in reference 8 is 0.806. So the free-space impedance of the transmission line would be 304 ohms. The presence of the ground then lowers the transmission line impedance by 46 ohms, or 15 percent of the free-space value.

The significance of ground effect perturbation on the characteristic impedance is twofold. First, the larger the ground effect on Z, the greater the high-frequency pulse energy lost in and reflected from the ground can be expected to be. A detailed analysis of this situation has not yet been published, so it is difficult to determine the relative significance of a 15 percent ground effect perturbation as opposed to a 10 percent perturbation.

All of the calculations thus far have assumed an infinitely conducting ground in order to make the problem tractable. However, one can at least estimate the effects of a finitely conducting ground in the limit of low frequency. One should note that the transmission line equations are really only valid for wavelengths large compared to the cross-sectional dimensions of the line; i.e., the expressions derived here are good only for low frequencies anyway.

In the static limit, a finitely conducting ground appears as a perfect conductor to electric fields, while it is essentially invisible to magnetic fields, assuming the permeability

of the ground is the same as that of free space, i.e., μ_o. Thus, one can estimate the effect of a finitely conducting ground on a horizontally polarized transmission line by assuming the ground is perfectly conducting for electric field calculations and absent for magnetic field considerations. This is equivalent to using a perfectly conducting ground to calculate C', the capacitance per unit length of the line, and ignoring the ground when calculating L', the inductance per unit length. Since the pulse impedance of a transmission line, Z, is given by

$$Z = \sqrt{\frac{L'}{C'}} \tag{5.2}$$

one can use L' and C' to approximate the impedance of a line above a finitely conducting ground.

Remembering that we are considering only the static limit,

$$L' = \mu_o f_{g_{FS}} \tag{5.3}$$

$$C' = \frac{\varepsilon_o}{f_{g_{PCG}}} \tag{5.4}$$

Thus

$$Z_{FCG} \simeq \sqrt{\frac{\mu_o}{\varepsilon_o}} \left[f_{g_{FS}} f_{g_{PCG}} \right]^{1/2} \simeq 120\pi \left[f_{g_{FS}} f_{g_{PCG}} \right]^{1/2} \tag{5.5}$$

where

FS → free space

PCG → perfectly conducting ground

FCG → finitely conducting ground

and f_g is the geometrical factor for the transmission line with or without the ground as indicated by the subscript.

Since the presence of a ground decreases the geometrical factor of a transmission line,

$$Z_{FS} > Z_{FCG} > Z_{PCG} \tag{5.6}$$

neglecting losses in the ground. Note that with a finitely conducting ground we can no longer assume TEM mode propagation; i.e.,

$$\frac{|\vec{E}|}{|\vec{H}|} \neq \sqrt{\frac{\mu_o}{\varepsilon_o}} \simeq 377\Omega \tag{5.7}$$

Thus the above equations are only estimates with limited validity. However, plugging in the appropriate numbers,

$$Z_{FCG} = 120\pi\sqrt{(.806)(.686)} \simeq 281\Omega \tag{5.8}$$

which varies by only 7.6% from the value of 304 ohms for the free-space impedance of the line.

Common Mode Impedance

Figure 5.2a depicts the sources for ATLAS I. In this case, if $V_1 = V_2$ then the system will be symmetric about the ground point. That is

$$V_{BC} = V_2 = V_{AB} = V_1 \quad \text{and} \quad V_{AC} = V_1 + V_2 \tag{5.9}$$

To analyze the case where $V_1 \neq V_2$, we make use of the equivalent circuit shown in figure 5.2b. Here, as in figure 5.2a $V_{AC} = V_1$ and $V_{BC} = V_2$. The voltage $V_1 + V_2$ is the differential mode voltage and $1/2(V_2 - V_1)$ is the common mode voltage. To understand how these terms apply let us first consider figure 5.2c where we have the plates of the transmission line at equal but opposite voltages. This line has an impedance of Z_L from plate to plate. This impedance includes the fact that the ground is present and some field lines will go from a plate to ground and then to the other plate. The plate to plate impedance Z_L is the differential mode impedance Z_{DM}. In figure 5.2d we have each plate at the same voltage, the common mode voltage. One would like to know the impedance of the plates to ground. A close approximation, which neglects effects of the presence of the other plate, can be made with the use of SSN 42. The calculation that is done is the impedance between a plate and its image as shown in figure 5.3. This impedance (Z_g) is plotted in figure 5.4 as a function of x_o/x_1. The impedance from a plate to ground would be $Z_g/2$ from symmetry arguments. Thus the impedance from one plate to ground in figure 5.2d is approximately $Z_g/2$. This gives the approximate common mode impedance for the entire line as $Z_g/4$, since the two plates are connected in parallel. The use of this calculation technique

gives a common mode impedance of 69 ohms at a cross-section of the parallel plate section of the transmission line and an impedance of 82 ohms at the terminator location. The use of these calculations in properly designing the termination of the simulator will be discussed in another section of this report. The actual common mode impedance is somewhat larger than these estimates due to the mutual interaction of the two plates.

Use of Impedance

One should note that the very concept of impedance must be used with caution when applied to this simulator due to the size of the transmission line being considered. The impedance as defined in this report really only applies to TEM mode propagation and tells us little about the actual electromagnetic field distribution, especially at frequencies corresponding to wavelengths small with respect to the simulator's cross-sectional dimensions. Because of the finitely conducting ground, the assumed TEM mode is only an approximation and techniques using the impedance in various circuit models should only be considered first cut approximations of the real solution.

Impedance is used here in the form of the impedance change due to the ground presence. It is merely one more electromagnetic distortion parameter. Smaller impedance change means a better simulator from this one type of measure.

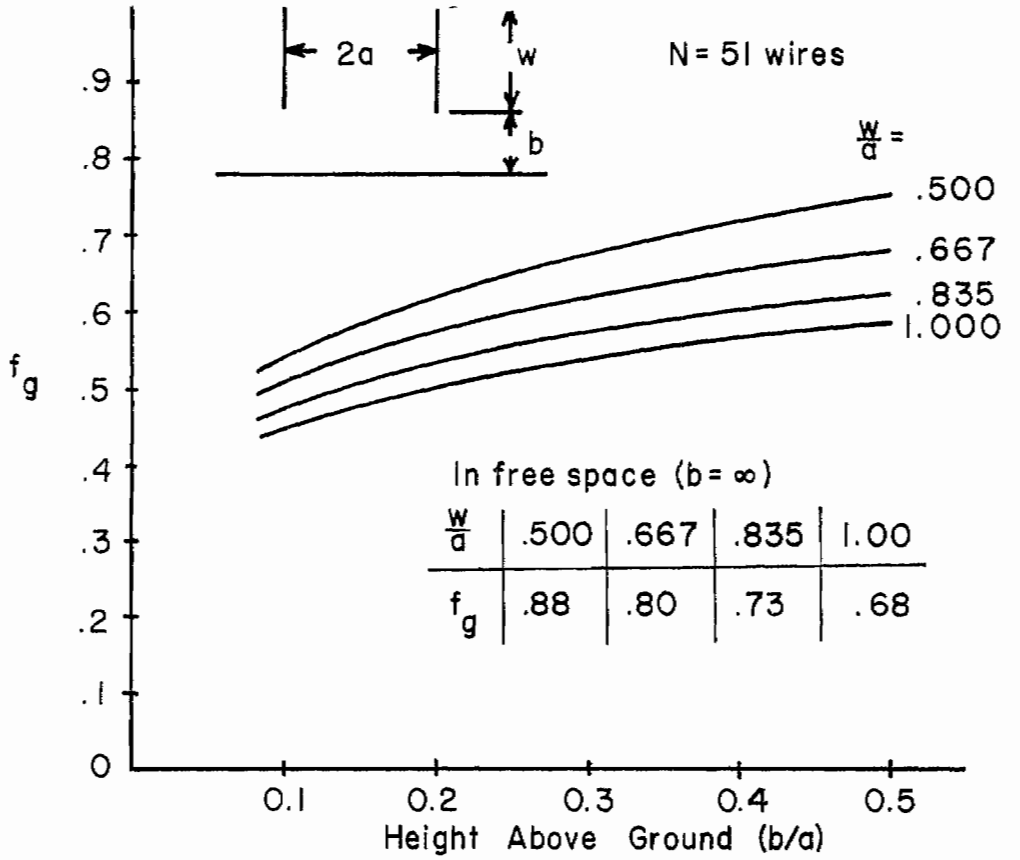

Figure 5.1. Geometrical factor as a function of height above ground with plate width a parameter.

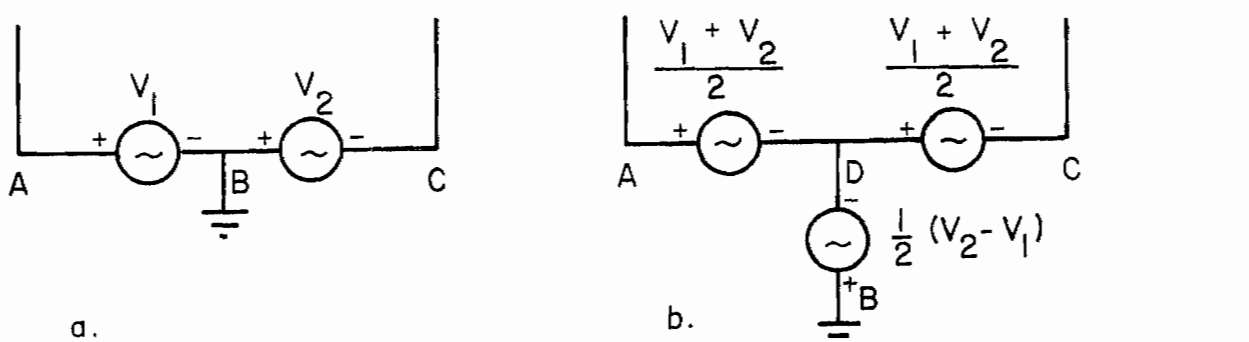

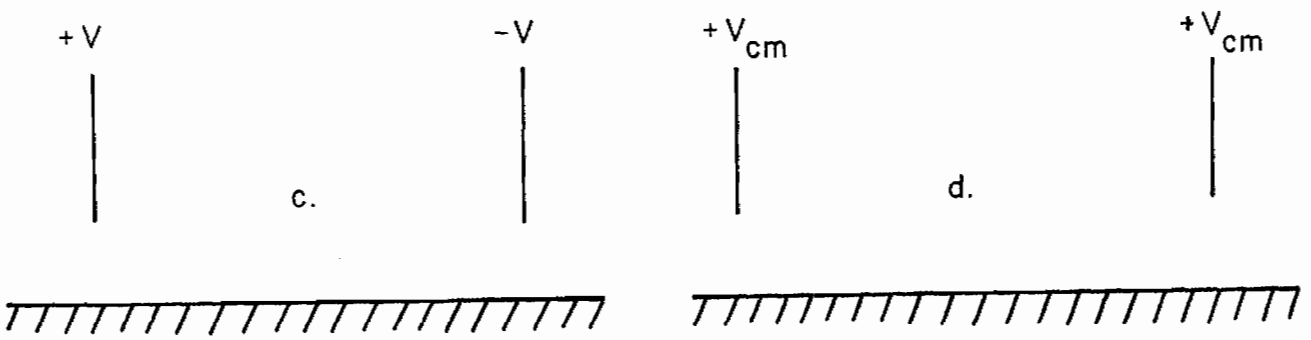

Figure 5.2. Equivalent circuits

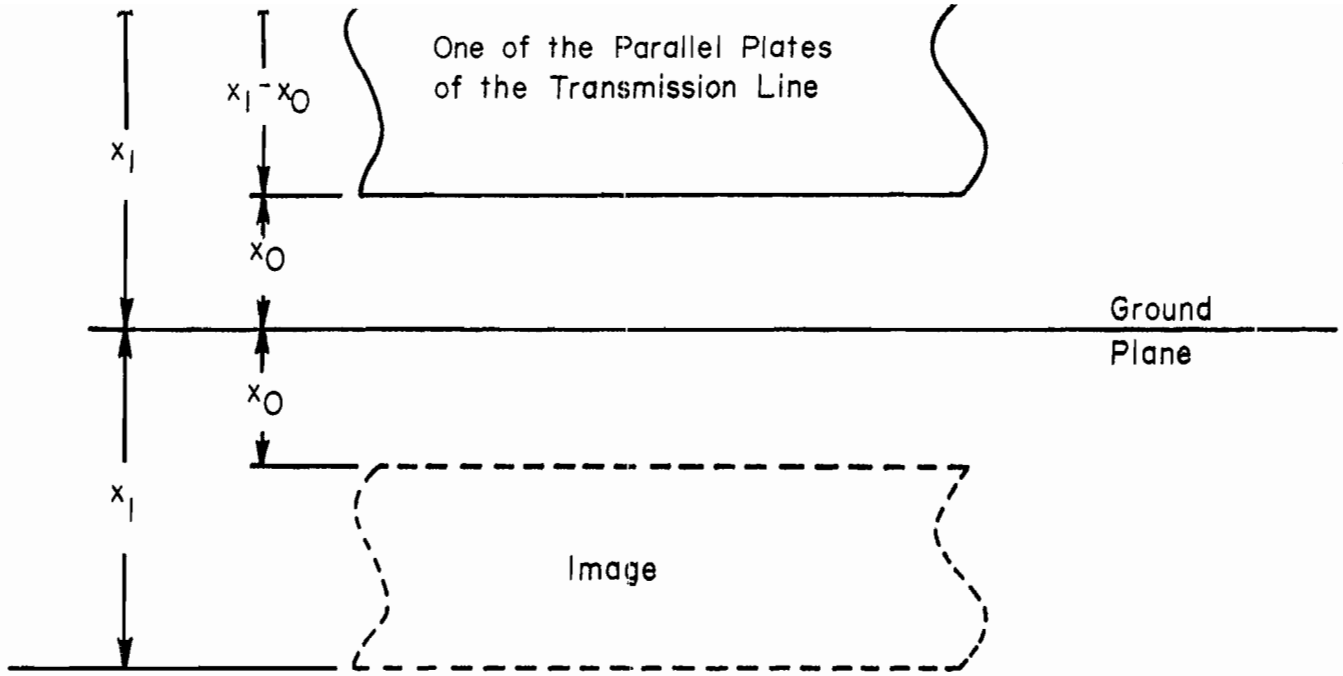

Figure 5.3. Geometry for common mode impedance calculation.

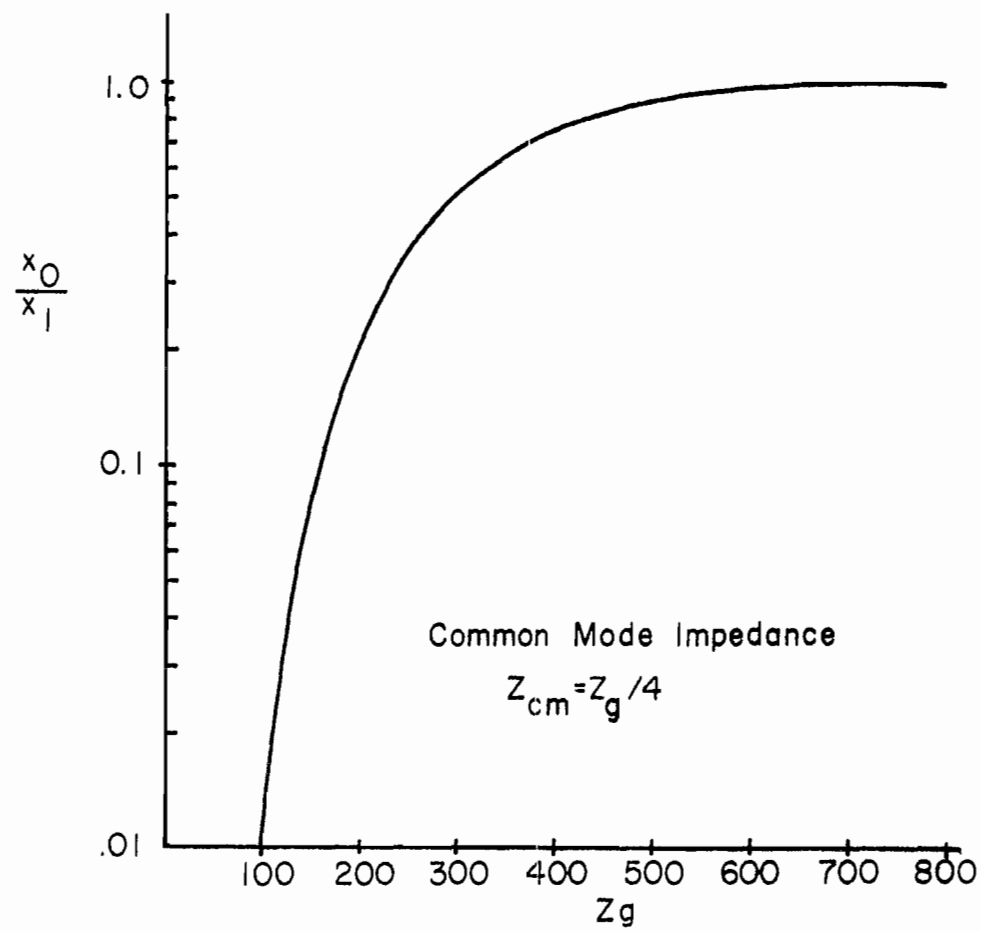

Figure 5.4. Common Mode Impedance.

VI. Impedance Along the Input Transition

We now turn to the impedance questions in the input transition region. This region is taken to extend from the pulse generator location forward to the outer bend in the outer transmission line plates. In design 1, this transition section is a duplex affair, with an enclosed wedge-shaped volume between the two conic-like transition lines. In analyzing the performance of this kind of transition section, we encounter another of the several electromagnetic theory problems posed by this simulator which have yet to be considered in detail in the Sensor and Simulation Notes series. Here, we will simply discuss the problem of TEM mode wave impedance in the transition structure, although this is only one aspect of the overall electromagnetic design problem that has yet to be solved in detail.

Examining the dimensioned drawing of design 1 (figure 1.5), the impedance problems can be visualized. At the pulser locations, the ratio of transmission line width to center plane width is a sufficiently small number that we can start out by considering the two pulser transition sections as electromagnetically independent of each other. Moving along the transition structure from the pulser toward the working volume, the ratio of outer plate width to ground plate width increases and at some point we are no longer justified in ignoring the mutual coupling effects between the two transition sections. Finally, when the two transmission sections join with the main parallel-plate section of the simulator transmission line, we must consider the impedance of this system as a whole. This has already been done in the preceding section.

Obviously, when the outgoing electromagnetic wave has reached the location of the center pole at the end of the wedge-shaped shielded volume between the two transmission lines, its field pattern is going to be quite similar to the field pattern eventually developed in the working volume. This results from the symmetry of the situation, since in the working volume there is no vertical electric field in the central vertical plane which divides the two outer transmission line plates along the centerline of the simulator. Since the central support pole lies in this symmetry plane, it will have practically no effect on the eventual field pattern developed in the working volume, at least from static (or TEM) field considerations. However, moving only a short distance back toward the pulsers from the center pole, this simple symmetry situation no longer exists and the local electric field in the vicinity of the central pair of transmission line plates (the ground plates) will be different in shape from that near the centerline of the working volume. We would expect this distortion of the field pattern to be reflected as a change in the TEM mode characteristic impedance of the transition section

from its value in the immediate vicinity of the center pole. However, there are as yet no convenient analytical results that will enable us to accurately evaluate the size of this impedance discontinuity.

Working back still further toward the pulsers, we eventually encounter a situation in which the spacing between the grounded central transmission line plate and the outer transmission line plate in each transition section is much less than the height above the ground, and so the ground proximity effect can be ignored near the pulsers, in a first approximation. In addition, the center ground plane appears "larger" and thus more closely approximates an infinite ground.

A cross-section of the input transition line at the point where it joins the pulser is shown in figure 6.1. The distance to the ground from the outer plates is so great, relative to the width of those plates, that the presence of the ground can be neglected at this point. Reference 2 can then be used to calculate a series impedance for the two launchers of 312Ω. Alternately we can apply reference 16 by considering each side of the input transition line to consist of two plates of unequal width. This gives an impedance of 326Ω which would be somewhat higher than the true value since the model does not account for the fact that the space between the two center planes has been screened off. The impedance of the input transition line at this point, therefore, appears to lie between 312Ω and 326Ω.

A cross-section at the centerpost has the geometry shown in figure 6.2. To evaluate the impedance at this point, reference 39 (figure 5.1) can be used to yield a result of 273 ohms. One could also ignore the ground effects and use reference 2 to calculate an impedance of 311 ohms. At intermediate points between the pulser and the centerpost, one can estimate the impedance in two different ways: first, by using the distance between the outer plates as the plate separation distance; second, by using twice the outer plate-to-centerplate distance as the plate separation. The first way ignores the effect of the center ground plane wedge and is thus more accurate as one approaches the centerpost where the wedge cross-section is smallest. The second method ignores interaction effects between the two wave launching sections and therefore is most accurate near the pulsers, where the center plate is relatively "large," preventing such interaction. Also, one can calculate the impedance using reference 2, 16, or 39, remembering that references 2 and 16 ignore earth effects while references 2 and 39 don't include the fact that the centerplates have only finite width.

Table 6.1 shows the results of such calculations made for several points along the input transition line. It can be seen that design 1 provides some impedance change along the input

transition. For the region from the pulser to the centerpost, this mismatching can be reduced by sloping the earth upward more rapidly so that in the final geometry there is less ground clearance at the pulser. However, other factors argue toward maximum ground clearance.

If we assume that this impedance variation is fairly smooth and evenly distributed along the length of the transition section, then the net effect of the impedance change will be to introduce a voltage step-down transformer effect. The voltage step-down ratio will be approximately the square root of the output to input impedance ratio, or 0.88. In late times, comparable to the transit time along the transition section (in this case about 260 ns) this step-down effect will disappear and the full pulser voltage will be transmitted to the main simulator transmission section. However, in the vicinity of the rise of the pulse, this effect will reduce the delivered pulse amplitude by about 12 percent. This reduction will persist for a significant fraction of the total pulse length, becoming negligible in the 200 to 300 nanosecond regime after the initial rise of the pulse in the working volume.

This is not a negligible voltage loss. To overcome it directly, one would need to raise the pulser voltage by 12 percent, keeping the pulser capacitance constant since this determines the shape of the low-frequency spectral content in the pulse. This would raise the stored energy requirements by 25 percent, which is surely not negligible.

However, by careful design of the input transition section this transformer effect can be greatly reduced if not totally eliminated. Probably the most straightforward approach would be to widen the outer transition section plates at the pulser location in order to lower the local wave impedance to match that of the main transmission line.

Note that these calculations assume the nominal pulser location indicated in section I of this report. However, the calculated pulser voltage needed for a 200 kV/meter peak field is 35.2 MV as indicated in section IV. If one follows the general guideline of assuming 1 MV/meter average field strength at the pulser, the pulser location is moved to where the input transition is 17.6 meters between plates. The general comments in this section still hold, however, and since present considerations indicate that a sloped pulser array will be used the question of pulser location is not precise anyway.

Distance from Apex (m)	d	b	2a	Z (ref 2)	Z (ref 16)	Z (ref 39)
25	30	12.5	7.5	312	326	---
50	31.7	27.6	16.7	311	336	306
75	32.6	41.4	25.0	311	354	292
100	33.3	55.2	33.3	311	362	273
125	30	62.5	40.0	305	392	256
	d	b + Δ	2a	Z (ref 2)	Z (ref 16)	Z (ref 39)
50	31.7	37.6	16.7	348	---	313
75	32.6	46.1	25.0	324	---	302
100	33.3	55.2	33.0	311	---	273
125	30	62.5	40	305	---	256

d = distance from nominal ground to bottom edge of plates

b = 1/2 the plate spacing (outer plate to center wedge)

2a = width of the plate

b + Δ = outer plate to simulator centerline

Z = series impedance of the two wave launchers at point being considered

Table 6.1

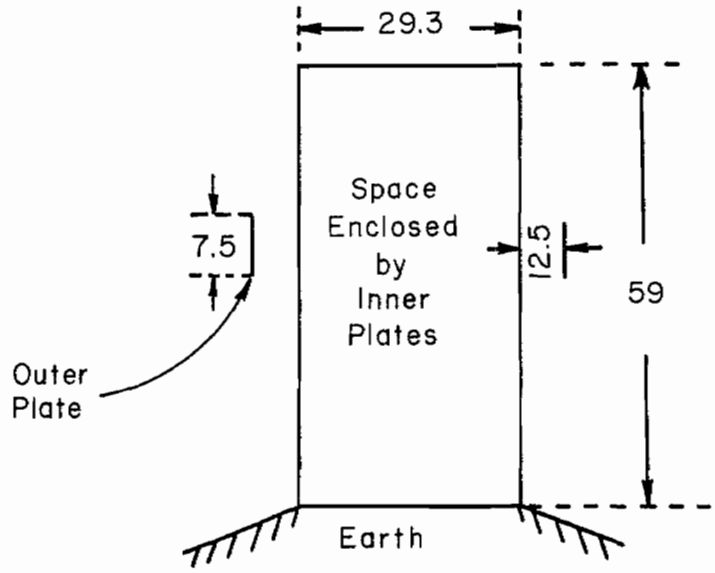

Figure 6.1. Cross section of transmission line at nominal pulser location.

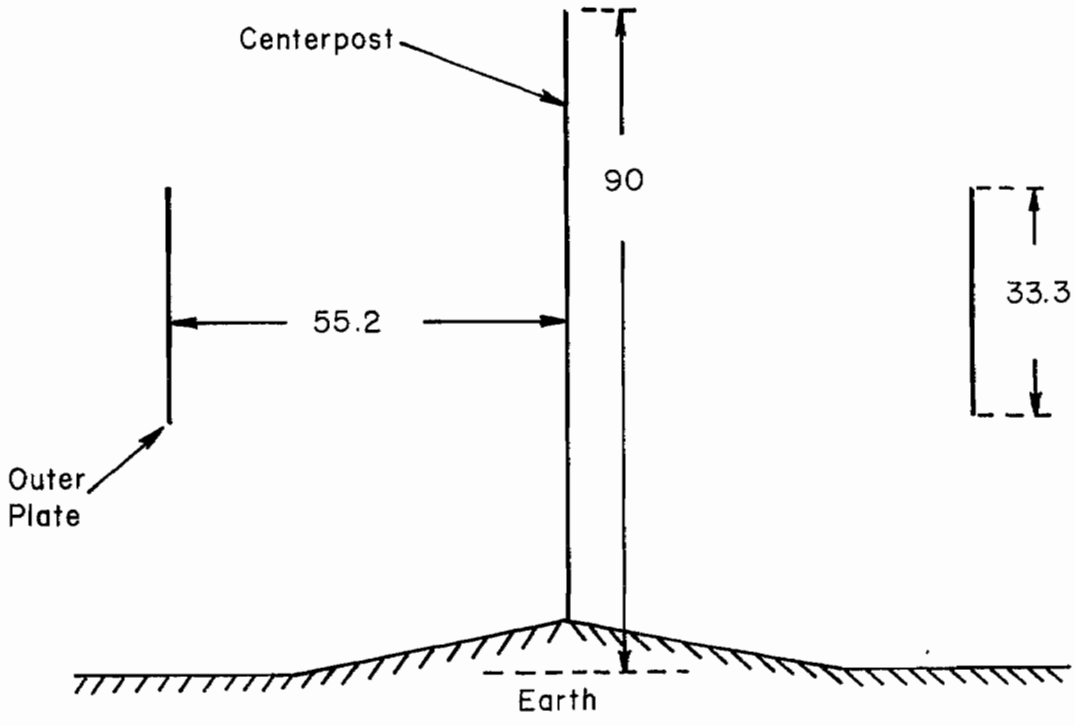

Figure 6.2. Cross section of transmission line at centerpost.

VII. Planarity of Incident Wave at the Input of the Cylindrical Transmission Line

In design of a simulator of the present type in which various design compromises are made it is usually impossible to exactly calculate the complete pulse response of the system. Instead various frequency or time components of the pulse must be considered separately. The frequency components in the incident pulse spectrum which have wavelengths much less than the transverse dimensions of the transmission line structure will propagate according to the laws of geometrical optics. Two useful simulator design concepts that arise from the application of these laws are the idea of wave front planarity and the concept of wave reflection (constructive interference) zones. These ideas are discussed in some detail as they apply to the design of EMP simulator systems in several of the Sensor and Simulation Notes. Reference 4 contains much useful information on the application of geometrical optics to design of this type of a simulator.

The concept of wave front planarity can be visualized, for the design 1 system, with the aid of figure 7.1. We will calculate the planarity of the wave as it arrives at the principal transverse diameter of the working volume, defined by diameter AB. If the incident wave were perfectly plane then the wave front would arrive simultaneously at every point on line AB. However, it is clear from figure 7.1 that the wave will arrive first at point C, which is located nearest to the apex of pulser Number 1. Of course, since both pulse sources are presumed to fire simultaneously, then all statements about wave arrival above the centerline of figure 7.1 apply equally to the mirror image points below the centerline. Also, the last point on diameter AB to receive the wave front signal will be the center point of the diameter. (In actuality, points A and O receive the signal at the same time.)

The wave planarity is simply defined as the time difference between the earliest and latest arrival times of the wave on diameter AB. Applying the dimensions of design 1 to figure 7.1, we find that this difference in arrival times is 3.8 nanoseconds.

The geometry for calculating such planarity times is shown in figure 7.2. The difference in arrival time between point A and point B of a spherical wave centered at point O is given by the expression

$$\Delta t = \frac{R_o}{c}\left[\sqrt{1 + (d/R_o)^2} - 1\right] \approx \frac{d^2}{2R_o c} \quad \text{for } \left(\frac{d}{R_o}\right)^2 << 1$$

Using this expression one can also calculate the planarity across the junction of wave launching section and the parallel plate section (along the line $\overline{PP'}$ of figure 7.1). The maximum time difference can be shown to be approximately 13.6 nanoseconds. This planarity number can be considered as one measure of how well the conic input sections are matched to the parallel plate section of the transmission line. (See reference 4.)

One way of approximating the impact of this planarity number on the quality of the simulation obtained is to imagine a picture of the arriving signal built up by adding the outputs of a large number of E field sensors located along diameter AB. If the incident spherical wave front is supplied by a perfect step-function source (zero rise time) the composite output signal will have a rise time from zero to peak simply equal to the planarity time as calculated above. So, one sensible approximation to make here would be that the incident wave is "equivalent" to a perfectly planar wave incident on diameter AB but with a finite rise time equal to the planarity time. In practice, the pulse source will itself have a finite output rise time and this may be combined in a rough manner with the planarity time by taking the square root of the sum of the squares of the two times to arrive at an overall equivalent pulse rise time. Thus, if the pulse source in this case produces an intrinsic rise time of 10 nanoseconds, the "equivalent" rise time in the working volume would be 10.7 nanoseconds by this argument. Note, however, that the square root of the sum of the squares may not be a very accurate combination.

The above approximation is useful for simulators having only a single input transition section driven by a single pulse generator. However, things are somewhat more complicated in the case of ATLAS I. The added difficulty arises from the fact that point C in figure 7.1 only receives a direct signal from pulser No. 1 but the center point of diameter AB (point O) receives an equal signal from both pulsers No. 1 and No. 2, and these signals simply add vectorially for a time, producing a net electric field at this central point which is almost twice as large as that received at point C. The final static field value will tend to lie between the two.

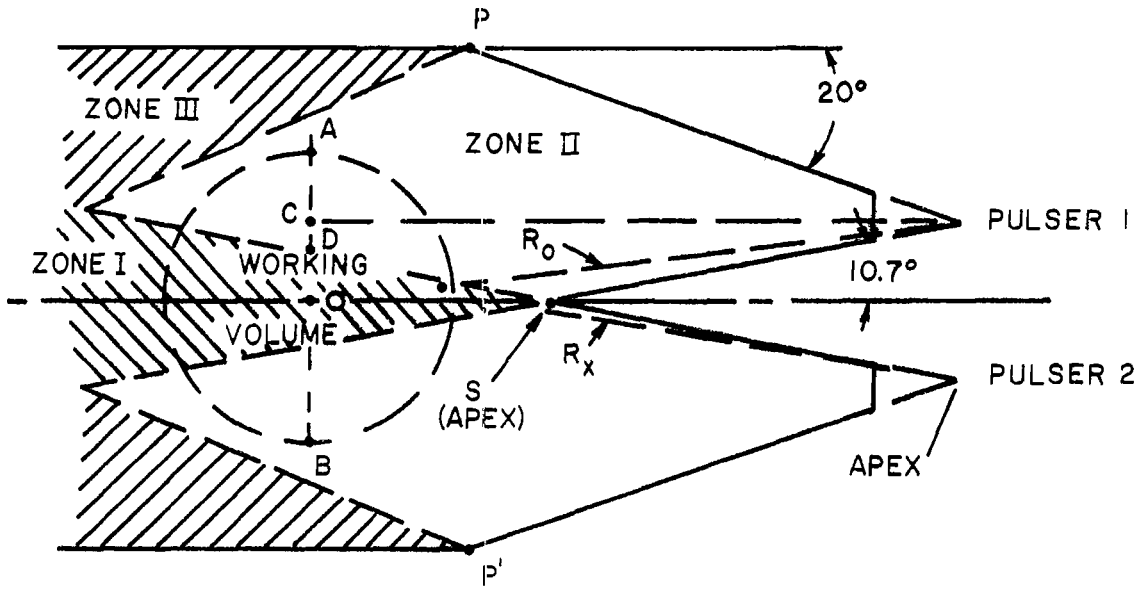

Figure 7.1. Diffraction and reflection zones.

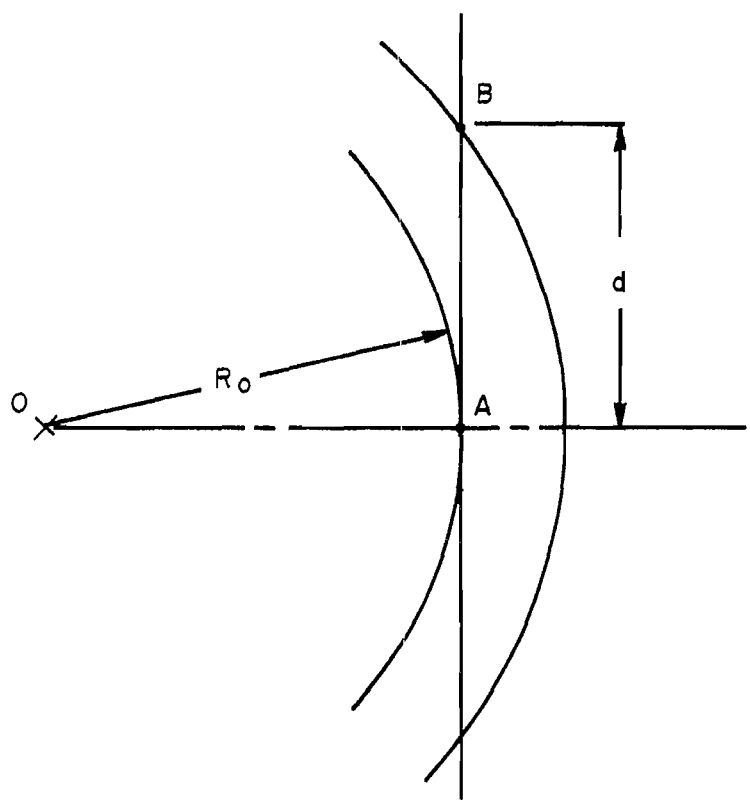

Figure 7.2. Geometry for planarity calculations.

VIII. Reflection and Diffraction at the Input Section

Introduction

Even if one matches impedance between the conical wave launching sections and parallel plate section of simulator, a number of reflection and diffraction effects will occur associated with the junction of these two sections. Several Sensor and Simulation Notes (references 4, 5, 7, 25) have addressed this general class of problems, but specific problems of the dual conical wave launchers proposed for design 1 have not been addressed in detail. Certain, somewhat crude, models will be studied here to at least identify the major effects of the various reflection and diffraction phenomena.

The input transition section can be divided into certain reflection and diffraction zones as shown in figure 8.1. Zone I "sees" direct illumination from both pulsers as well as the effects of diffraction at the center ground plane apex, point S. Zone II is illuminated by only one of the pulsers and is outside the direct reflection regions defined by geometrical optics. Zone III is the region where direct reflection from the side plates is seen. Diffraction effects at points P and S perturb the fields in all of these zones and the varying arrival times of all these combined effects make detailed calculations of field strengths at various points rather difficult.

Reflection and Diffraction from the Side Plates

Let us first consider the reflection and diffraction caused by the bend in the outer plate at point P as shown in figure 8.1. The technique used is to directly apply the theory developed in reference 7 for the diffraction at a bend in perfectly conducting plate. This theory does not consider the 1/r fall off of the incident fields or the finite extent of the conducting plates, and thus the results can only be considered approximate. However, approximate corrections can be made to include these effects.

A line drawn from the intersection of the input transition plate with the cylindrical transmission line plate and tangent to the edge of the circular working volume makes an angle of 27.6° with the transmission line plate. From reference 7, figure 5, one sees that

$$1 \leq |\vec{H}_o| \leq 1.25|\vec{H}| \tag{8.1}$$

$$0.8|E_y| \leq |E_{oy}| \leq 1.2|E_y| \tag{8.2}$$

and

$$|E_{ox}| \leq 0.2|E_y| \tag{8.3}$$

where the geometry is as shown in figure 8.2 and E_y and H are the strength of the fields incident at the bend (assumed a step-function in reference 7).

Figure 5 of reference 7 is reproduced here as figure 8.3. Since the values of E_{oy} and E_{ox} vary differently in time one cannot add them vectorially directly and put the result in the x',y' coordinate system. If one assumed the peaks to occur at the same time, one gets the maximum E in the y' direction of 1.2 E_y and a minimum of 0.82 E_y while the E in the x' direction ends up 0.09 E_y due to the opposite directions of the two x' components of E_{ox} and E_{oy}.

For a square working volume as seen from the top, 75.7 meters on a side, the angle from the bend to the back corner becomes 18.3° and again using figure 8.3 one gets

$$1 \leq |\vec{H}_o| \leq 1.5|\vec{H}| \tag{8.4}$$

$$0.8|E_y| \leq |E_{oy}| \leq 1.4|E_y| \tag{8.5}$$

and

$$|E_{ox}| \leq 0.3|E_y| \tag{8.6}$$

Again the time variations are different but if they are assumed to be the same one gets

$$.83|E_y| \leq |E_{oy'}| \leq 1.42|E_y| \tag{8.7}$$

$$|E_{ox'}| \leq .2|E_y| \tag{8.8}$$

again due to the cancellation of components. $E_{ox'}$ is now in the plus x' direction due to the x' component of E_y being larger in this case. The positive x' component of E_y more than compensates for E_{ox} being in the minus x direction. Here $E_{oy'}$ is the field in the y' direction and $E_{ox'}$ is in the x' direction.

Several comments should be made regarding the use of the graphs reproduced in figure 8.3. The data were calculated for a bend angle ϕ_o of $.1\pi$ radians or 18°, which varies slightly from the 20° bend of design 1. The calculation at the edge of the circular working volume uses the $\phi/\pi = .2$ curve while that calculation for the square working volume uses the $\phi/\pi = .25$ curve. Only the outer edge of the working volume was considered because the effects of diffraction rapidly become smaller as one moves into the working volume and away from the direct reflection zone (Zone III of figure 8.1).

One should also note the time scale of the graphs and compare the risetimes shown with the real rise time of the incident pulse being diffracted (figure 8.3 data assume a step-function incident pulse). From reference 7, τ is a normalized time and

$$\Delta\tau = \frac{c\Delta t}{r} \tag{8.9}$$

where c is the speed of light, Δt is the real time interval and r is the distance from the bend in the plates to the point of observation. Referring to figure 8.2 the distance $r = \overline{PQ} \simeq 63$ meters. Thus

$$\Delta t = \frac{r\Delta\tau}{c} \simeq (210 \text{ nsec}) \ (\Delta\tau) \tag{8.10}$$

Since the pulser initial rise to some fraction of the peak is expected to be about 10 ns, one would expect some small effect on the step risetimes indicated for $\phi/\pi = .2$, but from the above calculation it is seen that the general shape of the pulse is only slightly affected since the pulse width is much greater than 10 ns.

Thus one can conclude from the results of the somewhat crude theory applied here that diffraction from the side plates will only slightly perturb fields in the working volume.

It should also be noted that no 1/r correction was included in the above discussion, indicating that we really have a worst case analysis. In reality, fields diffracted from the bend in the side plate have about a 10% longer path to the edge of the working volume than the directly illuminating fields. Thus one would expect the diffracted fields to have roughly 10% less effect than indicated above when compared to the direct path fields. However the fields which first arrive at the observation position are associated with a different position on the TEM mode than those which diffract from the first bend in

the outer plate(s). One can note from figure 13 of reference 2 that the field incident on the bend is perhaps 50% larger than that propagating directly toward the observer; this would increase the diffracted field by about this amount. Finally the 1/r correction for the amplitude reduction of the fields from the conical launcher into the transmission line will reduce both direct and diffracted fields at the observer (Q) by about 40% for the direct fields and an additional 10% (as above) for the diffracted fields. These various effects tend to cancel each other out in minimizing overshoot and giving a smooth waveform.

Reflection and Diffraction Associated with the Junction of the Central Ground Planes

The pulse propagating in the simulator transmission line has a very broad frequency spectrum, containing components with wavelengths as short as a few meters to dimensions larger than the simulator itself. The short wavelengths propagate according to the laws of geometrical optics for the most part, but the longer-wavelength components in the pulse produce very complex wave diffraction effects at discontinuities in the transmission line geometry such as bends, folds, etc. These diffraction phenomena are not very amenable to straightforward analysis, but in general require several approximations to be made in the solutions of Maxwell's equations. Several useful results have been published in the Sensor and Simulation Note Series, most notably those of Note 47 (reference 7) and Note 128 (reference 25). Of these, we will refer most frequently to reference 7 in this section, since it deals primarily with "interior" bends in transmission lines and the principal diffraction problems are all associated with such bends. Reference 26 lays the ground work for further diffraction calculations involving other shapes than sheets, but it contains no results of immediate use to the design engineer and will not be utilized here.

Although the results of references 7 and 25 are extremely useful, they must be applied with care in the case of interest here. These results apply strictly only to the idealized case of a uniform TEM plane wave diffracted at a bend in an infinitely wide conducting sheet. In reality, these approximations fail in many cases since the wave carried in the transition section is neither uniform nor plane but is ideally spherical and has a field distribution across a surface of constant phase much like that described in the static field plots of references 2, 8, 30 and 39. Secondly, the plates are definitely limited in width, and most points inside the working volume are located sufficiently far from these plates that the effects of finite plate width will influence the diffraction signal.

The data in reference 7 will be used keeping these cautionary notes in mind. However, first let us consider another approach to the diffraction problem.

Turning now to figure 8.4, the wave diffraction problem can be described in terms of the sequence of events that occur at a point P_o inside the working volume as the incident wave passes this location. The first signal to arrive at P_o travels along radius R_o, the straight line connecting P_o with the apex of the pulser array. This apex is the focal point of the virtual point source which the pulser represents as it launches its quasi-spherical wave into the transition section. The amplitude of the signal at P_o during this early-time regime is determined by whether P_o is located inside Zone I (figure 8.1) or in Zone II of that figure. If it is in Zone I, we have seen in section VII that the amplitude at P_o will be practically twice the amplitude delivered by each pulser alone, since the signal is delivered to this point by both pulsers almost simultaneously. The signal amplitude remains at this early-time value until additional information about the boundary conditions in the transition region can reach point P_o. The first such new information arrives along paths R_2 and R_1, and at this time the electric field at P_o begins its transition from the early-time to its eventual "static" or late-time value.

Up to this point, the sequence of events is identical to that described in reference 7. However, in this case the plate width of the conducting sheet which is providing the "new" information about the boundary conditions is finite, and we can expect the flow of this "new" information to stop when the signal has arrived at point P_o from the edges of this plate. This edge signal propagates along paths R_3 and R_4, and when it finally reaches the observer at P_o, we can for all practical purposes assume that the diffraction contribution of the center plates as considered above is ended. The electric field at P_o will rest at the value it has reached, until more "new" information can arrive from the outer bends in the transition section. Then, relaxation toward the final "static" field value will resume.

We cannot deduce the shape of the diffraction pulse from this argument, but these shapes are given in the data of reference 7. This reference will apply for time intervals at point P_o up to the arrival time of the "edge" signal contribution. At this time, the pulse shape will diverge from that given in reference 7, since the reference is based on an infinite plate width and no final "edge" signal is ever observed.

There is another slight difference between this situation and that of reference 7, in that the secondary waves traveling along paths R_1 and R_2 are spherical rather than planar and will thus be slightly lower in amplitude than the principal wave

propagating along the shorter path R_o. In reference 7, all the incident energy is carried in a uniform plane wave, and this additional inverse distance attenuation factor is not present to reduce the amplitude of the diffracted waves with respect to the principal wave. However, this slight difference will be neglected for the moment.

To illustrate these concepts by an example, take point P_o as the geometrical center of the working volume. Then signal contributions arrive at this point simultaneously from the two pulsers and its initial field value is twice that from one pulser alone.

The relationship between the early-time field arriving at P_o from each pulser and the "static" late-time field is a complicated issue which is not fully understood. The early-time field at P_o depends greatly on the early-time field distribution launched by the pulser array. Now, the pulser array is being designed so as to approximate a TEM mode field distribution as closely as is economically feasible (see references 37 and 38). Even assuming that the pulser array launches a perfect TEM mode wave at the pulser location another problem occurs. As noted in section VI, the waves launched by the two pulser arrays are largely isolated by the large center ground plane at the pulser location. At the apex of the ground plane wedge, however, the two waves "see" each other and are expected to approximate a TEM mode field distribution. Since the center ground plane wedge has both finite height and width at the pulser location, the TEM mode field distributions at the pulser location and at the apex of the center wedge are different, resulting in the impedance variations noted in section VI.

Noting these difficulties, let us make the assumption that the pulser arrays and transition sections are designed so that a TEM field distribution exists across the wavefront of the launched pulse at the ground plane apex (along SP' of figure 8.1). Further assume that this is the TEM distribution for a finite width parallel plate line of plate separation $2\overline{SP}'$, ignoring the effects of the earth below the line (the early-time wavefront does not "see" the ground effects). Also assume a step-function incident wave.

With these assumptions it can be seen that the early-time field value at P_o is approximately given by

$$E_{initial} \simeq 2 \cdot \left(\frac{62.5m}{\overline{SP}'}\right)\left(\frac{R_2}{R_o}\right)E_{late\ time} \qquad (8.11)$$

where the factor 2 accounts for the two sources, the ratio $(62.5/\overline{SP}')$ shows the effect of the transmission line's cross-

sectional spacing being larger across the working volume than across the line at the apex of the ground plane, and the ratio (R_2/R_o) gives the approximate proper 1/r fall-off for a spherical wave. Elate time is the field one would see at P_o for a quasi-static TEM field distribution when the effect of the earth is not included.

For design 1, with P_o at the center of the working volume,

$$R_o = 159 \text{ m}$$

$$R_1 = 57.8 \text{ m}$$

$$R_2 = 101.8 \text{ m}$$

$$\overline{SP'} = 55.2 \text{ m}$$

giving

$$E_{initial}(P_o) \simeq 1.41\, E_{late\ time} \qquad (8.12)$$

The signal at point P_o will remain at this initial value for a time corresponding to the difference between R_1 plus R_2, and R_o, or 0.6 meters, which translates to 2.0 nanoseconds. At this time, as shown in figure 8.5, the amplitude will begin to relax toward its eventual steady-state value. This trend will continue until a signal can arrive along path lengths R_3 and R_4. Once again, figures 1.5 and 8.4 show that these lengths are 110 and 70 meters, respectively. So the "edge" reflection arrives 63 ns after the onset of the signal at point P_o.

To sketch in the waveform up to this time, reference 7 can be used up to 63 nanoseconds, the diffraction behavior will be the same as that of an infinitely wide plate.

To facilitate the use of reference 7, observe that the centerline of the simulator as shown in figure 8.1 is in fact a plane of symmetry, with all components of electric field parallel to that plane being forced to zero for all times. This results from the symmetrical construction of the simulator array and the assumed simultaneous firing of the two pulse generators. Consequently, this central plane can be replaced by a conducting sheet, and the problem of diffraction at the centerpost where the two transition ground plates join then becomes equivalent to the diffraction problem at an "interior" bend which is discussed in reference 7. The angle of this bend, ϕ_o (referring to figure 2 of reference 7) is then 10.7° as shown in figure 8.1.

For an observation point on the central plane of the simulator, the observer angle ϕ is equal to the bend angle ϕ_o and both of these are equal to 0.188 radians, or $\phi/\pi = 0.06$. The diffraction pulse data that most closely corresponds to this angle is that of figure 4 of reference 7 given for ϕ/π of 0.05. In that figure, the item of interest is the data for e_y. In the present case, r, the distance from the bend in the sheet to the observer, is equal to our value of R_1, or 57.8 meters. Using equation 25 of the reference, we find that the normalized time corresponding to a time t of 63 nanoseconds is 0.33. The normalized time τ is equal to the time t at the observer's position multiplied by the speed of light and divided by the radial distance R_1 between the bend (centerpost) and the observer. From figure 4 of the reference, the diffracted pulse has fallen to a value of 1.08 at this time τ, and this is shown in figure 8.5.

It should be noted that during this time interval the wave shape should be very similar to those of reference 7. As indicated in reference 25, for early times the diffracted field will vary as $t^{1/2}$ and figure 8.5 reflects this variation.

The earliest information that can arrive at P_o from the outer plate bend, from the geometry of figure 8.4, begins to show up at 143 nanoseconds after the start of the pulse at P_o. At this time, the electric field continues to decline toward its late-time value, which it reaches for all practical purposes when the signal from the upper edge of the outer plate bend finally arrives at point P_o. The resulting electric field pulse is shown in figure 8.5.

To complete the waveform, we now must consider the effect of the earth on the field and when this effect is first seen. By comparing references 2 and 39, it can be seen that a perfectly conducting earth below the line tends to decrease the fields between the plates. Thus, the late time field with the earth is related to the field without the earth by the ratio $E_{\text{with earth}}/E_{\text{without earth}}$.

Along the symmetry plane of the simulator, this ratio is equal to the ratio of efficiency factors, f_E (defined in equation 4.4. Also see references 2 and 39) neglecting any transient voltage or current change on the transmission line due to the small change in impedance. For the case of design 1, f_E ignoring the earth is about .810 (reference 2) and f_E with the earth is .619 (reference 39), giving a ratio of 0.764. This result is shown in figure 8.5. However, the effect of the earth can be seen in the working volume only when a reflection from the earth has had time to reach the point of interest. Assuming a flat earth and the dimensions of figure 1.5, the first ground reflection arrives at approximately 65 nanoseconds. Note that a step-function input signal has been assumed and

that for times of several hundred nanoseconds, the RC decay time of the capacitive source would cause the waveforms to fall off faster than indicated in figure 8.5. Constructions very similar to this one can be performed for any point lying inside Zone I of figure 8.1.

The diffraction situation at the outer edge of the working volume, point A of figure 8.1, is somewhat different since that point lies in Zone II and so receives direct radiation only from pulser No. 1. In that case, the initial electric field to arrive at point A is given by

$$E_{initial} \simeq \left(\frac{62.5m}{\overline{SP'}}\right)\frac{R_o(A)}{R_2} E_{late\ time} \simeq .7\ E_{late\ time} \quad (8.13)$$

Here, $E_{late\ time}$ is the static or late-time value of the electric field at point A, neglecting earth effects, and $R_o(A)$ is the distance from the pulser apex to point A.

From the above equation and the stated dimensions, we can see that the early-time E field at point A is only 70 percent of the eventual late-time field value, assuming an ideal step function pulser waveform and neglecting earth effects. So the diffraction effects in Zone II are quite different than those in Zone I. In Zone II, the electric field pulse initially undershoots its final value, while in Zone I a definite overshoot phenomenon is observed.

The geometrical delay time arguments advanced earlier can be used here in a similar way to construct the composite waveform at point A. First, the amplitude will remain stationary at its early-time value until signals can reach point A from either the inner or outer bends in the transmission line plates. From figure 8.1 it is clear that point A is nearer the outer bend than it is to the centerpost of the transition section, and in fact signal will begin arriving at this point approximately 45 ns after the principal wave arrives. The final information regarding the boundary conditions at the interface between the "transition" section and the parallel-plate section arrives at point A from the top of the center pole at approximately 100 ns after the beginning of the pulse at point A. This marks the time at which the field at A assumes its late-time or static value for all practical purposes. The resulting waveform, for the transverse E field component, is sketched in figure 8.5. There will be a longitudinal E field component at point A as well, since this point is not located on the central symmetry plane of the simulator, and the wave shape at this point can be constructed from the data of reference 7. To do this, it is necessary to superpose the results of two sets of data, one corresponding to the longitudinal diffraction signal

from the outer bend of the transmission line and the other to the signal from the inner bend.

As mentioned when considering the waveform at point O, the effect of the earth on the waveform at point A must be taken into account at late times. The same ratio of efficiency factors used previously applies to point A, but one must multiply this ratio by the ratio of normalized fields at A with and without the earth below. The net result is that when one considers earth effects the late-time field at point A is about 0.85 the field with no earth effects, as indicated in figure 8.5.

The above described geometrical approximations, combined with the data of reference 7, can be used to construct pulse waveforms for virtually any point inside the simulator transmission line. The two working volume waveforms sketched in figure 8.5 are representative of the range of pulse shape differences caused by diffraction effects across the transmission line.

One can also use the same techniques to study variations in the waveform as one goes from the front to the rear of the working volume. The early-time peaks of the waveforms at several locations along the centerline of working volume are plotted in figure 8.6. Note the changes in pulse shape from one end of the working volume to the other. The height of the early-time peak tends to decrease as one approaches the rear of the working volume, but the width of the peak increases.

Thus, one can readily see that the pulse shape varies somewhat at early times over the working volume. This effect is almost impossible to avoid with such a large working volume and limited length for the input transitions. All of these deviations are not necessarily harmful however, since the "overshoot" in Zone I tends to reduce the equivalent pulse risetime averaged over the diameter of the working volume. The importance of understanding these various effects is to enable the user to properly assess the response of the test object.

One should remember that the diffraction and reflection phenomena associated with the central ground planes are rather complicated and the results presented here are only approximate. The time history of the pulse at various points in the working volume is a function of many things including field distribution at the pulser array and pulser risetime. Further study is needed in many areas, and the waveforms shown in figure 8.5 should be considered as general estimates rather than exact specifications.

Also, one should be careful to note several important factors concerning the waveforms shown in figure 8.5. First of

all, a step-function risetime was assumed. In actuality, a finite risetime would tend to round off the initial peak seen at the center of the working volume. (The amount of round off will be considered later.) The second point to remember is that each waveform is normalized to the late-time (TEM mode) electric field at that point (ignoring ground effects), and that the late-time fields are considerably different at different points in the working volume. (See section IV.) However, the late-time field variations are opposite the early-time variations. At late-times, the field at point A is 1.5 times that at point O (see figures 4.3 and 8.1) while for early-times the field strength at point A is about one half times 1.5 or .75 times that at point O. These two effects will tend to cancel each other, giving a composite uniformity better than that indicated in section IV.

Thus far, we have just considered a step-function rise on the incident field. We will now consider the effect of a finite risetime on the waveform in the working volume. First, let us approximate the waveform of Zone I (figure 8.1) as

$$R(t) = 1 + e^{-t/T_1} \tag{8.14}$$

Thus we are approximating the diffraction effects by an exponential decay, and R(t) is normalized to the field of one pulser array by itself (i.e., the field from just one pulser at the point in question would be unity). Examination of reference 7 indicates that T_1 is in the range of 20 to 30 nanoseconds. Now, assume the input pulse has the form

$$E_{in}(t) = 1 - e^{-t/T_o} \tag{8.15}$$

where we have assumed that the RC decay time of the pulse is considerably longer than other times being considered. Upon differentiating E_{in} to obtain the "impulse response" and convoluting the result with R(t), the output response can be evaluated in closed form as

$$E_{out}(t) = 1 - (1-k)e^{-t/T_o} - k\, e^{(-t/T_o)\left(\frac{1+k}{k}\right)} \tag{8.16}$$

where

$$k \equiv \left(\frac{T_1}{T_o - T_1}\right)$$

This function reaches a peak at time t_{pk}, given by

$$t_{pk} = -kT_o \ell n\left(\frac{k-1}{k+1}\right) \tag{8.17}$$

Amplitude at peak is given by

$$E_{out}(\text{peak}) = 1 + (k-1)\left(\frac{k-1}{k+1}\right)^k - k\left(\frac{k-1}{k+1}\right)^{k+1} \tag{8.18}$$

Figures 8.7 and 8.8 show the resulting output pulses for the indicated T_o and T_1 values. The peak time T_{pk} and peak amplitude E_{pk} are also tabulated. The time at which the pulse overshoot falls to 10 percent of the late-time amplitude is given as T (10 percent).

Curve Number	T_o	T_1	T_{pk}	E_{pk}	T (10 Percent)
1	10	20	22	1.333	58
2	20	20	40	1.135	60
3	30	20	66	1.037	-
4	4.5	30	13	1.642	74
5	10	30	24	1.447	82
6	20	30	42	1.250	92
7	30	30	60	1.135	90

(times in ns)

Applying these results directly to the waveforms in figure 8.5 is somewhat difficult but the above considerations point out the main effects of an assumed finite risetime on the waveform in the working volume. Of course, the TEM waveform launched by a pulser array does not necessarily have a simple rise characteristic (reference 38) and so the risetime effects considered here are only illustrative.

Now, let us consider a completely different way of looking at the centerpost diffraction problem. This method directly applies the results of reference 7 and includes approximations treating the 1/r field fall-off and pulser risetime effects. This method primarily gives us an estimate of relative fields at various points in the working volume for early times, while not attempting to relate the early and late-time fields. This is in part a recap of some of the earlier considerations.

Reference 7 analyzes the diffraction of a step-function plane wave by a bend in a perfectly conducting plane. By symmetry arguments it can be shown that this analysis is also applicable to the intersection of two guided plane waves. The incident wave of reference 7 corresponds to the plane wave from one source and the reflected wave corresponds to the plane wave from the other source. However, the case of interest in design 1 of ATLAS I is the intersection of two guided waves which have approximately spherical fronts.

Since spherical waves have a 1/r fall-off from the assumed point sources the incident wave can easily be treated. However, the problem is how the reflected and diffracted waves computed in reference 7 can be corrected for 1/r fall-off.

There are two regions of concern in which different effects are taking place. The first region is $\phi_o \leq \phi \leq 2\phi_o$. Refer to figure 8.9. This is the region corresponding to those parts of the simulator with a direct line of sight to both point sources. In this region reference 7 shows the incident and reflected waves superpose to form a high, short-lived peak amplitude. The peak is followed by a decay to a value closer to that of the incident field. See figure 8.3. This decay can be described as a diffraction effect.

The second region is $2\phi_o \leq \phi \leq \pi$ and will be termed the shadow region. This region corresponds to those parts of the simulator where there is a direct line of sight to only one point source. In this region reference 7 shows only a diffraction wave.

In order to make the 1/r correction two assumptions will be made.

1. The field fall-off with r is continuous in a direction parallel to the wave front. Therefore, since the field in the superposition region falls off approximately with 1/r, the field in the shadow region will be assumed to fall-off with 1/r. This is consistent with the coupling of energy from the diffraction wave region behind the peak of the wave in the superposition region in the shadow region.

2. The peak of the diffraction field for the spherical incident wave has the same variation with ϕ as the diffraction field for the plane incident wave calculated in reference 7. This is consistent with the first assumption.

Obviously both of these assumptions are better for small values of ϕ_o and for small values of ϕ since for larger angles the difference between the direct distance R and the indirect (reflected or diffracted) distance $R_o + R'$ becomes greater (see figure 8.9).

The configuration for this computation is shown in figure 8.10. Eighteen points are shown where calculations are made. The actual value of ϕ_o for design 1 is 10.7°. However, since the cases of ϕ = 9°, 18° and 27° are computed in reference 7 it will be assumed that ϕ_o = 9° to avoid interpolation. In addition, the case of ϕ = 36° will be estimated.

The principal component of the horizontal electric field is the y' component of the e_{oy} function given in reference 7. However, the relationship between the incident, and the reflected or diffracted waves is different for the spherical wave. By subtracting 1.0 from the e_{oy} the reflected or diffracted wave can be obtained or

$$e_{ydiff} = e_{oy} - 1.0 \tag{8.19}$$

The y' component of the e_{oy} component of the reflected or diffracted wave is

$$e_{y'diff} = (e_{oy} - 1.0) \cos\phi_o \tag{8.20}$$

The incident part (1.0) can be corrected for the changed angle of incidence by taking the y' component directly as

$$e_{y'inc} = \cos(\alpha - \phi_o) \tag{8.21}$$

The y' component of the e_{ox} component of the reflected or diffracted wave can also be included as

$$e_{y'x} = e_{ox} \sin\phi_o \tag{8.22}$$

Thus the total horizontal electric field is

$$e_{y'} = (e_{oy} - 1) \cos\phi_o - e_{ox} \sin\phi_o + \cos(\alpha - \phi_o) \tag{8.23}$$

The horizontal component of electric field relative to the single incident field at the front center of the working volume (y' = 0, x' = 20M) is

$$e_{y'r} = \frac{e_{y'(y',x')}}{e_{y'(y'=0,x'=20)}} \frac{R_{(y'=0,x'=20)}}{R_{(y',x')}} \tag{8.24}$$

By the law of cosines, the value for R is

$$R = \sqrt{R_o^2 + R'^2 + 2R_o R' \cos\phi} \tag{8.25}$$

where

$$R' = \frac{x'}{\cos(\phi - \phi_o)} \tag{8.26}$$

The value for α can be obtained from

$$\alpha = \tan^{-1} \frac{R' \sin\phi}{R_o + R' \cos\phi} \tag{8.27}$$

The results shown in reference 7 are for a step rise in voltage. Within the superposition zone the composite field rises to a fixed level with a finite duration in terms of the normalized time τ and then decays. It must be established whether the rise characteristics of a real pulse are long or short compared to the duration of the diffracted pulse. The definition of τ is

$$\tau = \frac{t - x/c}{R'/c} \tag{8.28}$$

where t is measured from the time the plane wave of reference 7 reaches the bend. The normalized time between different values of τ would be

$$\Delta\tau = \tau_2 - \tau_1 = \frac{t_2 - x/c - t_1 + x/c}{R'/c} = \frac{t_2 - t_1}{R'/c} = \frac{\Delta t c}{R'} \tag{8.29}$$

Thus the equivalent real times for the curves plotted against τ would be

$$\Delta t = \frac{\Delta\tau R'}{c} \tag{8.30}$$

As long as the risetime of a pulse is short compared to the duration of the peak of the pulse shapes in reference 7 (see figure 8.3) the radiated wave will rise to the predicted peak. However, if the pulse risetime is comparable to or longer than the duration of the peak in figure 8.3 then the

radiated wave will be rounded off. To compute this effect each of the components in equation 8.23 must be convoluted with the risetime function. The results must then be summed with the proper time delay.

The waveform selected for the rise is an exponential with a 10-90% risetime of 10 nsec or

$$e_{inc} = 1 - e^{-\beta t} \quad . \tag{8.31}$$

where

$$\beta = \frac{\ln 9}{\text{10-90\% risetime}} = \frac{2.20}{10^{-8}} = 2.20 \times 10^{8} \text{ sec}^{-1}$$

A computer program was written to calculate the results of the finite risetime. The recalculation of the e_{oy} and e_{ox} functions of reference 7 was more involved than was justified by the assumptions and approximations in this section. Consequently, the values of e_{oy} and e_{ox} were read from figure 8.3 and used in tabular form.

If g(t) is the response of a system to a unit step function and if $\psi(t)$ is the response of the system to the function f(t) then

$$\psi(t) = \int_{o}^{t} f'(t - t')g(t')dt' \tag{8.32}$$

Note that f is differentiated in equation 8.32. Then equation 8.32 is valid provided that f(0) = 0 which is true for the present case in which $f(t) = 1 - e^{-\beta t}$. From equation 8.23 we see that

$$g(t) = (e_{oy} - 1)\cos\phi_o - e_{ox}\sin\phi_o \tag{8.33}$$

thus

$$e_{y'} = \psi(t) + \cos(\alpha - \phi_o)(1 - e^{-\beta t}) \tag{8.34}$$

After $e_{y'}$ is calculated in (8.34), it is normalized after the method of equation 8.24. The function g(t) is approximated by straight lines.

A field value at intermediate time is picked for the sake of comparison. This is the incident field value $e_{y'inc}$ which is the field that would result from a single source. Two quantities of interest are calculated using $e_{y'inc}$. The first is $e_{y'max}/e_{y'inc}$ which will give a measure of the amount of peaking to be expected. The second is the time for $e_{y'r}$ to fall off from its peak value to an arbitrary value which is 110% of $e_{y'inc}$. This indicates the duration of the peaking effect.

The values for $e_{y'rmax}$, $e_{y'max}/e_{y'inc}$ and the 110% fall-off time are given in table 8.1 for the 18 points selected in figure 8.10. The values of $e_{y'rmax}$ are also plotted in figure 8.11 for different values of x'. This gives the variation of peak fields within the working volume plus some adjacent points.

The foregoing centerpost diffraction discussion shows the following:

(1) The real rise time of 10 nsec is long enough so that the actual peaks are substantially smaller than the peaks would be predicted from a step function.

(2) The resulting early-time electric field nonuniformity (neglecting fringing fields) is less than the dc limit in section IV.

(3) The time for the diffraction effects to decay down to no more than 10% greater than the incident field is shorter at the front than at the rear of the working volume so that nonuniformity decays faster at the front. The time varies on the centerline from 12 nsec at the front to 89 nsec at the rear, but the initial amplitudes are down somewhat at the rear to compensate for this effect.

x' (Meters)	y' (Meters)	$e_{y'rmax}$	$\frac{e_{y'max}}{e_{y'inc}}$	Fall Time to 110% (nsec)
20.0	0.	1.000	1.14	12.0
*20.0	3.17	.998	1.14	2.0
*20.0	6.50	.985	1.12	0.7
*20.0	10.19	.970	1.10	0
38.9	0.	.953	1.26	29.8
38.9	6.16	.926	1.22	11.8
38.9	12.64	.890	1.17	4.1
38.9	19.82	.858	1.13	0
57.8	0	.906	1.36	50.1
57.8	9.15	.843	1.26	23.4
57.8	18.78	.796	1.19	10.1
57.8	29.45	.758	1.14	0
76.7	0	.862	1.45	69.0
76.7	12.15	.770	1.29	36.3
76.7	24.92	.716	1.20	16.1
95.7	0	.828	1.54	89.3
*95.7	15.16	.707	1.31	48.4
*95.7	31.09	.649	1.21	20.1

*Outside of working volume.

Table 8.1

Computed values

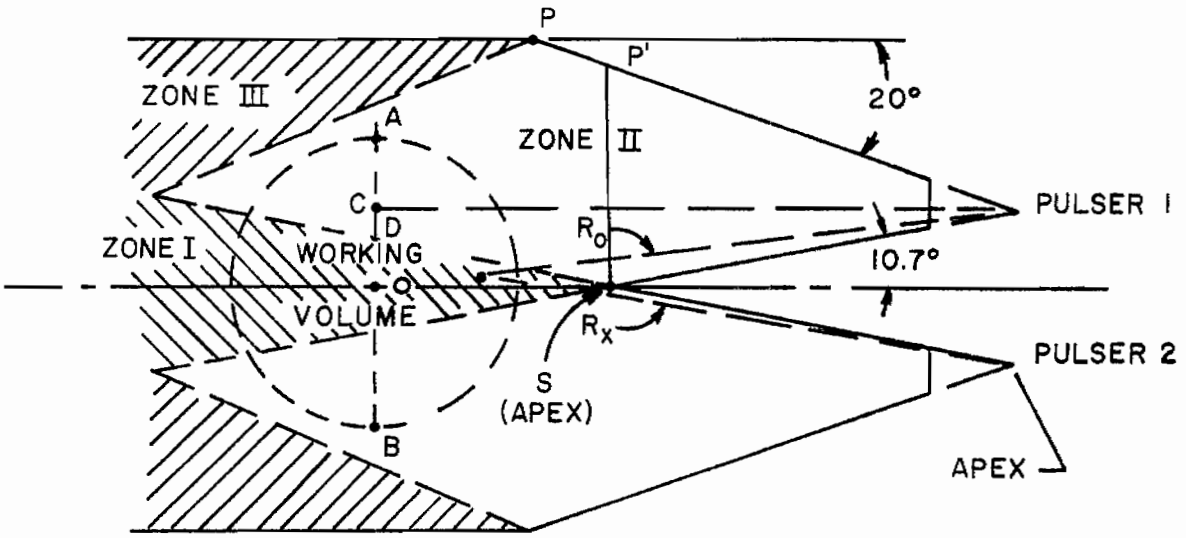

Figure 8.1. Diffraction and reflection zones.

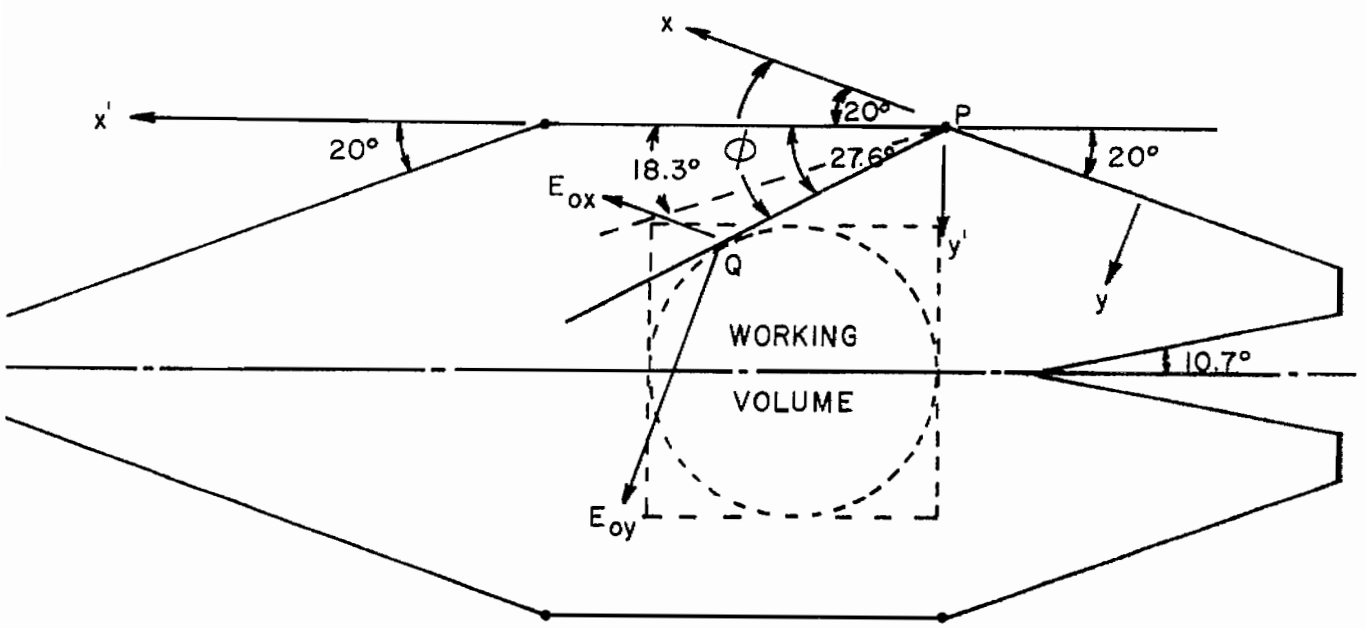

Figure 8.2. Geometry for diffraction into the working volume from the first bend in the outer plate.

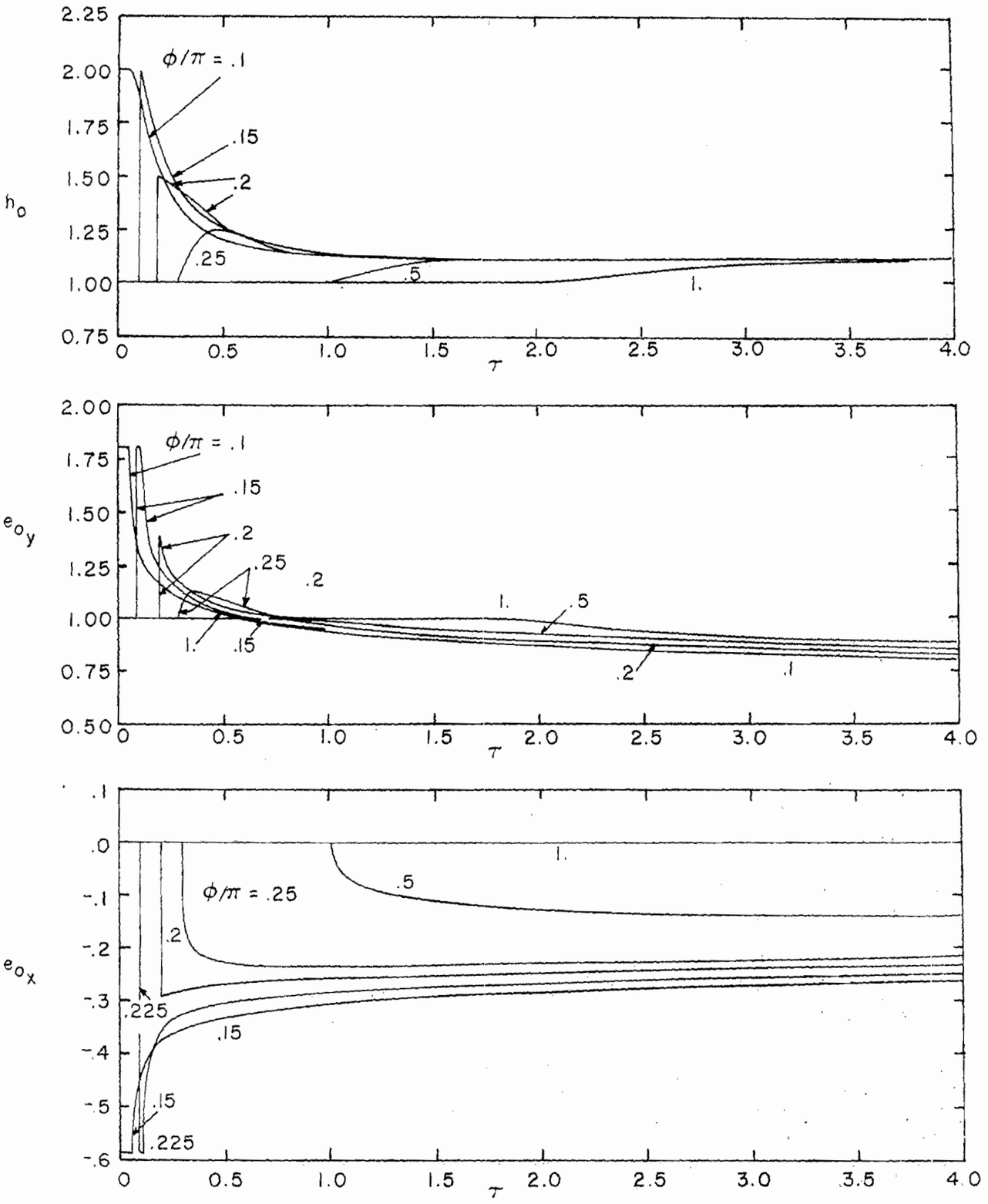

Figure 8.3. Pulse shapes for diffraction of a step function wave at a bend in a perfectly conducting sheet: $\phi_o/\pi = .1$.

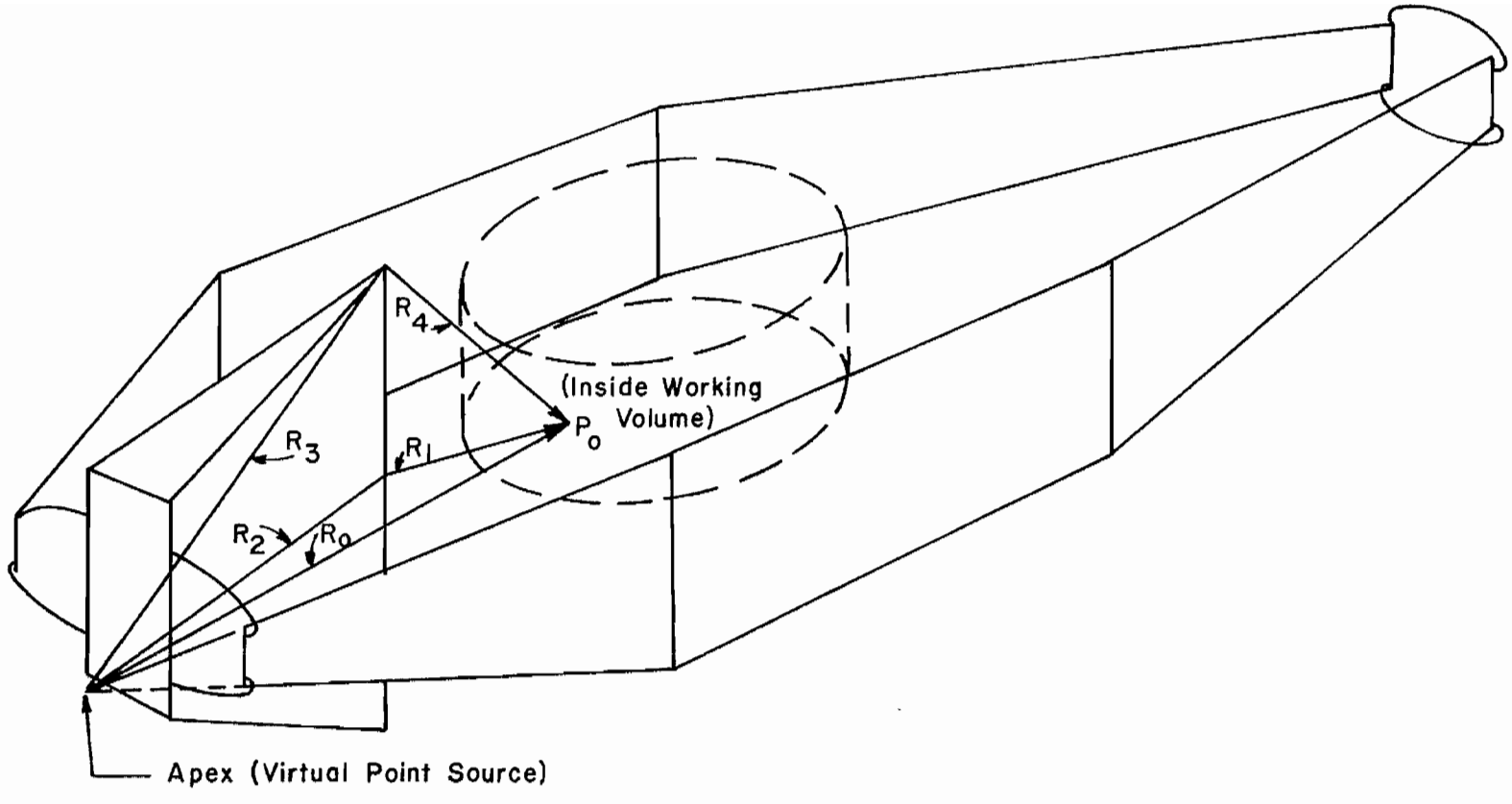

Figure 8.4. Ray paths to a point in working volume for diffraction calculations.

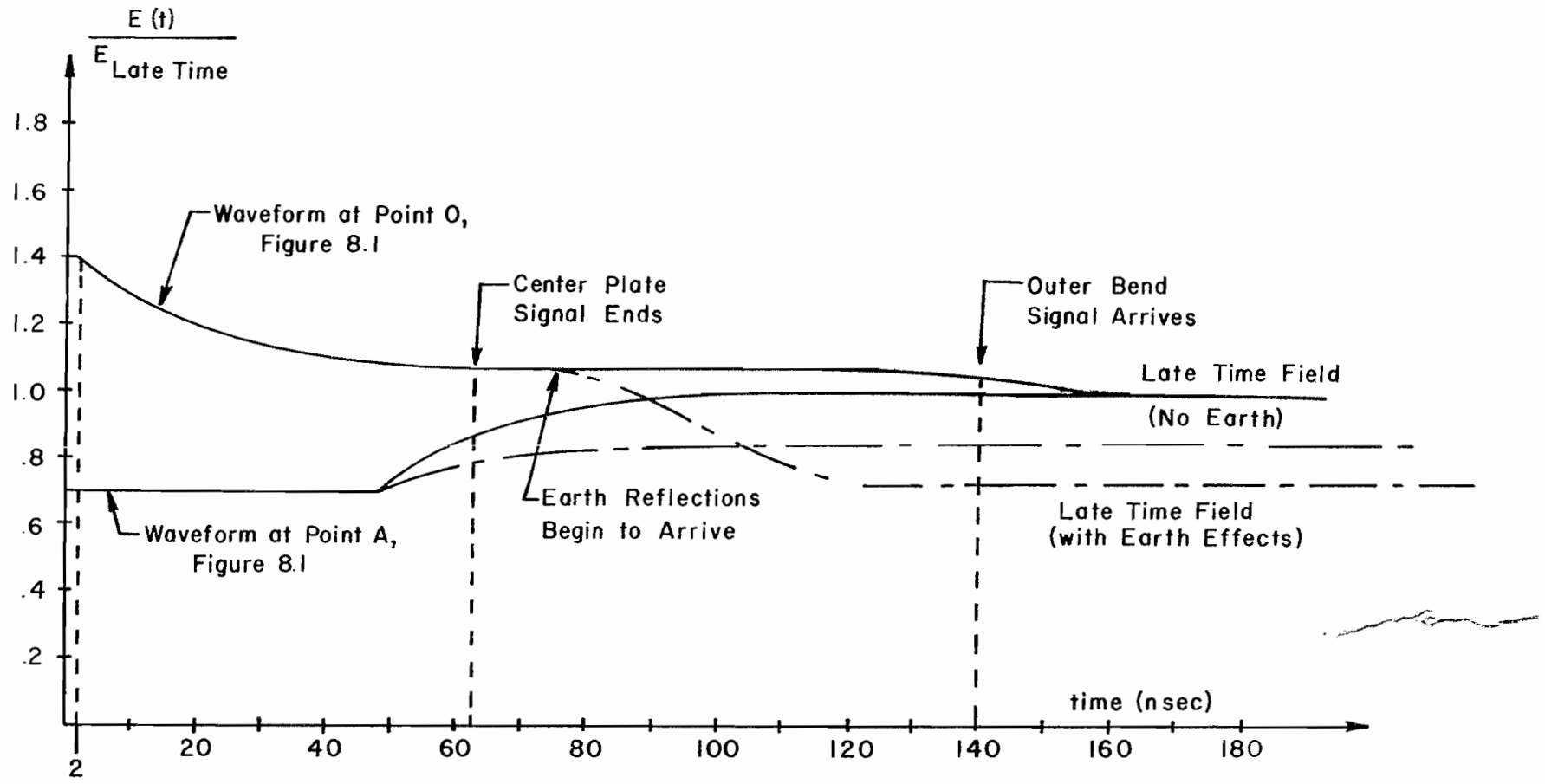

Figure 8.5. Transverse E field pulse, showing diffraction effects, assuming ideal step function pulse generators.

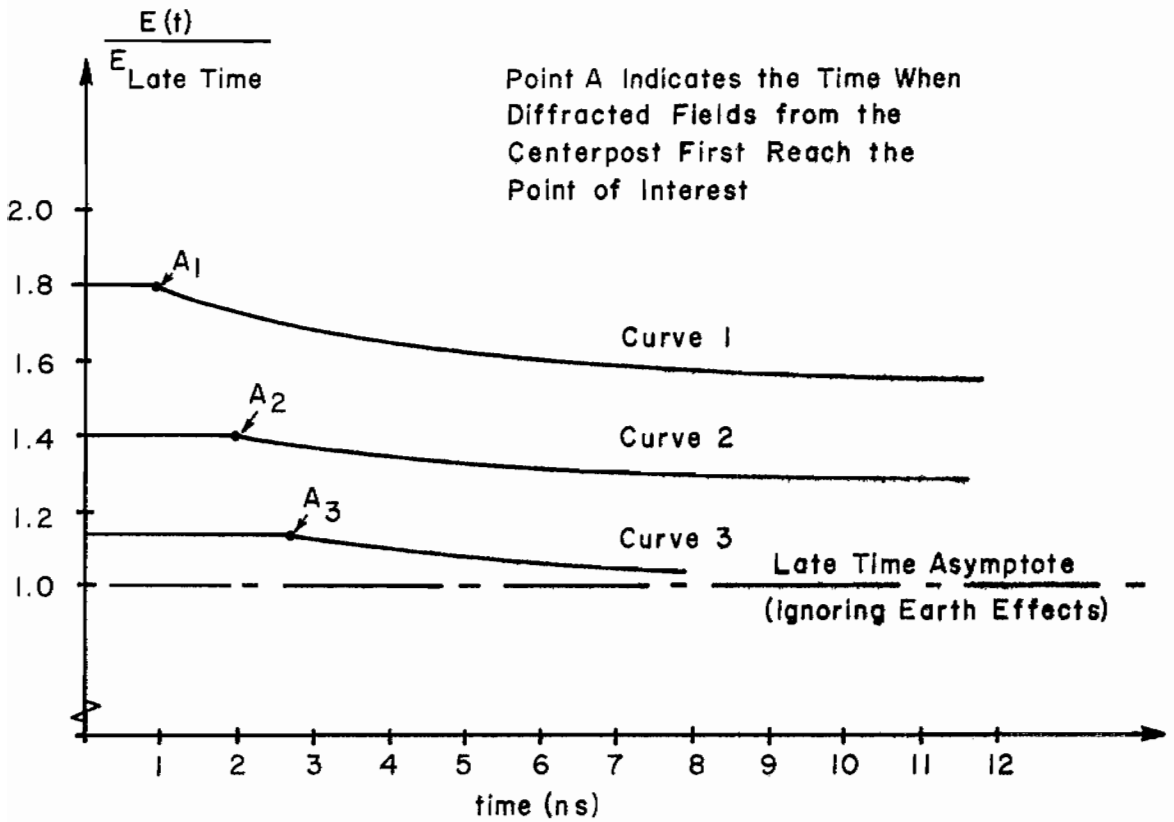

Curve 1 - front edge of working volume
Curve 2 - mid-point of working volume
Curve 3 - back edge of working volume

Figure 8.6. Early time fields along the center line of the working volume.

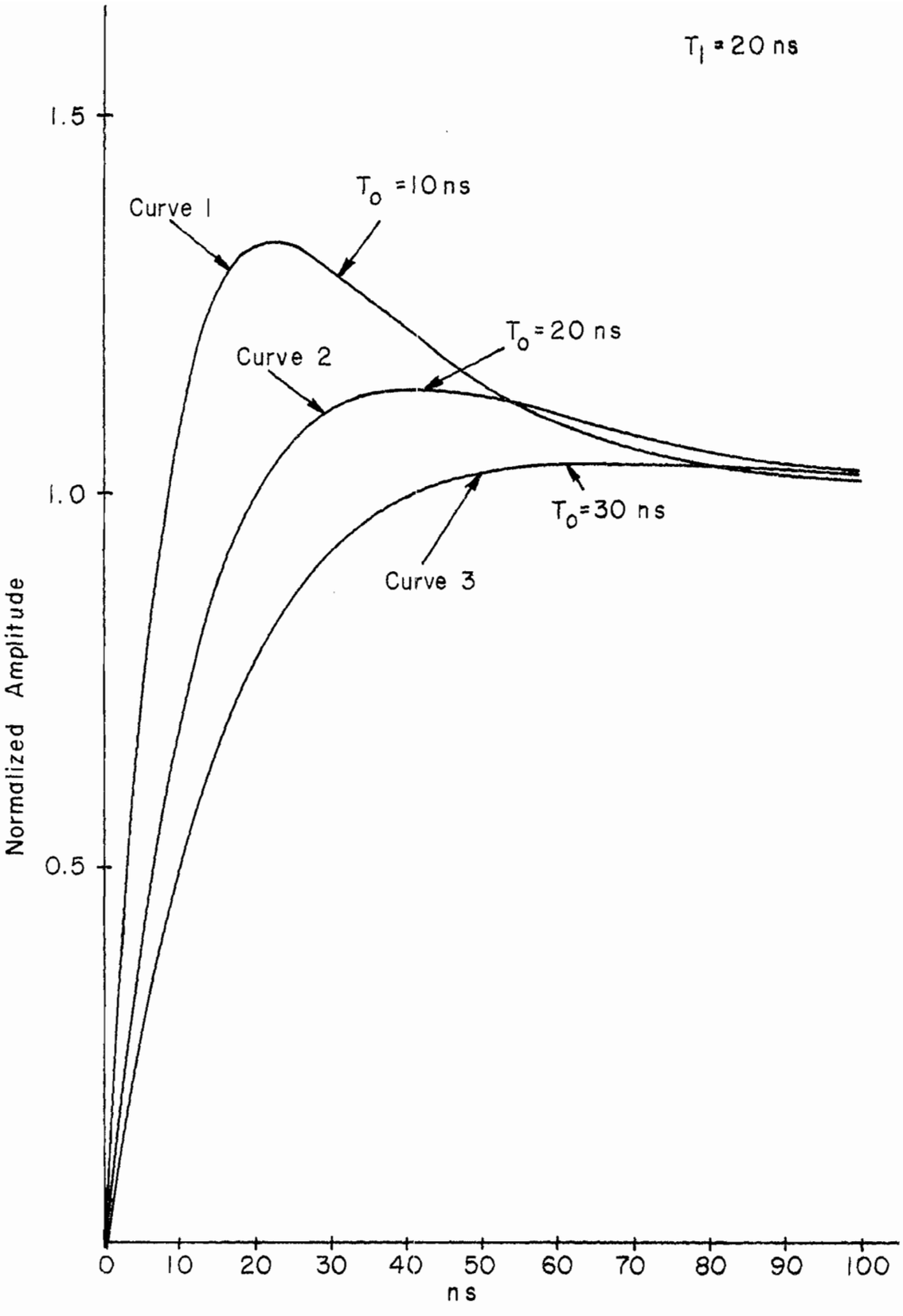

Figure 8.7. Effects of finite risetime on peak amplitude.

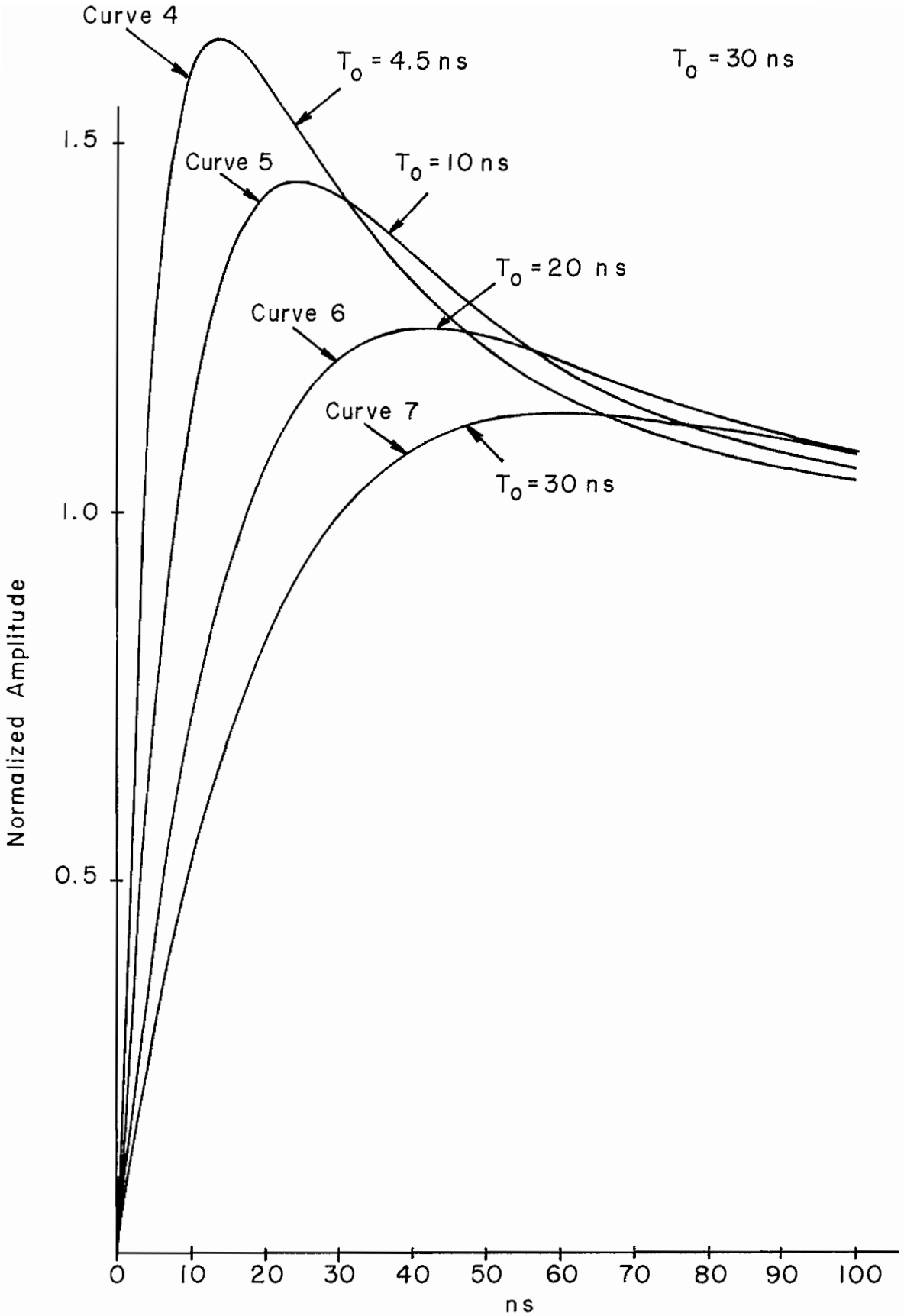

Figure 8.8. Effects of finite risetime on peak amplitude.

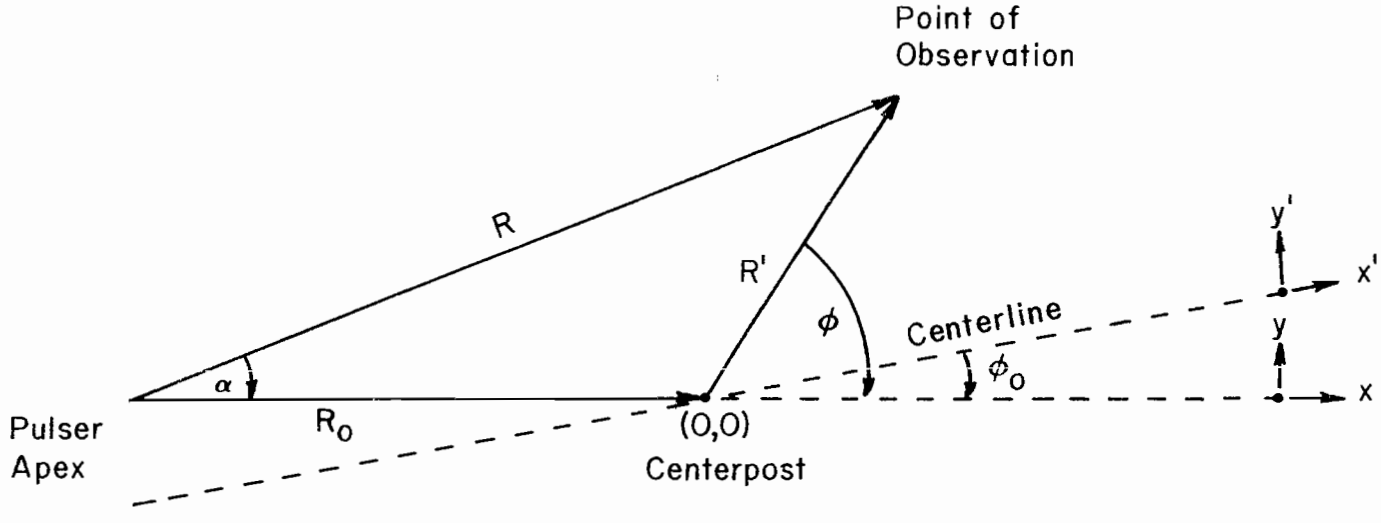

Figure 8.9. Configuration for computations.

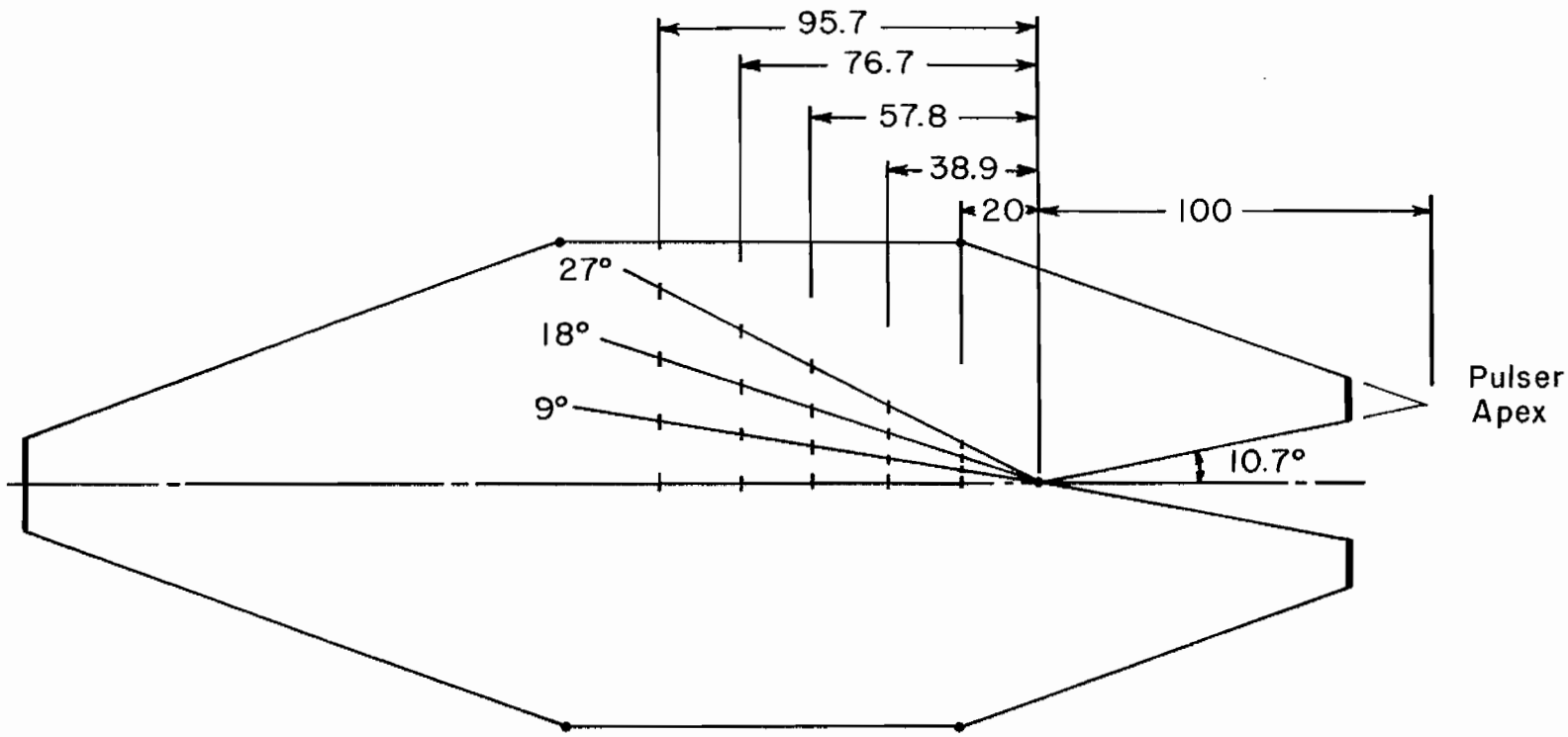

Figure 8.10. Positions of computation (meters).

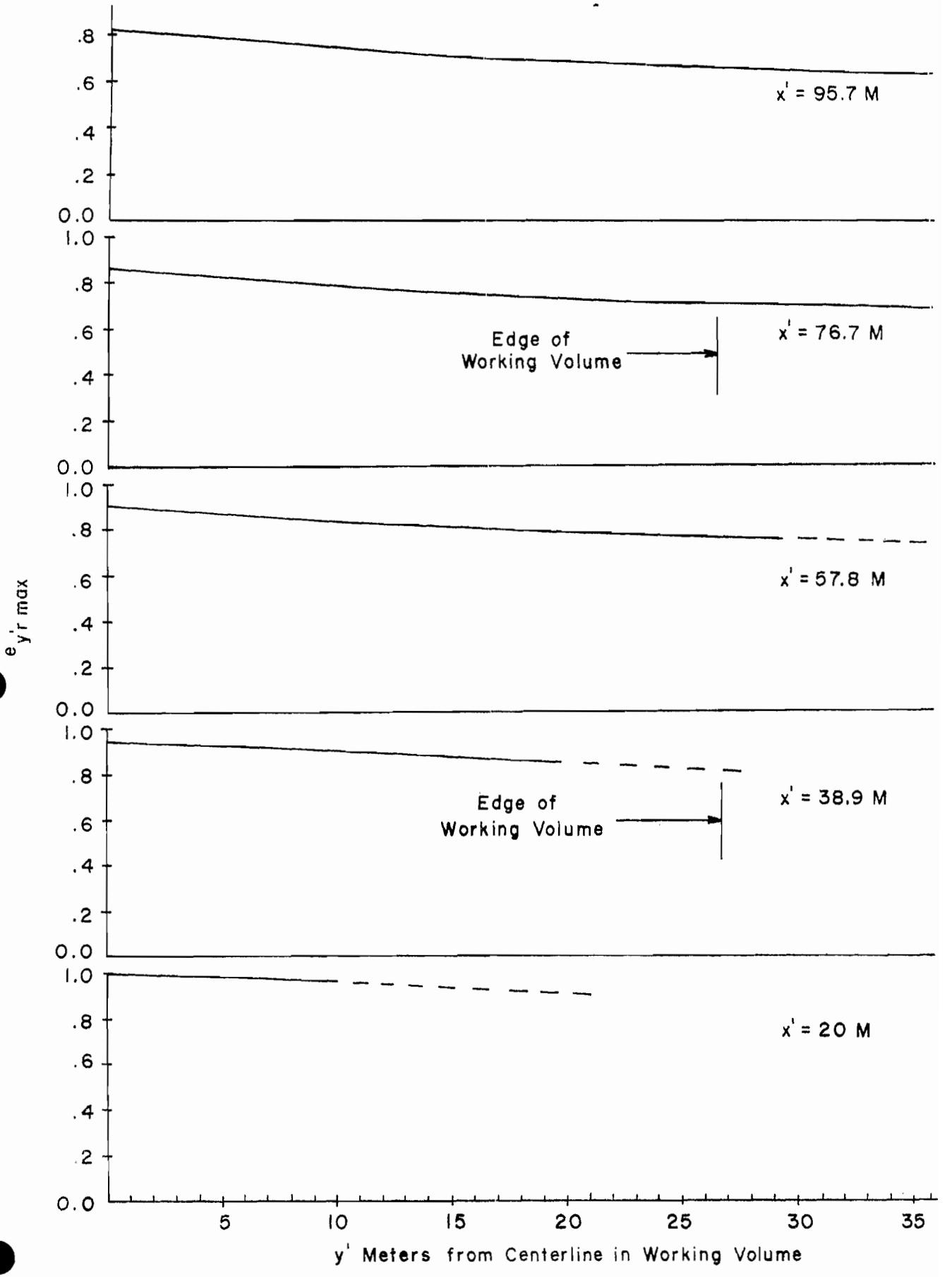

Figure 8.11. Peak horizontal electric field compared to value at x' = 20M, y' = 0 (front center of working volume).

IX. Reflection and Diffraction from the Earth

Geometrical optics can be used to examine still another reflection phenomenon, namely the effect of signals reflected from the ground beneath the simulator into the working volume. During a time interval comparable to the transit time across its face, the pulse source launches a wave which is peaked in directions away from the ground (references 37, 38) including a strong peak toward the working volume; it still radiates somewhat in all directions. With a nominal face dimension of 12.5 meters, we might expect significant radiation from the pulser in all directions for a time of approximately 40 nanoseconds. After this time, radiation from the pulser in directions other than directly toward the working volume can be considered negligible.

From the side view of the simulator shown in figure 1.5, it is clear that the earth's surface beneath the input transition sections will produce at least one direct reflection path for this early-time pulser radiation to travel into the working volume, unless the earth is sloped downward moving out from the central ground planes.

If the earth were a perfect conductor, then this reflected wave would have polarization opposite to the direct wave from the pulser, and attenuated only by the 1/r factor introduced by the longer path length of the reflected signal as opposed to the direct signal. From figure 1.5, a typical ground reflection path would appear to be 25 percent longer than the direct path if it were to reach the working volume, so the perturbing signal would have about 80 percent of the amplitude of the direct signal and would in addition be opposite in polarity. Several factors will reduce this effect.

First, by "sloping" the pulser array toward the working volume, as is discussed in reference 37, the early-time radiation can be made less isotropic with less signal downward. This will reduce the amplitude of the spurious signal reflected from the earth into the working volume. Secondly, the earth is of course not a perfect reflector. In fact, it can be made to absorb very high frequencies (those with a period much less than the relaxation time constant of the earth) selectively according to the angle of incidence of the energy. Such "Brewster Angle" absorption for that part with polarization of the magnetic field parallel to the ground is discussed in reference 6, and these considerations should be included in determining the final shape of the earth's surface beneath the input transition sections.

A third mitigating factor is that the ground reflection will be significantly delayed with respect to the direct signal in the working volume. If the ground reflection path is in

fact 25 percent longer than the direct path to the center of the working volume, then the reflected signal will arrive about 130 nanoseconds after the primary signal in the working volume. Its effects will then be well separated from the leading edge of the pulse. These numbers apply at the front of the working volume.

In estimating the amount of signal reflected from the ground we need an estimate of the signal strength incident on the ground in the direction toward the reflection position on the ground. Consider the electric field distribution in the TEM mode launched onto the conical transmission line. Other modes are also present but difficult to estimate in the present state of the art.

Consider the field strength ignoring ground effects at 50 m below the centerline with the side plates at about 55 m away from the central ground plane near the main centerpost where the ground planes join. The side plate is about 33 m wide at this position. This gives a b/a ratio of about 3.3 for use with reference 8 which has potential plots for b/a of 2 and 5. Considering a position halfway between the central ground plane and the side plate (y/b = .5 in that note) the field falls off from x/b = 0 to x/b = .91 to between 40% to 60% of the value in the center (x/b = 0, y/b = .5). The electric field orientation is also changed reducing the horizontal component about 10% from the electric field magnitude there. The reflected field is further reduced by a 1/r effect compared to the direct incident field by about 10% at the working volume. So 30% to 50% might be a reasonable estimate of the reflection of the horizontal component of the TEM electric field for this typical path halfway between the outer plate and central ground plane. This, of course, assumes a perfectly horizontal earth at the reflection position under the transmission line. These high frequency reflection numbers change somewhat for different reflection paths.

One should also note that there need be no direct reflections into the working volume if the earth is shaped properly. In particular, if the earth is sloped downward as one moves out from the center ground planes, the earth's curvature can be designed to cause reflection paths to miss the working volume entirely in addition to dispersing the reflected energy over a larger volume. At least some such sloping will tend to reduce the direct reflection contribution by dispersing it out somewhat. At low frequencies, of course, the reflection converts over to the reduction of the fields in the working volume considered in section IV.

If all of the mitigating factors are applied, it is probable that the total field perturbation caused by ground-reflected signals can be kept within 20 percent of the peak amplitude of the main pulse and will in addition be quite short

in duration (less than 20 nanoseconds). Techniques of shaping the pulser array can be used not only to redistribute the radiation pattern from the pulser, but will also in general tend to reduce the time duration of spurious radiation in preferred directions; this effect can be used to reduce the duration of the reflected ground pulse. If some of the very high frequencies contained in this "ground pulse" can be attenuated by careful shaping of the ground surface and control of the ground moisture content (by using a plastic film ground cover, for example) then not only will the reflected pulse fall rapidly but it will also rise more slowly than the main pulse and these effects will further reduce its net amplitude.

Now let us try to make a few quantitative estimates of actual reflection coefficient of the finitely conducting earth using relative dielectric constants and conductivity measured at a site near that proposed for the simulator. These specific parameters will be used in applying the theory developed in reference 40 for the specific case of interest.

Typical measurements give an average conductivity of about .02 mho/meter and an average relative dielectric constant of about 20 for earth typical of that found near Kirtland AFB (at a frequency of 1 MHz). These values vary considerably with location and frequency but are probably reasonable for first cut estimates of reflection coefficients. Reference 40 calculates the reflection waveform of a step-function incident on a conducting dielectric. The geometry is shown in figure 9.1 and the results reproduced in figure 9.2. The time scale in figure 9.2 is normalized by the expression

$$\tau_r = \frac{t}{t_r}$$

where t is the time and

$$t_r = \frac{\varepsilon}{\sigma} = \frac{20 \times 8.85 \times 10^{-12}}{.02} = 8.85 \times 10^{-9} \text{ s}$$

With a scale factor of this size, a τ_r of 100 corresponds to a time of only .9 ns and figure 9.2 thus indicates that the ground is almost a perfect reflector for times greater than several nanoseconds. Note that the assumption of frequency independent conductivity and dielectric constant is somewhat suspect. However, the general conclusion that most of the energy of the pulse will be reflected off the ground is still probably justified.

From the above considerations, it can be seen that it is probably desirable to slope the ground below the simulator so that as much energy as possible is not reflected into the working volume. First, assume a planar earth and use geometrical optics to find the point where the reflection just misses the working volume. (See figure 9.3.) Using design 1 dimensions we find that this point is 17 meters from the front of the working volume. This indicates that the earth between this point and the pulser should be sloped so as to reflect the incident pulse away from the center of the transmission line. Further details on this ground sloping should be considered as the design progresses. Again reference 34 gives general guidelines for the local earth contouring.

Similar considerations need to be taken when planning the ground contours under the output transition section and the earth shaping exterior to the transmission line. The ray tracing techniques of geometrical optics should be used to insure that the earth is shaped so that single (or multiple) reflections return a minimum of energy to the working volume.

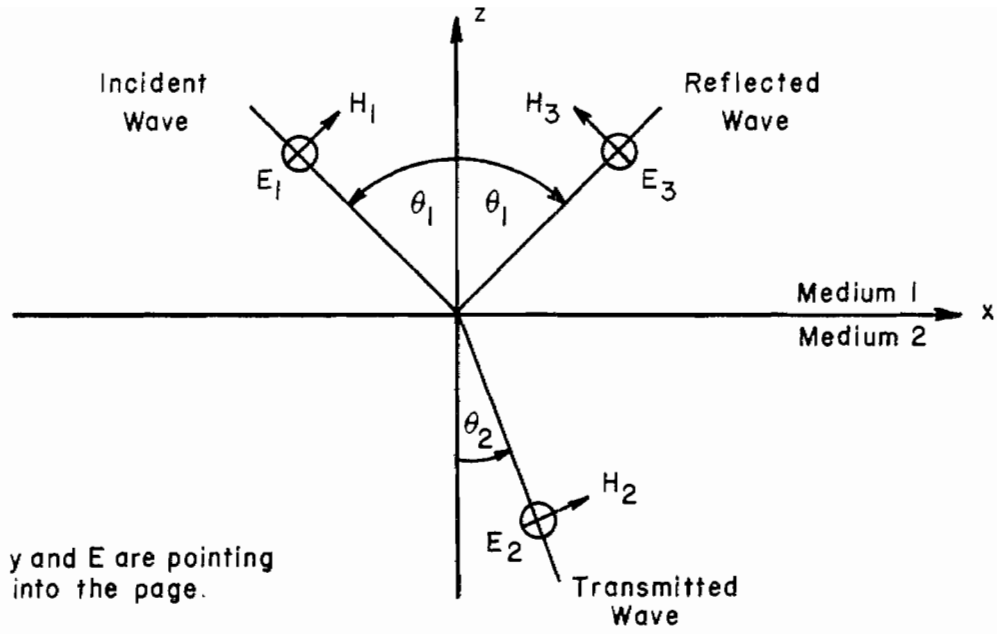

Figure 9.1. Reflection Geometry: E parallel to interface.

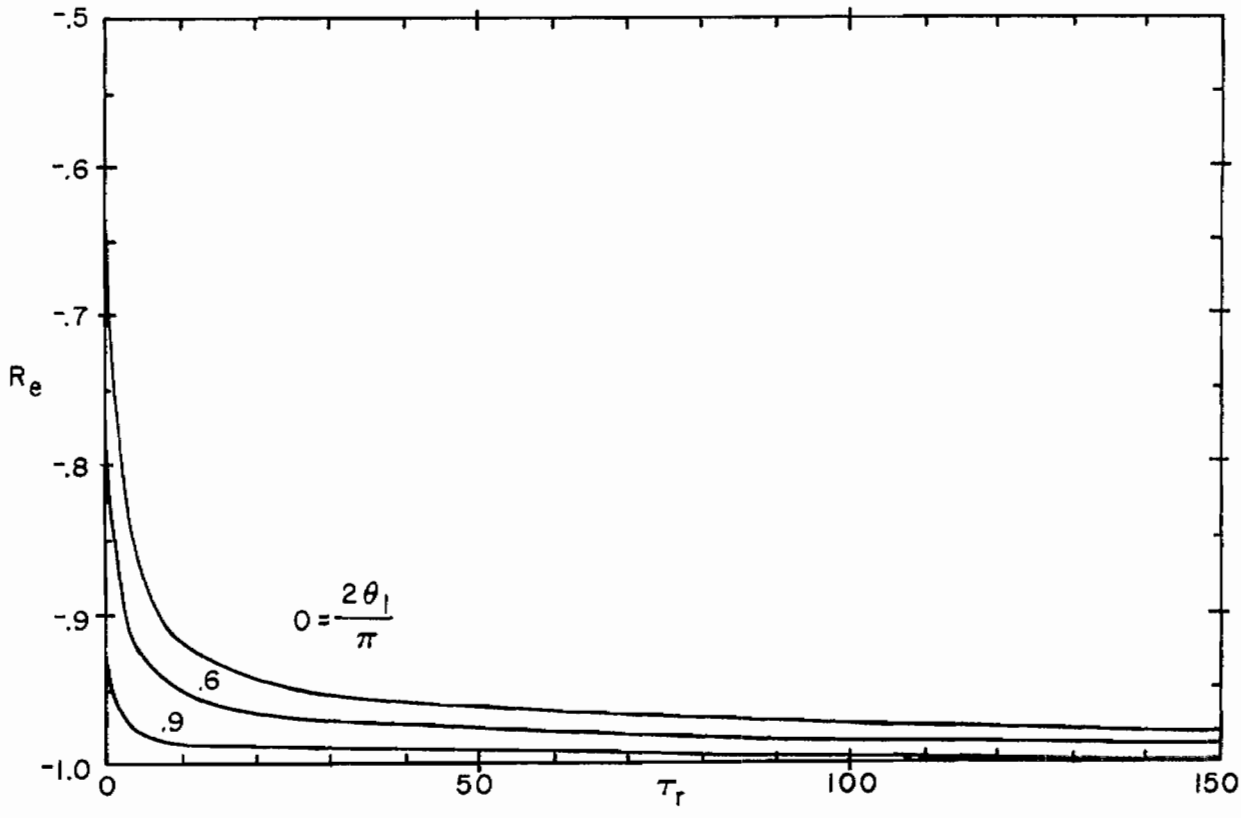

Figure 9.2. Reflection of step function wave with electric field parallel to interface: $\epsilon_r = 20$.

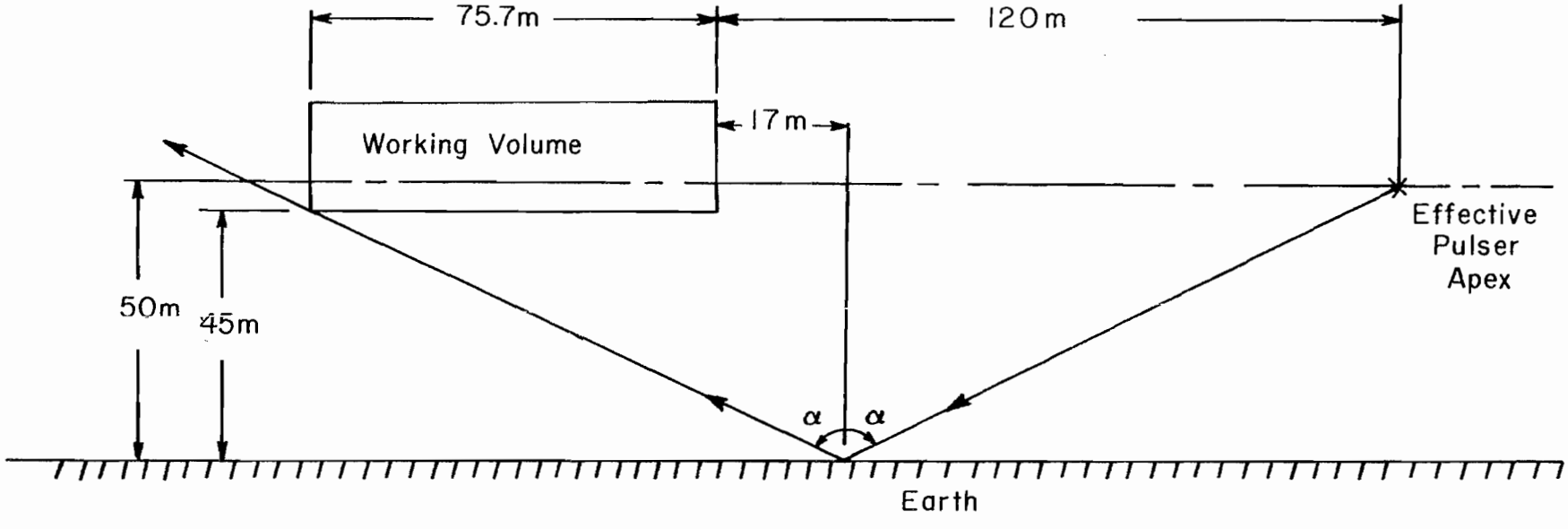

Figure 9.3. Geometry such that ground reflection is tangent to the working volume.

X. Reflections in the Output Transition Section

The question of high frequency multiple reflections in the output section of the simulator can be treated by ray tracing techniques of geometrical optics.

The multiple reflection question is treated in general terms in figure 10.1. The ray (dotted line) is at angle ϕ with the centerline of the simulator.

The terminator transition plate is at an angle α from the centerline. By Snell's Law the angle of incidence of the ray with the terminator transition plate is the same as the angle of reflection. By geometry the incidence angle is $(\alpha + \phi)$. Therefore the angle the reflected ray makes with the centerline is $(2\alpha + \phi)$. By the same argument it can be shown that the angle the ray makes with the centerline after its reflection from the opposite plate of the terminator transition is $(4\alpha + \phi)$. In general, after n such reflections the angle of the ray with the centerline is $(2n\alpha + \phi)$.

When the $(2n\alpha + \phi) > \pi/2$ then the ray is returning toward the working volume; this occurs after the second bounce when $\phi = 19°$, which is the worst possible case. By geometrical ray tracing it was determined that this ray did not actually enter the working volume until after the fourth bounce. See figure 10.2.

Since the ray is an element of a spherical wave front, its peak amplitude will be attenuated by an inverse distance factor which is approximately 0.25, obtained by direct measurement of path lengths. Also, this reflected pulse will arrive quite late in time, reaching the center of the working volume approximately 1.5 microseconds after the onset of the main pulse. Finally, from diffraction concepts it can be seen that the duration of this multiply reflected pulse will be quite short, probably less than 10 nanoseconds, and so it may very well not even be observed when the finite rise time of the pulse source itself is taken into account.

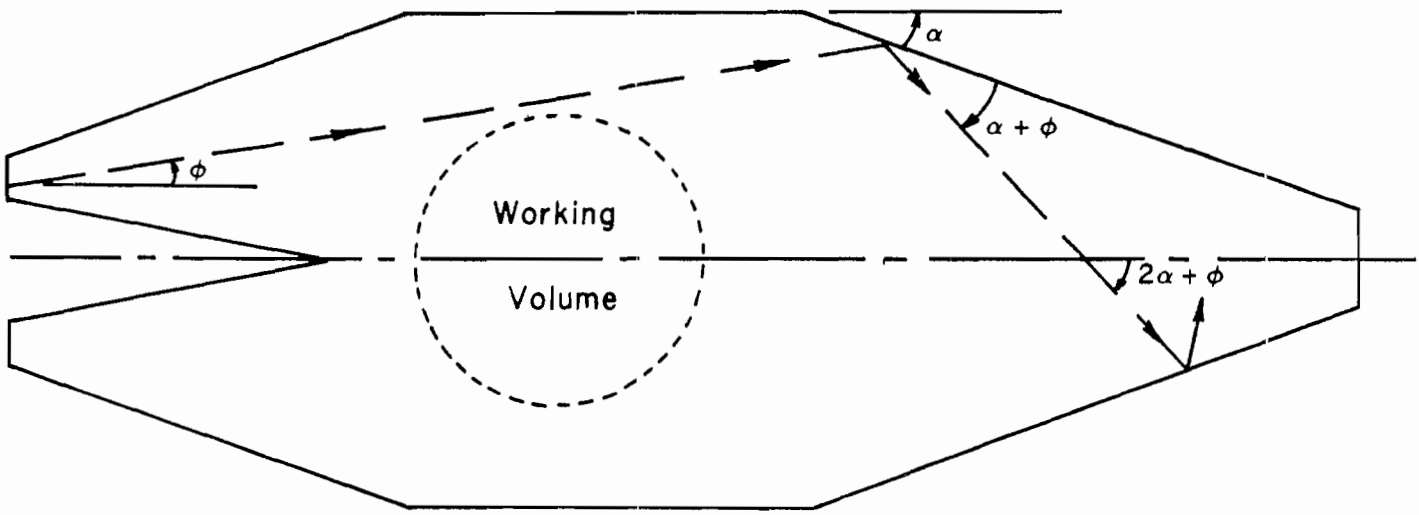

Figure 10.1. Geometry for reflections in the output sections.

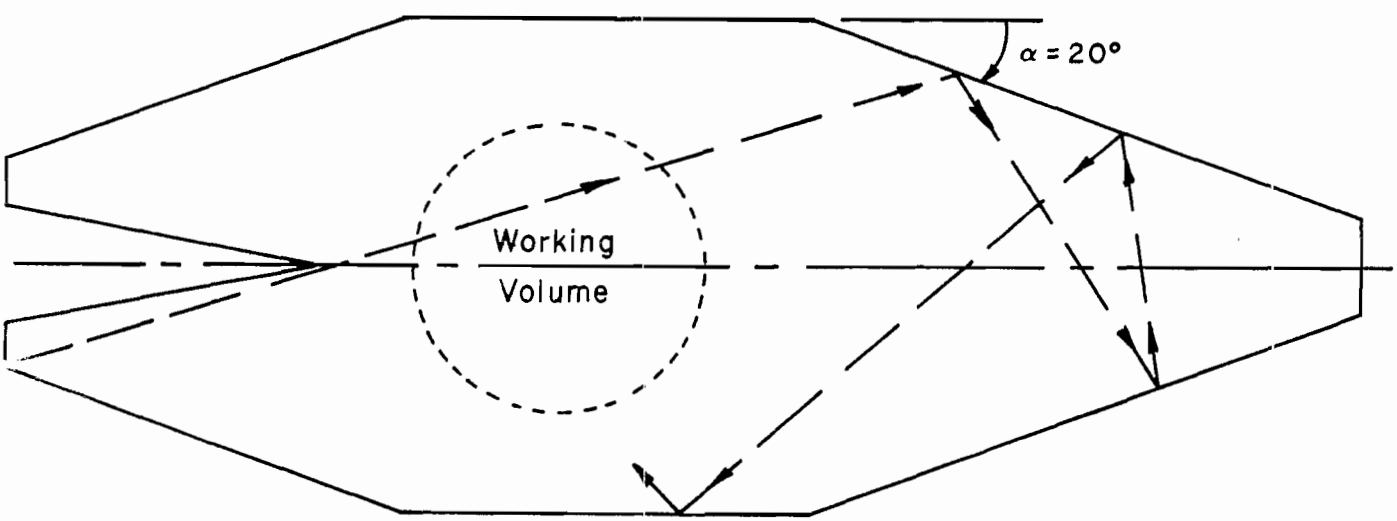

Figure 10.2. Reflections back into the working volume.

XI. Differential and Common Mode Termination

Terminating a horizontally polarized transmission line is a more complicated task than one might expect from experience with previous vertically polarized transmission line EMP simulators. First of all, the large size of the transmission line requires some sort of admittance sheet terminator rather than a simpler resistive termination. Secondly, the presence of the ground creates the possibility of a common mode signal propagating down the line when the two pulser arrays are out of balance. These questions are discussed in reference 36.

As a first cut, let us form an equivalent circuit for the simulator, remembering that circuit theory and impedance matching are only first-cut approaches to proper termination. The equivalent circuit is shown in figure 11.1 where the terminator geometry of figure 11.2 is assumed.

Z_{CM} is in parallel with $Z_{DM}/4 + \Delta Z$ (since the two $Z_{DM}/2$ are in parallel. The $2Z_{CM}$ is the impedance from a plate to ground which is discussed in section V. The differential mode impedance, Z_{DM}, is just the plate to plate impedance. With the line terminated in two equal impedances of $Z_{DM}/2$, the Z_{DM} is just the termination impedance. One wishes to have the Z_{CM} to be equal to the impedance in parallel with it or

$$Z_{CM} = \Delta Z + \frac{Z_{DM}}{4}$$

or

$$\Delta Z = Z_{CM} - \frac{Z_{DM}}{4}$$

From section V, we can find Z_{CM} since $Z_{CM} = Z_g/4$. The values of Z_{CM}, Z_{DM} and ΔZ as a function of z, the distance from the apex of one pulser input transition section toward the terminator, are given in table 11.1. In order to obtain values for $z > 220$ m, one needs to assume a value of the distance from the bottom of the termination to the ground as well as a width of the termination. Using the specification of 1 MV/m maximum stress, the terminator ends up 17.6 m from the ground and 35.2 m wide. The differential mode impedance as a function of z is obtained from references 2, 16, and 39.

The results for various values of z are listed in table 11.1. For values of $z < 100$ m we get $\Delta Z = 0$ because the ground plane between the outer plates of the input transition sections causes the circuit for the differential mode to be identical to

the common mode. This is true as long as the circuit on one side has not communicated with the one on the other. The time at which this communication takes place and the effect of this communication on the different modes is too complicated for the present analysis.

From table 11.1, one can see that the value of ΔZ to be used as shown in figure 8.5 should be 2-3 Ω. With such a small value, it may be adequate to set $\Delta Z = 0$. The values of the dimensions of the terminator may be incorrect and the effect of changing them should be looked at later. However, the likely changes should have little effect on ΔZ. The value of ΔZ in the input transition region is elusive due to the changing current path in the center ground plane as a function of time as well as the time varying "cross talk" between the two input sections. Since, to a first approximation, $\Delta Z = 0$ for $z \leq 100$ meters the correct value will not be very large and the values in the regions of $z > 100$ meters are reliable enough to justify a working value of $\Delta Z = 0$ throughout.

It is likely in any case, however, that the common-mode terminating system will have to be tailored to the characteristics of the pulser array and site when the system is finally installed. Furthermore one might wish to adjust this common-mode termination from time to time to compensate for changes in soil moisture content and possible aging effects in the pulser arrays.

The inadequacy of a purely resistive termination is discussed in reference 9 and thus one needs to consider a more complicated approach for termination design, such as some type of admittance sheet.

A generalized admittance sheet for ideal termination (i.e., reflectionless) is considered in references 12 and 17 and it is pointed out that an ideal admittance sheet is not, in general, realizable in terms of lumped passive elements. For this simulator, an ideal termination can probably be fairly well approximated by an admittance sheet consisting of series inductance and resistance elements. It is pointed out in reference 9 that an LR admittance sheet will properly terminate both the low and high frequency elements of a pulse traveling down a transmission line with some reflection of the intermediate frequency range. A particular realization of such a distributed LR admittance sheet is discussed in reference 20. This note specifically considers the use of an array of sloped resistive rods as the termination. This technique was developed for terminating the SIEGE type of simulator, and it is felt that a similar technique might well be used here. The resistive rods are made up of strings of individual wire-wound resistors so that the wire winding of the resistor is the main source of inductance. One can consider shaping these resistive rods to run

along the lines of electric field of the transmission line field distribution with the resistors spaced according to the equipotentials.

	z (m)	x_o (m)	x_1 (m)	Z_{CM} (Ω)	$Z_{DM}/4$ (Ω)	ΔZ (Ω)
(1)	344	16	26.5	82	80	2
(2)	282	23	48.2	73	71	2
(3)	220	30	70	69	65	4
(4)	120	30	70	69	65	4
	(Just beyond the centerpost)					
(5)	100+	33.3	66.6	75	67	8
(6)	< 100					0

z = 344 is the terminator location

z = 282 is midway between the terminator and the termination transition section-transmission line interface

z = 220 the above interface

z = 120 the transmission line-input transition section interface

z = 100 the centerpost location

Table 11.1

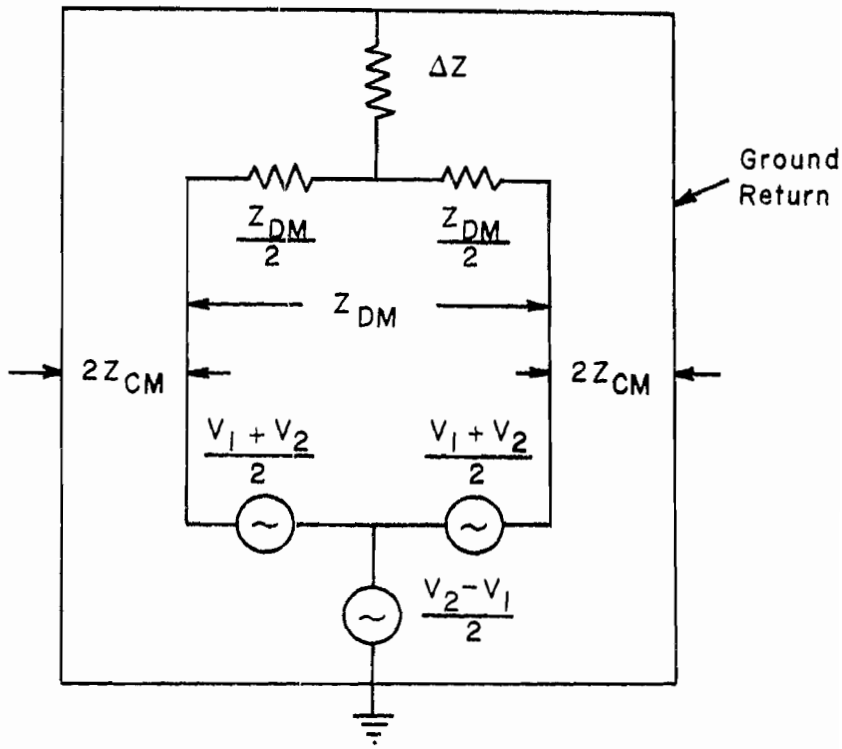

Figure 11.1. Simulator equivalent circuit.

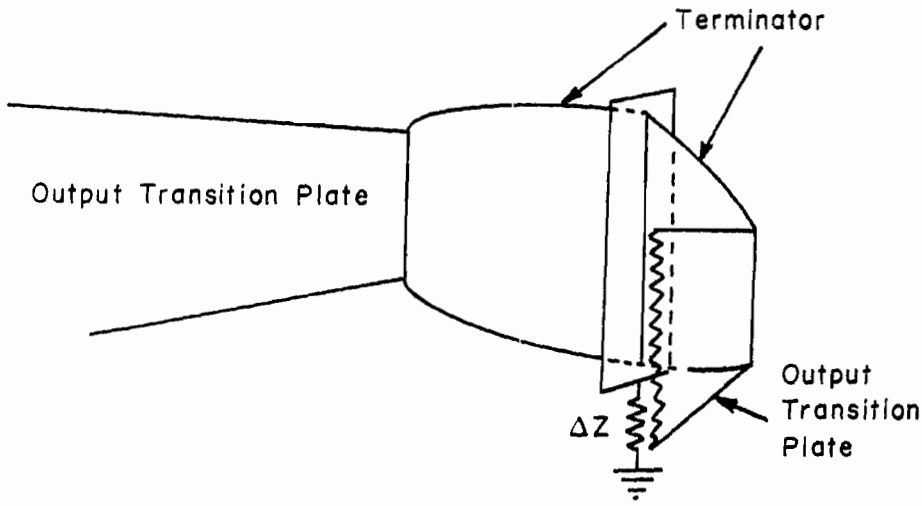

Figure 11.2. Terminator geometry.

XII. Summary

If the reader is to get an impression of the present state of the art in the design of large transmission line EMP simulators we would hope that it would be this: while much more is known about the details of the electromagnetic performance of such simulators than a few years ago, still it is not (and probably will never be) perfect. As more relevant electromagnetic boundary value problems are solved and documented in formulas, tables, and graphs both more answers will be known and more questions will be asked. At present we have some idea of what are some of the important questions that can be asked but future reports should refine this.

The following table summarizes some of the approximate distortion numbers for ATLAS I, design 1, for a 75.7 meter (horizontal dimensions) working volume with $\vec{E}_{avg}$ equal to 200 kV/m and horizontal with respect to the earth. If the reader wishes to understand more about the details of how these approximate numbers were derived he may refer back to appropriate sections in the body of this report.

Thus we have a summary of some pertinent electromagnetic design numbers for ATLAS I, design 1. These may be refined and more figures of merit added in the future. Furthermore, another design (specific set of dimensions) is being considered and other designs may be considered as well. The comparison of the electromagnetic numbers among these designs is of utmost importance.

Note that the present note deals primarily with the simulator structure. The pulser array design is another issue. As such the present note is primarily concerned with simulator response functions which can be approximately convolved with the waveform launched by the pulser array (reference 38).

This note does not consider every detail in the design of ATLAS I, design 1. It puts numbers on some of the major issues as far as the present state of the art will allow. In building such a simulator the reader should be familiar not only with this note, but with references 34 through 38 as well in particular. There are many design guidelines discussed in these references which can improve the performance and utility of this simulator.

Summary of Design 1 Performance

Interaction of Aircraft with Side Plates (section II - worst case) (all ratios relative to free space)

Current density ratio (time domain) - .83
Current density ratio (freq. domain) - .73
Charge density ratio (time domain) - .99
Charge density ratio (freq. domain) - .85
Decay time ratio - .60

Interaction of Aircraft with Ground (section III)

Less than 20% variation from free space

Low Frequency Uniformity (section IV)

Worst case - bottom outer edge of working volume - 44% variation from average

Pulser Voltage (for 200 kV/m) - 35.2 MV (100 kV/m implies 17.6 MV)

Transmission Line Impedance (section V)

Assuming a perfectly conducting earth - 258 Ω
Ignoring earth effects - 304 Ω

Impedance along Input Transition (section VI)

~320 Ω at nominal pulser location (total)

Planarity across Working Volume (section VII)

~3.8 nanoseconds at center of working volume

Diffraction Effects from the Bend in the Outer Plates (section VIII)

Less than 20% in working volume at outer edge - considerably less farther in

Diffraction at Apex of Center Ground Plane Wedge (section VIII)

Peak of 1.8 E late time at front of working volume (worst case)
Peak decreases "effective" risetime across working volume

Reflection from the Earth (section IX)

Earth contouring below wave launching section necessary to avoid direct reflections at high frequencies
A typical relative value for this reflection considering only the incident TEM wave is a negative 30% to 50% for the horizontal electric field from a horizontal earth surface

Reflections in Output Transition Section (section X)

4 reflections before return to working volume (very fast time components only)

Table 12.1

XIII. References

SENSOR AND SIMULATION NOTES (EMP 1)

1. SSN 1 - R. E. Partridge, EMP Testing Facility, 25 February 1964.

2. SSN 21 - Carl Baum, Impedances and Field Distributions for Parallel Plate Simulators, 6 June 1966.

3. SSN 27 - Carl Baum, Impedances and Field Distributions for Symmetrical Two-Wire and Four-Wire Transmission Line Simulators, 10 October 1966.

4. SSN 31 - Carl Baum, The Conical Transmission Line as a Wave Launcher and Terminator for a Cylindrical Transmission Line, 16 January 1967.

5. SSN 32 - Carl Baum, A Lens Technique for Transitioning Waves Between Conical and Cylindrical Transmission Lines, 25 January 1967.

6. SSN 37 - Carl Baum, The Brewster Angle Wave Matcher, 13 March 1967.

7. SSN 47 - Carl Baum, The Diffraction of an Electromagnetic Plane Wave at a Bend in a Perfectly Conducting Planar Sheet, 9 August 1967.

8. SSN 52 - T. L. Brown & K. D. Granzow, A Parameter Study of Two Parallel Plate-Transmission Line Simulators of EMP Sensor and Simulation Note 21, 19 April 1968.

9. SSN 53 - Carl Baum, Admittance Sheets for Terminating High-Frequency Transmission Lines, 18 April 1968.

10. SSN 54 - G. W. Carlisle, Matching the Impedance of Multiple Transitions to a Parallel Plate Simulator, 2 April 1968.

11. SSN 55 - R. W. Latham, Interaction Between a Cylindrical Test Body and a Parallel Plate Simulator, May 1968.

12. SSN 68 - Latham & Lee, Termination of Two Parallel Semi-Infinite Plates by a Matched Admittance Sheet, January 1969.

13. SSN 75 - Roberts & Granzow, A Model for Transient Reflections from Objects Within an Above-Ground Simulator, March 1969.

14. SSN 82 - Carl Baum, Some Considerations Concerning a Horizontally Polarized Transmission-Line Simulator, 12 April 1969.

15. SSN 85 - Latham & Lee, Division of a Two-Plate Line into Sections with Equal Impedance, July 1969.

16. SSN 90 - G. W. Carlisle, Impedance and Fields of Two Parallel Plates of Unequal Breadths, July 1969.

17. SSN 95 - Carl Baum, A Sloped Admittance Sheet Plus Co-Planar Conducting Flanges as a Matched Termination of a Two-Dimensional Parallel-Plate Transmission Line, 31 December 1969.

18. SSN 99 - C. D. Taylor & G. A. Steigerwald, On the Pulse Excitation of a Cylinder in a Parallel Plate Waveguide, March 1970.

19. SSN 100 - Carl Baum, Some Characteristics of Planar Distributed Sources for Radiating Transient Pulses, 12 March 1970.

20. SSN 103 - D. L. Wright, Sloped Parallel Resistive Rod Terminations for Two-Dimensional Parallel-Plate Transmission Lines, 7 May 1970.

21. SSN 108 - Carl Baum, Distributed Sources and Terminations for Launching and Terminating Plane Waves Either With or Without a Reflected Plane Wave, 23 May 1970.

22. SSN 111 - Latham & Lee, Electromagnetic Interaction Between a Cylindrical Post and a Two-Parallel Plate Simulator, I., July 1970.

23. SSN 118 - L. Marin, Effect of Replacing One Conducting Plate of a Parallel Plate Transmission Line by a Grid of Rods, October 1970.

24. SSN 121 - K. S. H. Lee, Electromagnetic Interaction Between a Cylindrical Post and a Two-Parallel Plate Simulator, II (A Circular Hole in the Top Plate), November 1970.

25. SSN 128 - D. Higgins, The Diffraction of an Electromagnetic Plane Wave by Interior and Exterior Bends in a Perfectly Conducting Sheet, January 1971.

26. SSN 132 - Thomas B. A. Senior, The Diffraction Matrix for a Discontinuity in Curvature, June 1971.

27. SSN 134 - Lennart Marin, A Cylindrical Post Above a Perfectly Conducting Plate, I (Static Case), July 1971.

28. SSN 135 - F. M. Tesche, On the Behavior of Thin-Wire Scatterers and Antennas Arbitrarily Located Within a Parallel Plate Region, August 1971.

29. SSN 136 - Lennart Marin, A Cylindrical Post Above a Perfectly Conducting Plate, II (Dynamic Case), August 1971.

30. SSN 137 - Cho, Chu & Tai, Proximity Effects of Semi-Infinite Parallel Plate Transmission Line in the Presence of a Perfectly Conducting Ground, August 1971.

31. SSN 139 - K. S. H. Lee, A Vertical Post Inside a Two-Parallel Plate Simulator, October 1971.

32. SSN 140 - Varvatsis & Sancer, Electromagnetic Interaction Between a Perfectly Conducting Sphere and a Two-Parallel-Plate Simulator, I, October 1971.

33. SSN 141 - F. M. Tesche, Numerical Determination of the Step Wave Response of a Thin-Wire Scattering Element Arbitrarily Located Above a Perfectly Conducting Ground, February 1972.

34. SSN 143 - C. E. Baum, General Principles for the Design of ATLAS I and II, Part I: ATLAS: Electromagnetic Design Considerations for Horizontal Version, January 1972.

35. SSN 144 - C. E. Baum, General Principles for the Design of ATLAS I and II, Part II: ATLAS: Electromagnetic Design Considerations for Vertical Version, January 1972.

36. SSN 145 - C. E. Baum, General Principles for the Design of ATLAS I and II, Part III: Additional Considerations for the Design of the Terminations, March 1972.

37. SSN 146 - C. E. Baum, General Principles for the Design of ATLAS I and II, Part IV: Additional Considerations for the Design of Pulser Arrays, March 1972.

38. SSN 148 - C. E. Baum, General Principles for the Design of ATLAS I and II, Part V: Some Approximate Figures of Merit for Comparing the Waveforms Launched by Imperfect Pulser Arrays onto TEM Transmission Lines, May 1972.

39. SSN 150 - D. F. Higgins, A Method of Calculating Impedance and Field Distribution of a Multi-Wire Parallel Plate Transmission Line Above a Perfectly Conducting Ground, February 1972.

THEORETICAL NOTES (EMP 2)

40. TN 25 - C. E. Baum, The Reflection of Pulsed Waves from the Surface of a Conducting Dielectric, February 1967.

INTERACTION NOTES (EMP 3)

41. IN 63 - C. E. Baum, Interaction of Electromagnetic Fields with an Object Which has an Electromagnetic Symmetry Plane, March 1971.

42. IN 85 - C. D. Taylor & T. Crow, Induced Electric Current on Some Configurations of Wires, Part I, Perpendicular Crossed Wires, November 1971.

43. IN 100 - T. Crow, T. Shumpert, & C. D. Taylor, Induced Electric Currents on Some Configurations of Wires, Part II, Non-Perpendicular Intersecting Wires, April 1972.

INTENDED FUTURE NOTES

44. D. F. Higgins, The Effect of a Perfectly Conducting Ground Plane with a Symmetrically Located Semi-Circular Hump on the Impedance and Field Distribution of a Two-Wire Transmission Line.

45. C. D. Taylor, et al., a note on the response of an L wire near a ground plane.